Spectroscopic characterization of high-energy and high fluence rate photon beams

by

Laura J. Bartol

A dissertation submitted in partial fulfillment of
the requirements for the degree of

Doctor of Philosophy

(Medical Physics)

at the

University of Wisconsin-Madison

2013

Date of final oral examination: 12/13/12

This dissertation is approved by the following members of the Final Oral Committee:
Larry A. DeWerd, Professor, Medical Physics
Robert J. Nickles, Professor, Medical Physics
Thomas R. Mackie, Emeritus Professor, Medical Physics
Bryan Bednarz, Assistant Professor, Medical Physics
Douglass L. Henderson, Professor, Engineering Physics

To my husband, Joe, and my parents, Mike and Gloria

Abstract

High-energy, high fluence rate photon sources are used in radiation oncology for the treatment of a variety of disease sites. Common dosimetry methods for characterizing these sources use energy-integrating devices; however, the most descriptive characterization of these sources are performed with devices that preserve the energy-specific information in the source output. This work used Monte-Carlo- (MC-) and measurement-based spectroscopic methods to characterize two therapeutic-level megavoltage photon sources. MC simulations were performed using the MCNP5 transport code and measurements were performed with a Compton-scattering (CS) technique.

Because MC was used extensively in this work, some general MCNP5 investigations were performed to benchmark the techniques used. Limitations in the advanced variance reduction techniques, Doppler-broadening model, and use of phase space files were investigated. Based on the results of these investigations, recommendations were made for using each technique.

The validity of the CS technique for use with megavoltage systems was demonstrated using MC simulations of a 6 MV linear accelerator field and measurements of a high dose rate ^{192}Ir source. Following these initial demonstrations, the spectrum of a ^{60}Co teletherapy unit was characterized. Simulations were performed to determine the spectrum's sensitivity to the source model. Multiple measurements were completed using a reverse-electrode germanium (REGe) detector with the CS spectrometry technique. The CS spectra were corrected for detector response and the CS geometry using a novel detector response function that was calculated using MCNP5. The detector response was unfolded using the Gold deconvolution method. Comparisons of the simulated and measured spectra showed agreement in terms of the peak positions, mean spectrum energy, and relative fluences under specific portions of the spectra.

The spectrum of a 6 MV photon field from a Varian Clinac iX linear accelerator was also characterized. Simulations were performed to determine the spectrum's sensitivity to changes in the primary electron source parameters of mean energy, spot size, and divergence. In addition, measurements were performed using the CS technique with the REGe detector. These measurements demonstrated that the linac spectrum was detectable above background, and the CS signal was dependent on field size.

Acknowledgments

This is one of the final and most pleasant parts of this thesis to write. This work has been a collaborative effort, and I would like to take this opportunity to acknowledge each person who has contributed to its completion. First, I would like to thank my advisor, Professor Larry DeWerd, for the wonderful opportunities he has given me since I began my adventure in the Calibration Lab. Larry provided the vision and encouragement that were necessary to complete this dissertation. He allowed me to freely explore my ideas while providing enough direction to keep me well-grounded. In addition, he showed unflagging support for my professional development, which has undoubtedly shaped me as a researcher and future medical physicist. Through dedication to his students and a high standard for research, Larry has built an exceptional program from which I am proud to have graduated. I would also like to thank the UWADCL's technical director, John Micka, who has been an invaluable resource during my tenure as a student. His fine attention to detail and extensive knowledge of the field increases the quality of each project in our group. From weighing in on research to practical jokes, John has made my time at the Calibration Lab memorable.

Many other staff members at the UWADCL have contributed to this work, as well. I would like to thank Ben Palmer for his help with the machining/design/miscellaneous portions of this project. He has taught me many valuable problem-solving skills and has repeatedly demonstrated the importance of a well-thought-out design. Dan Anderson deserves many thanks for his work with our computing cluster. It is hard to believe how much

it has grown and improved since I began my work here. I greatly appreciate Dan's efforts to make our computing program more efficient and robust. In addition, I thank him for his unyielding patience with me as I repeatedly brought down nodes and made requests to access and change the MCNP5 source code. Our radiation safety officer, Wendy Kennan, has also been a pleasure to work with, and I am grateful for her help with our multinuclide sources. Thank you to Keith Kunugi for his assistance with all of my random computing problems. His willingness to promptly address my issues was very much appreciated. Frank Grenzow and Ben Rosen have been wonderful to work with, as well. I am indebted to them for fixing my goofy spectrometer problems, without which the measurements in this work would not have been possible. Thank you to Cliff Hammer for being my liquid nitrogen supplier as well as an excellent resource for all of my TLD questions. Finally, Denise Roche deserves my sincerest thanks for her help with student affairs. From lab equipment purchases to travel reimbursement, Denise made life easier for me.

I also owe thanks to many of the UWMRRC students, both former and present. First, I would like to thank Dr. Steve Davis for the countless ways that he helped me with this work. Steve was an exceptional and patient mentor who helped me grow as a researcher. His calm demeanor and thoughtful approach to research were critical to keeping me pointed in the right direction. I owe gratitude to Dr. Jackie Moga for her help while I was learning the ropes in the field of spectrometry. Jackie did not hesitate to share her knowledge and helped me work through many technical problems. Thank you to Dr. Adam Paxton for his help with diverse problems ranging from Monte Carlo to printers. He graciously shared the spectrometer and helped me with lots of odds 'n ends with my measurements. Thank you to my cube-mate, Martha Malin, for lending an ear to my myriad of problems. Martha was instrumental in solving many of my research woes and in the editing of this thesis. I thank her for the many conversations that we had and hope that our paths cross in the future.

Finally, thank you to Qing Liang, Josh Reed, Jessie Snow, Travis McCaw, and Megan Wood for their help with editing this thesis.

I have been fortunate to find wonderful friends among my colleagues in the Calibration Lab. Thank you to my dear friends Jessie Snow and Stephanie Junell for their camaraderie through the years. From frequent coffee breaks to late nights with our good friend, *vino,* they kept me smiling. I feel blessed to have found such loyal friends with whom I could celebrate successes and lean on for support.

My training in Madison would have been incomplete without the clinical physics internship that I completed at the Turville Bay MRI & Radiation Oncology Center. My gratitude goes to Drs. Sean Frigo and Frank Goodin for giving me the opportunity for this program. My time at Turville Bay helped me develop many clinical skills and keep my research in perspective.

Finally, I would like to thank my family, who, as always, have provided unwavering support and love through my graduate career. To my mom, Gloria Plesha: thank you for the countless sacrifices you have made throughout my life to help me succeed. I am constantly learning from your example and strive to demonstrate to others the patience, love, and selflessness that you continue to show me. To my dad, Dr. Mike Plesha: without your guidance I could not have completed this journey. You have taught me many valuable lessons running the gamut from unit conversion to proper target shooting technique (both of which have impacted this thesis, by the way). Thank you for encouraging me to find my own path and for teaching me that life is not a race. To my sister, Camille, my brother, Rob, and his wife, Christina: whether you were near or far you always let me know that I was in your thoughts. Thank you for the countless phone calls, texts, and welcome distractions you have given me over the years. To my Great Uncle Abe: thank you for the generous gift of my college education, without which I would not be where I am today. To the Bartol contingent of my family: thank you for welcoming me into your family with open arms– I sincerely cherish your love and support.

And lastly, to my husband, Joe: thank you for your consistent support, enduring love, and constant faith in me. I could not have reached this milestone without your patience and devotion. Your passion for learning continues to inspire me, and I thank you for using it to help me grow. Thank you for sweetening my life with laughs and love, and I look forward to the next chapter in our crazy journey.

Contents

List of Figures

List of Tables

Chapter 1

Introduction

1.1 Overview

Megavoltage external beam photon sources are widely used for non-invasive treatments of deep-seated diseases. Successful treatment with these sources depends on accurate dosimetry and treatment planning, both of which are influenced by the source's energy spectrum. Dosimetry for external beam systems is performed in terms of absorbed dose to water, which is measured with integrating dosimeters such as ionization chambers, thermoluminescent dosimeters, and film. The readings from these dosimeters are related to absorbed dose to water through corrections that are influenced by the energy spectrum. The spectrum is also an important component of the source model in treatment planning systems. Dose calculations with these systems rely on the accuracy of the modeled spectrum to predict dose distributions in patients. Although it has a large impact on dosimetry and treatment planning, the energy spectrum of an external beam source is rarely characterized directly. As such, the aim of this work was to determine the spectra of two external beam sources, a ^{60}Co teletherapy source and a 6 MV linear accelerator, using measurement and simulation methods.

Experimental characterization of megavoltage external beam spectra is challenging for a variety of reasons. First, due to small interaction cross sections in this energy range, typical detector materials are relatively inefficient at detecting high-energy photons. In addition, external beam units have characteristically high fluence rates that tend to overwhelm spectroscopic measurement systems. The measurements in this work were performed using a Compton-scattering (CS) technique that circumvented both of these challenges. Monte-Carlo- (MC-) generated corrections were used to correct these spectra for measurement artifacts. MC simulations were also used to determine spectra and to investigate the influence of spectroscopic differences on dosimetry.

1.2 Description of upcoming chapters

Chapter 2 provides an overview of the measurement-based and simulation-based spectroscopic methods that were used in this work. Background information regarding the megavoltage photon sources that were investigated is presented, including a discussion of current dosimetry methods, general beam characteristics, spectroscopic techniques, and treatment planning.

Chapter 3 describes three general MC investigations that were performed to isolate and investigate basic simulation techniques in the Monte Carlo N-Particle (MCNP5) radiation transport code. First, deficiencies in the compatibility of two variance reduction (VR) techniques with other simulation methods are discussed. Second, an investigation regarding the implementation of the MCNP5 Doppler-broadening model is presented. Finally, the limitations of the code to generate and use phase-space files is discussed. Based on the findings of each investigation, recommendations are made for the use of the described techniques.

Chapter 4 focuses on the common MC and experimental methods that were used to characterize the two megavoltage sources that were investigated in this work. First, the simulation methods that were used to characterize the CS spectrometry system are discussed. This section addresses the simulation geometries and VR techniques that were used to generate detector response functions and simulated pulse-height distributions (PHDs). Next, the CS spectrometry measurement method is discussed in detail, including descriptions of the detector, electronics, and shielding system that were used. This section also presents the method that was used to unfold the detector response function from PHD measurements.

Chapter 5 presents demonstrations of the CS spectrometry technique using MC and measurement methods. The MC demonstration was performed to assess the expected performance of the CS spectrometry system for the measurement of a 6 MV linear accelerator field. This section describes the simulation geometry and VR techniques that were used to calculate the expected PHDs for primary and secondary sources. A comparison of the PHDs and total number of expected pulses for all sources is presented. In addition, this chapter addresses the CS spectrometry measurements that were performed for the VariSource$^{\mathrm{TM}}$ (VS2000) high dose rate ^{192}Ir source. This section describes the experimental methods that were used for spectra measurements at a variety of scattering angles. In addition, the corrections that were applied to measurements are discussed. A comparison of the spectra for all of the scattering angles is performed. Finally, based on the results of the MC simulations and measurements, recommendations are made for higher-energy investigations.

Chapter 6 presents the spectroscopic characterizations that were performed for the therapy-level Theratronics T1000 ^{60}Co unit at the University of Wisconsin Accredited Dosimetry Calibration Laboratory (UWADCL). This section discusses characterizations that were performed using MC and measurement methods. First, the development and verification of an MC model of the T1000 system is described. The verification measurements that were performed to validate the MC model are presented. In addition, the sensitivity studies that were performed to determine the influence of the source model parameters on percentage depth dose and the spectrum are discussed. Finally, the influence of the structural components of the T1000 system (i.e., source, source housing, collimation, etc.) on the spectrum is presented. Next, this chapter presents and analyzes the four CS spectrometry measurements that were performed. The measured and MC-generated spectra are compared using the relative fluences in various regions of the spectrum. In addition, they are compared as a function of average spectrum energy.

Chapter 7 describes the spectroscopic characterizations that were performed for the 6 MV beam of the Varian Clinac iX linear accelerator at the University of Wisconsin Carbone Cancer Center. This section discusses characterizations that were performed using MC and measurement methods. First, the development and verification of an MC model for the 6 MV photon beam is described. In addition, the sensitivity studies on the spectroscopic effect of the primary electron beam parameters (energy, size, and divergence) are presented. Next, this chapter discusses the CS spectrometry measurements that were performed for this system. The raw measured and background-subtracted pulse-height distributions are analyzed. In addition, the response of the CS system to changing field size is discussed.

Finally, Chapter 8 presents overall conclusions for each portion of this work. Possible directions for future investigations are discussed.

Chapter 2

Background

2.1 Photon spectrometry

The most descriptive characterization of a radiation beam is provided by its energy spectrum. This quantity describes the distribution of photons passing through a point as a function of energy. An energy spectrum is determined from the measurement of a pulse-height distribution (PHD), which characterizes the collection of electrical pulses that are generated from radiation interactions in a detector. PHDs are measured by pulse-mode detectors which, for each interaction that occurs, generate a separate electrical pulse whose amplitude is related to the energy deposited. The following section discusses the details of photon spectrometry and various methods by which an energy spectrum is determined from a PHD.

2.1.1 Measurement systems

2.1.1.1 Detectors

A variety of detectors may be operated as pulse-mode spectrometers. The most common spectrometers are scintillators, which are crystalline detectors that emit prompt fluorescence following excitation by radiation. Scintillators are popular due to their high intrinsic efficiency and their ability to detect many kinds of radiation. These detectors exhibit an energy resolution of about 6 % for 662 keV photons (Knoll, 2000). For some applications, this resolution is inadequate. In such cases, semiconductor detectors are often used. Semiconductor detectors have a superior energy resolution of about 0.2 % at 662 keV (Knoll, 2000). Radiation interactions in these detectors generate electron-hole pairs in an amount that is proportional to the detected particle's energy. The motion of these pairs in an applied electric field generates the electrical signal from the detector (Knoll, 2000).

The most common semiconductor detector materials are silicon and germanium. Silicon detectors (atomic number, $Z = 14$) are used for low-energy photon and beta spectrometry. These applications take advantage of the relatively low atomic number of silicon to maximize full-energy gamma detection and to minimize electron backscatter. Germanium ($Z = 32$) is generally used for the measurement of medium- to high-energy photons because its higher atomic number results in larger photoelectric cross sections than are inherent in silicon. As such, germanium detectors are more efficient at detecting photons in this energy range.

High-purity germanium has a small bandgap (0.7 eV) that results in thermally-induced leakage when operated at room temperature (Knoll, 2000). To avoid this, germanium detectors are usually operated at the liquid nitrogen boiling point of 77 K. These detectors may be found in either planar or coaxial configurations, both of which have $n+$ and $p+$ contact layers (heavily doped n-type and p-type layers, respectively). These contacts, called dead layers, are not part of the active volume of the detector. As such, the dead layers are made as thin as possible to minimize their perturbation of the beam. A large-volume crystal with thin dead layers may be used to detect photons with energies ranging from a few keV up to many MeV (Knoll, 2000).

2.1.1.2 Electronics

Several pulse-processing modules are connected to a detector to complete a spectrometry system. In germanium systems, the detector is directly connected to a preamplifier. This module amplifies the raw detector signal, which is generally too small for practical use. In addition, the high-voltage bias to the detector is generally applied through the preamplifier. The output from the preamplifier is a linear-tail pulse that is next processed by a linear amplifier. This device further amplifies and shapes the pulse, resulting in a shaped-linear output with a near-Gaussian shape. Following the linear amplifier, the signal is sent to an analog-to-digital converter (ADC) which translates the pulse into an equivalent digital signal (Knoll, 2000). Finally, a multichannel analyzer (MCA) sorts these digital pulses into appropriate bins (called channels) based on amplitude, resulting in a PHD.

2.1.2 Spectrometer characterization techniques

In order to convert a measured PHD into an energy spectrum, a detection system must be characterized in terms of energy and efficiency. These characterizations account for the photon interactions in the detector and surrounding shielding, and they are specific to the geometry and electronic settings used for measurement.

2.1.2.1 Energy calibration

The output from an MCA gives a distribution of pulse amplitudes. In order to relate MCA pulse height to energy, the system must be calibrated (Knoll, 2000). Energy calibration is performed by measuring a high-purity standard source whose emission energies are well known. Measurement of such a source allows for a relationship between detected energy and MCA channel to be determined. Most spectrometry software will generate the best fit for the measured energy calibration PHD based on the positions (i.e., channel numbers) of user-identified peaks and their energies.

2.1.2.2 Detector response

The probability of photon interaction in a material is energy-dependent; therefore, a spectrometer will not equally detect photons of all energies. This indicates that an energy-dependent efficiency correction must be applied to all measurements. The efficiency correction accounts for the effects of energy-dependent interaction coefficients (intrinsic efficiency), crystal geometry, and surrounding materials on a measurement.

Measurement techniques The most basic approach to determining an efficiency correction involves measuring radionuclide sources that are traceable to the activity standard at the National Institute of Standards and Technology (NIST). This technique presents multiple problems when a detector is being characterized for use with high-energy and high fluence rate photons. First, to determine an accurate efficiency calibration, the geometric conditions for the calibration measurement must be representative of the irradiation geometry for related experimental measurements (Knoll, 2000). Since NIST-traceable sources do not exhibit high fluence rates or source sizes, these conditions cannot be met for complicated measurement geometries. Second, this technique characterizes only the full-energy peak efficiency of the detector. Thus, it is useful for measurements in which all of the incident photon energy is deposited in the detector by photoelectric interactions. For photon energies above 150 keV, Compton scattering (CS) dominates the interaction cross section in germanium (Berger et al., 2005b), leading to substantial partial energy deposition. Because of these complications, this conventional efficiency calibration method does not work well for many spectrometry systems.

Calculation techniques Alternatively, the efficiency correction may be determined using a calculated detector response, which accounts for all measurement artifacts introduced by the spectrometer and surrounding structures. The detector response is related to the spectrum and measured PHD, $t\left(E_{\mathrm{inc}}\right)$ and $m\left(E\right)$, by

$$m\left(E\right) = \int\limits_{0}^{E_{\mathrm{inc,max}}} H\left(E, E_{\mathrm{inc}}\right) \cdot t\left(E_{\mathrm{inc}}\right) dE_{\mathrm{inc}} + \varepsilon_n, \tag{2.1}$$

where $H\left(E, E_{\mathrm{inc}}\right)$ is the one-dimensional detector response array describing the probability that an incident photon of energy, E_{inc}, is recorded by the spectrometer at a different energy, E. The additive term, ε_n, is the random noise introduced by the detection system. Beach (2005; 2007) describes a method by which the detector response $H\left(E, E_{\mathrm{inc}}\right)$ is broken into two components as

$$H\left(E, E_{\mathrm{inc}}\right) = R\left(E, E_{\mathrm{inc}}\right) \cdot G\left(E, E_{\mathrm{inc}}\right). \tag{2.2}$$

The first component, $R\left(E, E_{\mathrm{inc}}\right)$, describes how radiation interactions in the detector and surrounding structures affect a measurement. It accounts for all of the major photon interaction mechanisms (e.g., photoelectric effect, CS, pair production) as well as artifacts introduced by the measurement geometry (e.g., fluorescence escape peaks, Compton outscattering, annihilation photon escape). This function may be determined entirely using calculation techniques. The second component, $G\left(E, E_{\mathrm{inc}}\right)$, accounts for the Gaussian-like broadening of photopeaks that occurs due to the statistical distribution of charge carriers produced for a given energy deposition. In addition, it accounts for the uncertainty introduced by the signal amplification process. $G\left(E, E_{\mathrm{inc}}\right)$ is determined from measurements of the full-width-at-half-maxima (FWHM) for photopeaks with a range of energies.

There are three common methods of determining the detector response (Moga, 2011). First, experimental methods may be used to determine the detector response for a few photon energies, and the response for other energies may be interpolated from those measured data (Bentley et al., 1967; Jessen, 1973). This method is limited by the availability and maximum activity of monoenergetic sources. Second, analytical methods may be used to calculate the detector response based on interaction probabilities (Gardner et al., 1986; Jin et al., 1986; Yacout et al., 1986); however, this method breaks down when complex collimation and shielding geometries are used. Third, Monte Carlo (MC) methods may be used to calculate the detector response (Faddegon et al., 1990; Sood and Gardner, 2004; Fehrenbacher et al., 1996).

Beach (2005; 2007) determined the detector response for the reverse-electrode germanium (REGe) detector (Canberra Industries, Inc.; Meriden, CT) used in this work using MC methods. In this previous work, the detector was modeled using the Monte Carlo N-Particle (MCNP5) MC code (X-5 Monte Carlo Team, 2005). Using a mathematically collimated source, the detector response was characterized for monoenergetic photons in increments corresponding to the experimental channel size that was determined during energy calibration. The F8 pulse-height tally was used to score the energy deposited in the active volume of the germanium detector for each history. In order to account for the finite energy resolution of the detection system, the Gaussian Energy Broadening (GEB) feature of MCNP5 was used. When the GEB feature is invoked, MCNP5 randomly samples for the detected photon energy, E, from a Gaussian distribution with a FWHM described by

$$\mathrm{FWHM} = a + b \cdot \left(E + c \cdot E^2\right)^{\frac{1}{2}} , \tag{2.3}$$

where a, b, and c are parameters determined from the measured FWHM values of a multi-nuclide standard source.

In Beach's work, each monoenergetic photon simulation produced a one-dimensional array. The entire series of one-dimensional arrays was combined to create a detector response function (DRF), $\mathbf{H}$. This DRF was a square matrix of order M that described the expected PHD for each of the M monoenergetic photon beams. Thus, the detector's response to many incident photon energies was contained in a single matrix, $\mathbf{H}$, rather than multiple individual one-dimensional arrays, $H\left(E, E_{\text{inc}}\right)$.

The DRF determined by Beach used a simplified model geometry that accounted for only the detector. In addition, the system was characterized only for energies below 1 MeV. While the current thesis work adhered to the same methodology of Beach, a more detailed simulation geometry was used. Furthermore, the detector response was characterized for photon energies in the megavoltage range.

2.1.3 Measurement correction techniques

Section 2.1.2.2 presented the mathematical relationship between a measured PHD and the true energy spectrum; however, the practical conversion of a PHD to an energy spectrum is not straightforward. The following section discusses two methods that can be used to perform this conversion.

2.1.3.1 Unfolding

There are multiple methods by which to unfold the spectrum from a measured PHD using the DRF. For a discrete system, such as a binned PHD, Equation 2.1 can be written in matrix form as

$$\mathbf{m} = \mathbf{H}\mathbf{t}, \tag{2.4}$$

where $\mathbf{m}$ and $\mathbf{t}$ are one-dimensional arrays representing the measured PHD and true spectrum, respectively. The most obvious approach to unfolding $\mathbf{t}$ is the inverse method. This method uses the inverse of $\mathbf{H}$ to solve for $\mathbf{t}$; however, this problem is ill-conditioned indicating that the determination of $\mathbf{t}$ is extremely sensitive to errors in the measured data (Morháč et al., 1997, 2003). Thus, while mathematically valid, the inverse method leads to an unstable estimate of the true spectrum.

A more stable approach estimates the true spectrum using an iterative method of solution. The specific parameters used with this unfolding technique have varying degrees of complexity and effectiveness when used with spectroscopic data. In general, this method involves making an initial estimate of the true spectrum and comparing the expected measured PHD (based on this estimate) with the actual measured PHD. A general form of this iterative method is given by

$$\mathbf{t}^{(k+1)} = \mathbf{t}^{(k)} + \mu \left[\mathbf{m} - \left(\mathbf{A}\mathbf{t}^{(k)}\right)\right], \tag{2.5}$$

in which μ is the relaxation factor, $\mathbf{A}$ is a matrix describing the system, and k is the number of the current iteration. This calculation is iterated until the system converges. The iterative method was used by Skarsgard et al. (1961) in the correction of x-ray spectra. In these calculations, μ was taken as unity and $\mathbf{A}$ was the DRF (i.e., $\mathbf{H}$ in Equation 2.4). Due to the selection of μ and $\mathbf{A}$, their solutions included negative values, which is physically nonrealistic for spectroscopic data. Bandžuch et al. (1997) noted that if $\mathbf{A}$ is positive definite, then a convergent solution exists. Since this is rare in physical problems, some modifications were added to ensure that the eigenvalues of $\mathbf{A}$ are real and positive. This is accomplished by multiplying each side of Equation 2.4 by $\left(\mathbf{H}^T\mathbf{H}\right)\mathbf{H}^T$ which gives

$$\left(\mathbf{H}^T\mathbf{H}\right)\mathbf{H}^T\mathbf{m} = \left(\mathbf{H}^T\mathbf{H}\right)\left(\mathbf{H}^T\mathbf{H}\right)\mathbf{t}, \tag{2.6}$$

or

$$\mathbf{m}' = \mathbf{H}'\mathbf{t}. \tag{2.7}$$

This is substituted back into Equation 2.5 to give the Van Cittert algorithm of deconvolution as

$$\mathbf{t}^{(k+1)} = \mathbf{t}^{(k)} + \mu \left[\mathbf{m}' - \left(\mathbf{H}'\mathbf{t}^{(k)}\right)\right]. \tag{2.8}$$

Finally, Bandžuch cites an appropriate local relaxation factor of

$$\mu = \frac{t_i^{(k)}}{\sum\limits_{m=0}^{N-1} \mathbf{H'}_{im} t_m^{(k)}}, \tag{2.9}$$

to give what is known as the Gold deconvolution:

$$t_i^{(k+1)} = t_i^{(k)} + \frac{t_i^{(k)}}{\sum\limits_{m=0}^{N-1} \mathbf{H'}_{im} t_m^{(k)}} \left[m_i - \left(\sum \mathbf{H'}_{im} t_m^{(k)} \right) \right]. \tag{2.10}$$

This form gives the value of the i^{th} element of the vector $t^{(k+1)}$ for the $k+n^{th}$ iteration. The benefit of using the Gold deconvolution is that its solutions are always real and positive.

Beach (2005; 2007) used the Gold deconvolution procedure to unfold discrete low-energy photon spectra from measurements performed with the REGe detector. The optimal number of iterations for unfolding the true spectrum in this application was found to be 1000. This method was also applied by Davis (2009) and Moga (2011) in the unfolding of low-energy x-ray spectra.

2.1.3.2 Backward stripping

Backward stripping is an alternative approach to measurement correction. This method involves the scaling and subtraction of one-dimensional detector responses from measured spectra, starting with the highest channel in the spectrum. While it is straightforward to implement, this method is unable to appropriately correct for the Gaussian-like broadening of photopeaks. The backward stripping method has been used by several investigators including Seelentag (1979), NIST (2010), and Moga (2010). Each of these groups focused on the correction of low-energy bremsstrahlung measurements. Seelentag used a combination of MC- and analytically-derived detector response functions for measurement corrections.

The response functions at NIST were determined using empirical methods. Finally, Moga used MC-derived detector response functions.

At the UWMRRC, Moga implemented a backward stripping algorithm using the Octave programming language. This work deviated from most previous investigations in that it used detector responses that were determined using MC. This method performed well for low-energy x-ray spectra, but performed increasingly poorer for higher energies. This was attributed to the increasing effect that Gaussian broadening has on spectra of higher energies. Since Gaussian broadening is not inherently accounted for in normal backward stripping applications, Moga investigated the effect of including various amounts of broadening in the DRF. The results indicated that, while not physically realistic, modeling a constant amount of broadening for the entire energy range gave the best results.

2.2 Megavoltage radiation therapy sources

The earliest external beam treatments were performed using kilovoltage x-ray sources (Khan, 2003; Laughlin, 1989). Radiation therapy with this technology was limited because these low-energy x rays exhibited poor depth-dose characteristics resulting in the inadequate treatment of deep-seated tumors. Furthermore, the equipment used to produce these beams exhibited very low dose rates (Johns, 1980). These difficulties led physicists to explore higher-energy and higher-dose-rate treatment options. In addition to addressing the depth-dose and dose-rate issues, high-energy photon beams were expected to provide physical advantages such as lowered skin dose, lowered bone dose, and less lateral photon scatter (Laughlin et al., 1986).

The mission to find high-energy photon treatments resulted in orthovoltage (150-500 kV), supervoltage (500-1000 kV), and megavoltage (>1 MV) therapies. While the ideal photon energy for any treatment is based on patient-specific factors, megavoltage radiation has become standard for most treatments (Karzmark et al., 1993). The term megavoltage technically describes x-ray beams; however, it is common to include gamma-ray sources with energies greater than 1 MeV in this category as well. The following sections discuss the dosimetry and characteristics of two kinds of megavoltage therapy devices: the ^{60}Co teletherapy unit and the linear accelerator.

2.2.1 Dosimetry

2.2.1.1 Dosimetric quantities

Ultimately, the current dosimetric quantity of importance for megavoltage photon beams is absorbed dose, D, to a particular tissue. Primary standards of absorbed dose have been developed using water as a reference material because of its metrological qualities that are similar to those for tissue (ICRU, 2001). Absorbed dose is defined as

$$D = \frac{d\bar{\epsilon}}{dm}, \tag{2.11}$$

where $d\bar{\epsilon}$ is the mean energy imparted by ionizing radiation to an infinitesimal volume containing matter of mass dm (Attix, 2004).

While dose is a descriptor of the energy deposited in a particular medium, it is not a fundamental descriptor of the beam. The most basic quantity that accounts for the individual photons in a beam is fluence. If N_e is the expectation value of particles passing through a finite sphere surrounding a point, P, the fluence, Φ, at P is defined as

$$\Phi = \frac{dN_e}{da}, \tag{2.12}$$

as the sphere is reduced to be infinitesimally small at P with a great-circle area of da (Attix, 2004). Fluence does not itself account for the energies of the individual particles passing through da; however, a related quantity called energy fluence does. Letting R be the expectation value of the total energy carried by all N_e particles into the previously described sphere, the energy fluence is defined as

$$\Psi = \frac{dR}{da}, \tag{2.13}$$

as the sphere is reduced to be infinitesimally small at P (Attix, 2004).

Although energy fluence is the most elementary field-descriptive quantity (Attix, 2004), it fails to describe the field's energy distribution. The energy spectrum, which is a quantity that is closely related to energy fluence, does just this. The energy spectrum, $\Phi(E)$, is defined as

$$\Phi(E) = \frac{d}{dE}\left(\frac{dN_e}{da}\right), \tag{2.14}$$

and is related to the energy fluence by

$$\Psi = \int \Phi(E) \cdot E\, d(E)\,. \tag{2.15}$$

Fluence, energy fluence, and the energy spectrum are deterministic quantities that describe a field of ionizing radiation at a point. Thus, if the energy spectrum of a field is known, many other quantities may be calculated.

2.2.1.2 Dosimetry formalism

In the United States, reference dosimetry for megavoltage photon beams follows the recommendations of the American Association of Physicists in Medicine's (AAPM) Task Group 51 (TG-51). The TG-51 protocol is based on the primary absorbed-dose to water standard for a therapy-level ^{60}Co beam, the water calorimeter (Minniti et al., 2006). This standard is maintained at NIST and is transferred to clinical ionization chambers via an absorbed-dose to water calibration coefficient, $N_{D,w}^{^{60}\mathrm{Co}}$. This coefficient allows for the conversion of a charge measured with an ionization chamber to an absorbed-dose to water in a ^{60}Co beam under specific conditions. While the $N_{D,w}^{^{60}\mathrm{Co}}$ calibration coefficient is directly applicable to a ^{60}Co beam, chambers holding this calibration are also used to measure megavoltage beams of other energies. In these circumstances, a beam quality conversion factor, k_Q, is required to account for the change in chamber sensitivity between the reference ^{60}Co beam and the beam of interest (quality, Q). In TG-51, k_Q is tabulated for a variety of ionization chambers as a function of the percentage depth dose from photons at a depth of 10 cm in water. According to TG-51, absorbed dose to water, D_w, is calculated by

$$D_w = M N_{D,w}^{^{60}\mathrm{Co}} k_Q, \tag{2.16}$$

where M is the charge reading under the reference conditions (corrected for recombination, polarity effects, and atmospheric circumstances).

Reference dosimetry according to TG-51 provides a description of large, flat beams in terms of energy imparted to water. However, energy absorbed in a particular medium is not the most elementary descriptor of the beam. Furthermore, many intensity-modulated and stereotactic radiosurgery beams are small in comparison to reference beams, are not flat over a large region, and often cannot accommodate the reference conditions specified by TG-51. In these situations, the quantities that are dependent on the reference field's spectrum (e.g., components of k_Q) cannot be used for these nonstandard beams, and an alternative characterization methodology is needed. This work explores the potential for spectroscopic dosimetry.

2.2.2 ^{60}Co teletherapy units

The British physicist William Mayneord began investigating radioisotopes for medical use during World War II. He suggested ^{60}Co as a replacement for radium, the radioisotope that was commonly used for cancer treatment at the time (Johns, 1980). Following his suggestion, ^{60}Co teletherapy was developed in Canada in the early 1950s (Laughlin et al., 1986; Laughlin, 1989; Podgorsak, 2005). Since its development for radiation treatment, ^{60}Co has also become the radionuclide used for calibrating many dosimeters that are required for routine dosimetry and quality assurance. The following sections discuss these applications as well as the general characteristics of a ^{60}Co teletherapy beam.

2.2.2.1 Applications

Patient treatment Teletherapy is a general term that describes an external beam treatment in which the radiation source is a considerable distance from the patient (Khan, 2003). In ^{60}Co teletherapy this source is often mounted isocentrically, allowing for the treatment head to rotate around a patient with a fixed source-to-axis distance of either 80 cm or 100 cm (Podgorsak, 2005). Cobalt-60 teletherapy can be used in the treatment of diseases throughout the whole body (e.g., head and neck, breast, lung (Fox et al., 2008)). It is also frequently used in total body irradiations to treat non-Hodgkin's lymphoma, multiple myeloma, metastases, and acute lymphocytic leukemia (Lim, 2006).

Cobalt-60 teletherapy systems exhibit a few advantages over other modern forms of external beam radiotherapy. Perhaps the most significant advantage is that they do not require a complex power supply or acceleration structure for operation (Laughlin, 1989). Furthermore, the dose rates from such units, while decreasing with time, are predictable based on a simple radioactive decay scheme. Finally, these systems are typically less expensive to maintain (van der Giessen, 2002; Van Dyk and Battista, 1996).

Despite these advantages, treatment using ^{60}Co teletherapy has declined precipitously in the past thirty years. This is partially due to the strict licensing and safety regulations for medical irradiators imposed by the Nuclear Regulatory Commission and state radiation control programs. In addition, ^{60}Co teletherapy has declined because of the inferiority of ^{60}Co beam characteristics when compared with linear accelerators (e.g., larger beam penumbra, lower beam energy, lower dose rate) (Van Dyk and Battista, 1996; Laughlin et al., 1986; Fox et al., 2008). However, recent investigations have demonstrated that, with proper improvements in machine design, about 25 % of patients that require radiation therapy may be effectively treated with ^{60}Co (Van Dyk and Battista, 1996). In particular, patients with shallow lesions, small separations, and targets that may be treated with multiple conformal therapy are good candidates for ^{60}Co teletherapy. This has led to a resurgence in ^{60}Co teletherapy, with vendors developing units that are equipped to perform intensity-modulated radiation therapy and on-board magnetic resonance imaging (Schreiner et al., 2003; Dhanesar, 2008; Fox et al., 2008).

Radiation dosimetry Reference dosimetry is a critical component of comprehensive quality assurance programs for all external beam treatment devices. Dosimeters used in reference dosimetry are calibrated in a reference field in order to relate its reading (e.g., charge, optical density) to a dosimetric quantity of interest (e.g., air kerma, dose, exposure). Because it is well characterized, ^{60}Co is a very common radionuclide used for dosimeter calibration. For example, clinical reference dosimetry for high-energy photon beams involves measurements using an ionization chamber with an absorbed-dose to water calibration coefficient that was determined using a therapy-level ^{60}Co beam (Almond et al., 1999). In a similar way, ^{60}Co is often used to calibrate dosimeters for experimental research. In most cases, these dosimeters are subsequently used in the measurement of beams with different energies and geometries. It is known that the output of a radiation dosimeter is dependent upon a variety of parameters including absorbed dose, dose rate, beam energy, and angular incidence of the radiation (Rogers, 2009). Due to these dependencies, a comprehensive understanding of the ^{60}Co calibration field is necessary to accurately interpret information from subsequent measurements.

2.2.2.2 Beam characteristics

The radioactive material for ^{60}Co teletherapy sources is generally in the form of small pellets or discs that are double-encapsulated in a cylindrical stainless-steel vessel (Podgorsak, 2005;

Khan, 2003). A typical capsule is (1 to 2) cm in diameter and 2.5 cm in height (Podgorsak, 2005). Due to the relatively large diameters of these sources, ^{60}Co teletherapy beams have large geometric penumbrae. This is often considered a disadvantage from a treatment planning perspective where sharp dose fall-off near the field edge is desired. These sources have an initial activity on the order of 10 kCi producing a dose rate of about $2\,\mathrm{Gy}\cdot\mathrm{min}^{-1}$ at 100 cm from the source (Podgorsak, 2005).

^{60}Co is a synthetic radioisotope that is produced by fast and thermal neutron activation of naturally occurring ^{59}Co in nuclear reactors (Khan, 2003). It decays with a half-life of 5.27 years to an excited state of ^{60}Ni via beta emission. The ^{60}Ni then quickly decays to its ground state by gamma emission (99.88 % 1.17 and 1.33 MeV, 0.12 % 1.33 MeV only) (Chu et al., 1999). While ^{60}Co decay results in the emission of only two photon energies it is well known that encapsulated ^{60}Co source spectra include other components due to scatter in the source, encapsulation, and surrounding shielding (Mora et al., 1999). This degradation leads to faster attenuation in media than would be predicted for the primary beam alone (Scrimger and Cormack, 1963). Various authors have found that this low-energy continuum due to source and head scatter contributes about 10 % (Aitken and Henry, 1964), (13 to 19) % (Ehrlich et al., 1976), and (30 to 38) % (Mora et al., 1999) of the total fluence for a ^{60}Co teletherapy beam. This amount was found to be dependent on field size and machine geometry.

2.2.2.3 Spectroscopic characterization

Monte Carlo techniques Multiple investigators have used MC techniques to characterize ^{60}Co teletherapy units. Han et al. (1987) was one of the first groups to perform such a study. They used the Electron Gamma Shower (EGS) MC code to investigate the dependence of spectra and output factors on field size for the Theratron 780 unit. They modeled a simplified geometry that was symmetric about the central axis with a single, solid collimator. These simulations did not accurately calculate machine output with field size, indicating that a more accurate model of the secondary collimation was necessary.

Mora et al. (1999) performed similar simulations for the Eldorado 6 teletherapy unit using the BEAM-EGS4 code. Their model of the secondary collimation incorporated a more realistic rectangular geometry. Agreement between measured and simulated depth-dose curves in the buildup region ([2-3] %) and output factors (0.1 %) was achieved. Similarly, Tedgren et al. (2010) used BEAMnrc, the successor to BEAM-EGS4, to model a Siemens Gammatron 1 ^{60}Co unit with two sources of different diameters. Their study showed that the spectrum changes with source diameter and, to a lesser extent, with treatment head geometry.

Most previous investigations have used various versions of the EGS MC system; however, Smilowitz (2001; 2002) used the MCNP code to extensively model the Eldorado 78 ^{60}Co unit that was formerly installed at the UWMRRC. This model showed good agreement between measured and simulated depth-dose curves and profiles for various field sizes. This study also investigated the contribution of scatter to the total fluence as a function of field size.

While these findings all suggest that MC is an effective tool for modeling a ^{60}Co teletherapy unit, none of these studies compared simulated spectra to measured spectra. The present work builds on these published investigations by performing this comparison. In addition, this work aims to quantify the effect of spectroscopic differences on dosimetry.

Measurement techniques While it is less common than using MC methods, some investigators have used measurement techniques to characterize ^{60}Co teletherapy spectra. Early measurements were performed by Costrell (1962) who used a low-activity source for measurements. Scrimger and Cormack (1963) used a CS technique to measure the spectrum after it was scattered at multiple angles. Their measurements were corrected using a small theoretically-derived detector response matrix followed by corrections for the CS kinematics. Due to the low resolution of their measurement system, the two primary ^{60}Co emissions were not distinguishable at any scattering angle. Similar measurements were performed by Jessen (1973); however, these results had slightly better resolution. Aitken and Henry (1964) directly measured the spectrum of an altered teletherapy unit that housed a low-activity source. They performed measurements with the source both in and out of the teletherapy head to estimate the amount of scatter coming from the different components of the source and unit. Similar measurements were performed by Ehrlich et al. (1976) at the National Bureau of Standards, now known as NIST. They performed a qualitative comparison with other authors, but concluded that the amount of scatter present in a given spectrum is dependent on the source and its housing.

Most previous investigators have used scintillation detectors for these measurements. In addition, they have used relatively few detector response functions for measurement corrections. The current thesis work used a high-purity germanium detector and hundreds of detector response functions to correct measurements. Furthermore, the correction methods in this work considered the effects of bound electrons and measurement geometry, both of which affected measurement results.

2.2.3 Electron linear accelerators

The development of the medical linear accelerator was approximately concurrent with the development of the ^{60}Co teletherapy unit (Podgorsak, 2005). Since its introduction, the linear accelerator has become the most common treatment device for external beam applications (Laughlin et al., 1986). The following section discusses the uses and characteristics of linear accelerator beams.

2.2.3.1 Clinical applications

Linear accelerators are used to create both photon and electron beams for medical use. Furthermore, they produce beams of different energies for each of these modalities. Because of the variety of beams produced, linear accelerators may be used to treat many conditions. The following section gives an overview of photon-based treatments; however, this is not meant to be a comprehensive discussion of linear accelerator treatments as this is a vast subject.

The most common photon-based linear accelerator treatments use multiple beams to conform the dose to a target volume and to deliver a uniform dose within that region (Podgorsak, 2005). The appropriate shape, position, and energy of these beams is often determined using computed tomography (CT) data of the treatment region. The jaws of the linear accelerator are used to define the field for basic treatments; however, while this method is still used, many treatments are now delivered using intensity modulation. These treatments use multi-leaf collimators (MLCs) or compensators to create complex spatial configurations. Treatments of this kind are generally delivered on a fractionated schedule that allows for healthy tissue to repair between treatment sessions. These common treatment techniques are used to treat a wide variety of cancers and other medical conditions (Yu et al., 2008).

A less common photon-based procedure is stereotactic radiosurgery. This technique uses a three-dimensional guiding device to localize a small lesion, allowing for the precise delivery of radiation, typically in one session. These treatments involve small circular fields (0.4 cm to 6 cm diameter, depending on the modality) and are used in instances where conventional surgery cannot be used (e.g., brain metastases, lung).

2.2.3.2 Beam characteristics

The x-ray beam from a linear accelerator is generated when electrons interact with a high-atomic-number target. These electrons are first emitted into an evacuated waveguide by thermionic emission from a cathode (Karzmark and Pering, 1973; Podgorsak, 2005) and are accelerated by non-conservative microwave fields. The microwave fields are produced by decelerating electrons in either a klystron or magnetron, which are evacuated devices that produce a retarding potential (Podgorsak, 2005). The electrons in medical linacs are generally accelerated to energies between (4 and 25) MeV. Once at the end of the waveguide, the trajectory of the electron beam is often changed and focused by a bending magnet. The shape of the resulting electron beam is approximately circular with a Gaussian spatial spread of about 1 mm FWHM. Following the bending magnet is the target, often made of tungsten. Typical targets are a few millimeters in thickness. The electrons interact with the target to produce a continuous bremsstrahlung spectrum with a maximum energy equal to the energy of the accelerated electrons.

Traditional linear accelerators further shape the photon beam using a flattening filter. This is a conical-like high-atomic-number structure that attenuates the center of the beam more than the outside to produce a flat field. Flattening filters are designed to produce a flat field at 10 cm depth in water and have various shapes based on the energy of the beam. As intensity modulation has become popular, some linear accelerators have been designed without flattening filters (Jeraj et al., 2004; Deng et al., 2004; Hrbacek et al., 2011). These machines rely on MLCs and dynamic delivery to produce the desired fluence patterns.

Linear accelerators are pulsed sources of radiation, meaning many short bursts of radiation are used during a treatment. These machines are usually operated with a pulse length between (1 and 5) μs and a repetition rate (pulses per second) between (5 and 500) Hz (Karzmark and Pering, 1973). Generally, the repetition rate is adjustable so that a single machine can produce beams with multiple dose rates. Typical dose rates for a machine with a flattening filter are between (100 and 1000) $\mathrm{MU} \cdot \mathrm{min}^{-1}$. Flattening-filter-free machines can achieve dose rates up to $2400\,\mathrm{MU} \cdot \mathrm{min}^{-1}$ (Hrbacek et al., 2011).

2.2.3.3 Spectroscopic characterization

Monte Carlo techniques MC simulation is the most popular method used to study the dosimetric characteristics of linear accelerator beams. Many authors have built complete models of linear accelerators using various MC codes (Mohan et al., 1985; Faddegon et al., 2008; Chaney et al., 1994; Lovelock et al., 1995; Rogers et al., 1995; Libby et al., 1999; Siebers et al., 1999; Sheikh-Bagheri and Rogers, 2002; Kry et al., 2006). It is known that differences exist among these codes, some examples of which are the methods of electron transport, bremsstrahlung cross sections, and variance reduction techniques (Siebers et al., 1999; Libby et al., 1999; Faddegon et al., 2008). As such, each MC code must be independently verified for modeling linear accelerators. Most often, these models are verified with percentage depth-dose and cross-beam profile measurements (Verhaegen and Seuntjens, 2003).

The present discussion will focus on the family of MCNP codes. DeMarco et al. (1998) used MCNP4a to generate phase-space data for a 6 MV photon beam from a Philips SL-15/25 accelerator. In a similar set of simulations, Lewis et al. (1999) used MCNP4b to generate phase-space data for a Philips 75/5 accelerator. Both of these groups compressed the phase-space data by using a point source approximation for subsequent dosimetric simulations. Siebers et al. (1999) performed an intercomparison of the EGS4 and MCNP4 codes in the generation of phase-space data for (6 and 18) MV photon beams from a Varian 2100C linear accelerator. Their results indicated differences in the absolute bremsstrahlung production for the two codes; however, these differences were not apparent after the normalization of the phase-space data. Kry et al. (2006) used a newer MCNP code, MCNPX, to model a Varian Clinac 2100 accelerator for the calculation of out-of-field doses.

These investigations have shown that, when properly used, MC is a powerful tool for simulating linear accelerators. However, no direct comparisons between measured and simulated clinical spectra have been made. This work builds upon the work of these other investigations by developing and verifying an MC model that can be directly compared to spectroscopic measurements of the same unit. In addition, this work aims to quantify the effect of spectroscopic differences on dosimetry using MC techniques.

Measurement techniques Measurements of linear accelerator spectra are uncommon due to the challenges posed by the high fluence rates that are characteristic of these machines. Various techniques have been used to reduce these fluence rates, thereby facilitating measurements. Faddegon et al. (1990; 1990) accomplished this by using a Vickers research accelerator that was operated with a beam current that was several orders of magnitude lower than clinical beam currents (50 fA versus ∼20 μA). This arrangement allowed for the direct measurement of spectra for 10 MeV to 30 MeV electron beams incident on various targets. While this group performed direct measurements, their method was restricted to machine parameters that are not achievable on a clinical unit.

Other groups have reduced fluence rates by inserting a target into the beam between the source and detector. O'Dell et al. (1968), Sherman et al. (1974), and Lambert et al. (1983), inserted deuterium targets into the primary beam and measured the photoneutron products from photodisintegration reactions. Cross-section data were used to infer the primary photon spectrum from these measured data; however, due to the relatively high binding energy of deuterium (2.22 MeV) this method was insensitive to lower-energy photons. Similar photodisintegration measurements were performed by Nakamura and Hirayama (1976) using different targets (e.g., ^{12}C, ^{89}Y, and ^{115}In). Archer and Wagner (1988) and Krmar et al. (1996; 2002) measured the transmission spectrum for various thicknesses of attenuating materials (e.g., lead and aluminum) and used iterative fitting techniques to deduce the incident bremsstrahlung spectrum. Finally, multiple authors have used a CS technique to characterize linear accelerator spectra (Levy et al., 1974, 1976; Landry and Anderson, 1991; Jessen, 1973; Brownridge et al., 1984; Bentley et al., 1967). The beams investigated by these authors were produced using accelerated electrons ranging from (2 to 25) MeV. Each of these investigators corrected their measurements for detector response; however, the particular methods of correction were not clearly delineated. After correcting for detector response, the scattered spectra were related to the bremsstrahlung spectra using the Klein-Nishina cross section and the energy-angle relationship based on the assumption that electrons are unbound and at rest.

This thesis work developed a technique to measure the spectra for modern linear accelerators. A method to correct these spectra for the CS relations, including bound and moving electrons, was developed.

2.3 CS spectrometry

Incoherent scattering dominates interaction cross sections for photons in the therapeutic energy range, which can be taken advantage of in measurements performed with CS spectrometry. The following sections discuss the theory of incoherent scattering and how a scattered spectrum is related to the unscattered spectrum using the CS spectrometry technique.

2.3.1 Incoherent scattering theory

2.3.1.1 Scattering from free electrons

Incoherent scattering from free electrons is well described by the Compton (1923) and Klein-Nishina (1929) (KN) formalisms. Using this classical treatment a photon with initial energy, E, that is scattered at an angle, θ, will have a single, unique scattered energy, E'. According to the principles of energy and momentum conservation, these variables are related by

$$E' = \frac{E}{1 + \frac{E}{m_0 c^2} \left(1 - \cos\theta\right)}, \tag{2.17}$$

where $m_0 c^2$ is the rest mass energy of an electron. The differential KN cross section, which gives the probability of a photon scattering into θ as a function of E, is given as

$$\frac{d\sigma}{d\Omega_\theta} = \frac{r_0^2}{2} \left(\frac{1}{1 + \alpha\left(1 - \cos\theta\right)}\right)^2 \left(1 + \cos^2\theta\right) \left(1 + \frac{\alpha^2 \left(1 - \cos\theta\right)^2}{\left(1 + \cos^2\theta\right)\left[1 + \alpha\left(1 - \cos\theta\right)\right]}\right), \tag{2.18}$$

where $\alpha = \frac{E}{m_0 c^2}$ and r_0 is the classical electron radius.

2.3.1.2 Scattering from bound electrons

Equations 2.17 and 2.18 are valid for the idealized case of free electrons; however, it is known that electrons are bound and not at rest (Jauncey, 1925; Du Mond, 1929). This affects the total CS cross section and the angular distribution of scattered photons. It also results in a broadened distribution of E' values for a given θ, known as Doppler broadening (DB). The effect that bound electrons have on a scattered photon is dependent on E, θ, and the material-dependent momentum distribution of electrons in the target, $n\left(\mathbf{p}\right)$. The Compton profile, $J\left(p_z\right)$, gives the component of $n\left(\mathbf{p}\right)$ along the scattering vector (defined in the z direction) as

$$J\left(p_z\right) = \int\limits_{p_x}\int\limits_{p_y} n\left(p_x, p_y, p_z\right)\, dp_x\, dp_y, \tag{2.19}$$

where p_z is the projection of the electron momentum on the scattering vector. This profile is considered in the determination of the scattered-photon energy, E'. According to the principles of energy and momentum conservation, E' is related to E, θ, and p_z by

$$p_z = -137 \frac{E - E' - \frac{EE'}{m_0 c^2}\left(1 - \cos\theta\right)}{\sqrt{E^2 + E'^2 - 2EE'\cos\theta}}, \tag{2.20}$$

where p_z is given in atomic units. The double-differential KN cross section, which gives the probability of a photon scattering into θ and E' as a function of E, is found by (Ribberfors and Berggren, 1982)

$$\frac{d^2\sigma}{dE'd\Omega_\theta} = \frac{r_0^2}{2}\left(\frac{E'}{E}\right)\left(\frac{m_0c^2}{\sqrt{E^2+E'^2-2EE'\cos\theta}}\right)\left(\frac{E}{E'}+\frac{E'}{E}-\sin^2\theta\right)J\left(p_z\right). \tag{2.21}$$

2.3.2 Spectra unfolding

CS spectrometry involves the measurement of a spectrum that has been incoherently scattered from a scattering element through a known angle, θ. The measured spectrum, $\Phi_m\left(E'\right)$, is then corrected for the Compton relations (i.e., KN cross section and energy-angle relation) to estimate the primary spectrum, $\Phi\left(E\right)$. Corrections for the Compton relations often assume scattering from free electrons. This has been shown to be acceptable for cases in which the primary spectrum varies slowly with energy (i.e., bremsstrahlung spectra) because DB is compensatory for photons of neighboring energies (Carlsson et al., 1989). Assuming free electrons, the primary spectrum is found as

$$\Phi\left(E\right) = \Phi_m\left(E'\right)\left(\frac{E'}{E}\right)^2\left(\frac{\mathrm{d}_e\sigma}{\mathrm{d}\Omega_\theta}\right)^{-1}, \tag{2.22}$$

where the energy shift is defined as in Equation 2.17. A more rigorous correction for incoherent scattering accounts for bound electrons. In this case, $\Phi\left(E\right)$ is unfolded from $\Phi_m\left(E'\right)$ according to

$$\Phi_m\left(E'\right) = \int \frac{d^2\sigma}{dE'd\Omega}\Phi\left(E\right)dE, \tag{2.23}$$

where the energy shift is defined as in Equation 2.20. This method, which involves a complicated unfolding technique, was used in this thesis work.

2.4 Treatment planning systems

The treatment planning system (TPS) is central to the success of a patient's treatment. It bridges the radiotherapy process between diagnostic imaging and treatment delivery. The most widely used and accurate TPSs are "model-based" systems (Papanikolaou and Stathakis, 2009). These model-based systems use various imaging modalities to create a virtual patient that is used to determine the geometric and radiological features of a treatment. Model-based TPSs compute the dose distribution using first principles and require both patient data and a model of the radiation field.

Common model-based systems can compute both dose and energy fluence distributions. Since dose is linearly proportional to energy fluence, it is convenient to describe delivered dose in these terms (i.e., normalize dose by energy fluence) (Ahnesjo and Aspradakis, 1999). Using this methodology, various authors have derived an energy-fluence-based monitor unit (MU) formalism (Mackie et al., 1996; Ahnesjo and Aspradakis, 1999). The formalism gives the dose rate ($\frac{D}{MU}$) at a position ($\overrightarrow{r}$) as

$$\frac{D\left(\overrightarrow{r}\right)}{MU} = \frac{\Psi\left(P\right)}{MU} \cdot \frac{D\left(\overrightarrow{r}\right)}{\Psi\left(P\right)}, \tag{2.24}$$

where $\Psi\left(P\right)$ is the energy fluence at a point, P. The normalized dose, $\frac{D(\overrightarrow{r})}{\Psi(P)}$, is calculated by the TPS (e.g., via convolution/superposition, MC) and is converted to units of dose-per-monitor-unit by applying a phantom-independent calibration coefficient, $\frac{\Psi(P)}{MU}$. This calibration coefficient is defined as

$$\frac{\Psi\left(P\right)}{MU} = \frac{\left(\frac{D(\mathrm{ref})}{MU}\right)_{\mathrm{meas}}}{\left(\frac{D(\mathrm{ref})}{\Psi(P)}\right)_{\mathrm{calc}}}, \tag{2.25}$$

where $\left(\frac{D(\text{ref})}{MU}\right)_{\text{meas}}$ is the measured dose-per-monitor-unit and $\left(\frac{D(\text{ref})}{\Psi(P)}\right)_{\text{calc}}$ is the calculated dose-per-energy-fluence, both of which are determined using the same reference conditions (Mackie et al., 1996; Smilowitz, 2002).

One strength of this formalism is that it can be used with any model-based calculation method, as long as that method gives dose per reference energy fluence (Ahnesjo and Aspradakis, 1999). In addition, it allows for the use of flexible reference conditions. This method was used by Smilowitz for the MC-based phantom-independent calibration of a ^{60}Co unit (Smilowitz, 2002). Smilowitz found that the field's calibration coefficient did not change with the materials that were tested. Furthermore, the calibration coefficient did not change when the reference conditions (depth or field size) were changed. This work thus verified that the energy fluence calibration is in fact phantom- and condition- independent.

The most complicated component of the energy-fluence-based monitor unit formalism is the beam model, which is used in the calculation of dose and energy fluence (Mackie et al., 1996). The energy spectrum, which is one of approximately 30 parameters that describes the beam model (Starkschall et al., 2000), is often estimated based on depth-dose measurements (Mackie et al., 1985; Starkschall et al., 2000). Direct measurement of the spectrum would therefore be a valuable verification of this portion of the beam model, especially since the phantom-independent calibration coefficient is dependent on its accuracy.

Chapter 3

General MCNP5 investigations

Most Monte Carlo (MC) codes undergo rigorous benchmarking to verify the accuracy and implementation of the physics models that they use. However, because these codes offer many complicated techniques, it is challenging to sufficiently benchmark a code for all of its potential uses. This chapter presents some inconsistencies and deficiencies in the Monte Carlo N-Particle (MCNP5) code that were discovered and addressed throughout this thesis work.

3.1 Variance reduction

Variance reduction (VR) techniques are used to increase the efficiency of a simulation. While VR is critical to many problems, the use of certain techniques can lead to inaccurate results if necessary precaution is not taken. The following section addresses two of the VR techniques used in this work, and some conditions under which they produce inaccurate results.

3.1.1 Electron energy cutoff

In general, coupled photon-electron transport (called `mode p e` in MCNP5) should provide the most accurate simulation of a radiation transport problem. However, electron transport is computationally expensive because, unlike neutral particles which undergo relatively infrequent collisions, electrons are constantly interacting with media via Coulombic forces. In some situations, full electron transport does not appreciably affect simulation results, and it is more efficient to transport photons only (i.e., `mode p`). In this mode, electrons are not completely neglected. Rather, they are treated with a thick-target bremsstrahlung (TTB) model in which electrons are assumed to come to rest locally, emitting bremsstrahlung photons in the process. For problems in which explicit electron transport is important it is often acceptable to follow only those electrons with energies above a particular threshold. In MCNP5, this energy cutoff is specified with the second entry on the `CUT:e` card.

MCNP5 allows for the presence of electron energy cutoffs in photon-only problems. Because electrons are not transported in `mode p`, the `CUT:e` card would not be expected to affect simulation results. This hypothesis was tested in a series of `mode p` simulations in which a 1 MeV point source was positioned at the center of a large water sphere (10 m in radius). In each simulation, a unique electron energy cutoff between (0 and 1) MeV was used. The effect of the electron cutoff was determined by the relative number of bremsstrahlung photons that were created with the TTB model.

The results of this study, shown in Figure 3.1, indicate that the value of the electron energy cutoff affects the creation of bremsstrahlung photons. This suggests that, while electrons are not explicitly transported in `mode p`, they are created and transported just far enough to produce bremsstrahlung photons. If the electron energy cutoff is sufficiently high, the electrons and their progeny bremsstrahlung photons are not produced. Depending on the particular tally used in a problem, the loss of bremsstrahlung photons may be

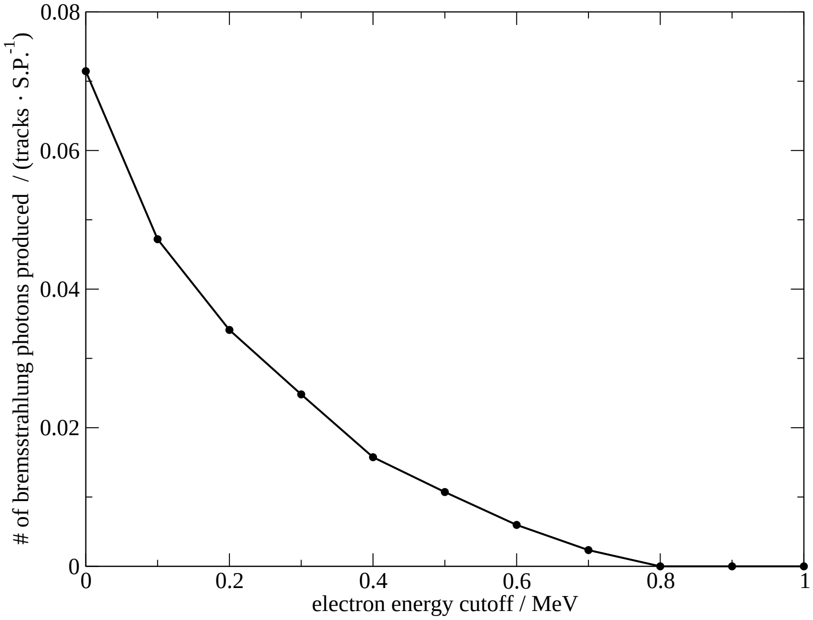

Figure 3.1: Number of bremsstrahlung photons produced in water as a function of the electron energy cutoff. This graph reflects results of `mode p` simulations for a 1 MeV photon point source positioned in a large water sphere.

inconsequential; however, these findings indicate that care must be taken when using the `CUT:e` card in photon-only problems.

3.1.2 DXTRAN technique and electron importance

The DXTRAN technique is the only technique in MCNP5 that allows a particle's scattering angle to be biased. It is particularly useful in problems where a region is inadequately sampled due to the rarity of scatter in its direction. To use this method, a sphere that encloses the undersampled region is overlaid on the simulation geometry. When a particle collides anywhere in the problem, it is split into a DXTRAN particle and a non-DXTRAN particle. The DXTRAN particle is deterministically scattered towards the DXTRAN sphere. It is transported to the sphere without collision and with an appropriately reduced weight. The non-DXTRAN particle is treated normally and undergoes no weight reduction. Due to the severe angular dependence of the Compton-scattering (CS) spectrometry method, many simulations in this work incorporated this technique. The following section discusses one problem associated with DXTRAN spheres in `mode p e` problems.

The compatibility of DXTRAN spheres with `mode p e` problems was investigated using a simple geometry that mimicked the CS spectrometry simulations performed in this thesis work. A 1 MeV photon point source was positioned 100 cm from an aluminum scattering rod. The source was mathematically collimated to emit photons uniformly within a cone with a 1° half angle. Collisions were forced in the scattering rod. A 5 cm-diameter DXTRAN sphere was positioned 242 cm from the scattering rod at a 30° angle relative to the axis of the source emission cone. Using the F4 tally, the average photon fluence was scored in a vacuum cylinder (5 cm in both diameter and height) that was placed directly behind the DXTRAN sphere. All of the cells except for the scattering rod were filled with vacuum. Two simulations were run using `mode p e`. In the first simulation, the electron importance was unity in all cells of the problem. In the second simulation, the electron importance in the regions outside of the scattering rod was changed to zero. In both simulations, the photon importance was unity in all cells.

Due to the simulation geometry and type of tally used (i.e., a photon-based tally), the only particles that could contribute to the tally were photons from the scattering rod. Thus, the presence of electrons anywhere outside of the scattering rod would not affect the physics of the problem. When the electron importance outside of the scattering rod was unity, the F4 tally was nonzero (5.57634×10^{-6} particles $\cdot$ cm^{-2}). However, when electrons were killed in these regions, the tally was zero; in fact, no DXTRAN particles were created under these circumstances. The MCNP5 v1.50 release notes (Booth et al., 2008) state that too many DXTRAN particles are rouletted when a cell has an electron importance of zero but a photon importance that is nonzero. Many VR methods use the rouletting technique to kill low-weight particles while conserving the overall weight of the system. The comments in the MCNP5 v1.50 release notes are consistent with the findings in this work. According to these results, it is recommended that the electron and photon importances are set to the same value in problems where DXTRAN spheres are used.

3.2 Doppler broadening

Incoherent scattering from free electrons is well described by the Compton (1923) and Klein-Nishina (1929) (KN) formalisms. Using this classical treatment, a photon that is scattered at a particular angle will have a single, unique scattered energy. However, it is known that atomic electrons are bound and not at rest (Jauncey, 1925; Du Mond, 1929), which manifests as a reduction in the total CS cross section, a modification in the angular distribution of scattered photons, and a broadened distribution of scattered-photon energies at a given scattering angle, known as Doppler broadening (DB).

Accurate characterization of incoherently-scattered photons is important for kilovoltage and megavoltage spectroscopic applications. In this energy range, CS dominates interaction cross sections for typical detector materials, such as silicon. As MC methods have become popular for verifying and correcting spectroscopic measurements (Faddegon et al., 1990; Sood and Gardner, 2004; Beach, 2005; Fehrenbacher et al., 1996), many general-purpose MC codes have implemented routines to consistently account for the effects of bound electrons (Namito et al., 1994; Longo et al., 2008; Sood, 2004; Ye et al., 2006). This work focused on the implementation of DB in the incoherent scattering model in MCNP5, which was developed by Los Alamos National Laboratory (Los Alamos, New Mexico). DB was first included in MCNP5 v1.14 and was implemented according to the methodology described by Namito et al. (Namito et al., 1994; Sood, 2004; Sood and White, 2004). Although the fundamental methodology has been consistent in all versions, the practical implementation of DB has changed with each subsequent release of MCNP5. This work investigated the DB model in the two most recent versions of MCNP5 (v1.51 and v1.60) and a modified form of v1.60 (v1.60m).

3.2.1 DB theory

DB is a process in which the pre-collision momentum of a bound target electron affects the momentum of a scattered photon. The effect of DB is a distribution of scattered-photon energies for a particular incident energy, E, and scattering angle, θ. The shape of the broadened energy spectrum is dependent on E, θ, and the material-dependent momentum distribution of electrons in the target, $n(\mathbf{p})$. The Compton profile, $J(p_z)$, gives the component of $n(\mathbf{p})$ along the scattering vector (defined in the z direction) as (Cooper, 1985)

$$J(p_z) = \int_{p_x}\int_{p_y} n(p_x, p_y, p_z)\, dp_x\, dp_y, \tag{3.1}$$

where p_z is the projection of the electron momentum on the scattering vector. This profile, which contains data for each electron subshell, is considered in the determination of the scattered-photon energy, E'. According to the principles of energy and momentum conservation, E' is related to E, θ, and p_z by

$$p_z = -137\frac{E - E' - \frac{EE'}{m_0c^2}(1-\cos\theta)}{\sqrt{E^2 + E'^2 - 2EE'\cos\theta}}, \tag{3.2}$$

where m_0c^2 is the rest mass energy of an electron, and p_z is given in atomic units. The DB model in MCNP5 makes use of Equation 3.2 in the calculation of scattered-photon energies (Sood, 2004).

3.2.2 Monte Carlo techniques

A set of simulations was developed to test the DB feature in three versions of MCNP5: v1.51 (released in 2009), v1.60 (released in 2010), and an in-house modified edition of v1.60 (called v1.60m) (Bartol and DeWerd, 2012). All calculations were performed using the MCPLIB04 photon cross-section library (White, 2003), in which the electron subshell data for incoherent scattering are presented in the form of a probability density function (PDF).

In MCNP5, these data are sampled using a binary search to select the subshell where CS takes place. In order to be sampled accurately using a binary search, data must be organized as a cumulative density function (CDF). Thus, MCPLIB04 provides the electron subshell data in an inappropriate form for the prescribed sampling technique; however, these data are still used in v1.51 and v1.60. This problem was addressed in a new version of MCNP5, v1.60m, in which the source code was altered to calculate the CDF from the PDF data. In v1.60m, these CDF data were used to sample the electron subshell.

Each version of the code was tested using an identical set of simulations that investigated DB at scattering angles of 15°, 30°, and 45°. For all calculations, the model geometry consisted of a 4 mm-thick slab of silicon ($Z = 14$) surrounded by vacuum. A monoenergetic point source emitted photons in a direction normal to the surface of the slab. For each θ, simulations were run for multiple energies between 200 keV and 800 keV. The forced-collision variance reduction technique was used in the silicon slab.

An F1:p current tally, which scores the number of photons crossing a specified surface, was used at the exit of the slab. This tally was binned by energy using 0.25 keV-wide bins. Only singly scattered photons that were scattered at an angle within ±0.01° of θ were scored. This angular acceptance criterion ensured that the energies of all of the scoring photons fell within a maximum of two bins when using the classic CS treatment. As such, any photons that scored outside of these two bins were attributed to the DB effect. With these specifications, the tally gave the differential energy spectrum of photons normalized per starting particle (S.P.) for scattering angles within ±0.01° of θ.

Analytical spectra were calculated for comparison with the MC simulations. Using Equation 3.2, E' was calculated for a given E, θ, and p_z. The silicon Compton profile data from Biggs et al. (1975) were used. These data, which are tabulated as a function of p_z, were normalized to create a PDF for p_z. Thus, for a given E and θ, a series of E' values

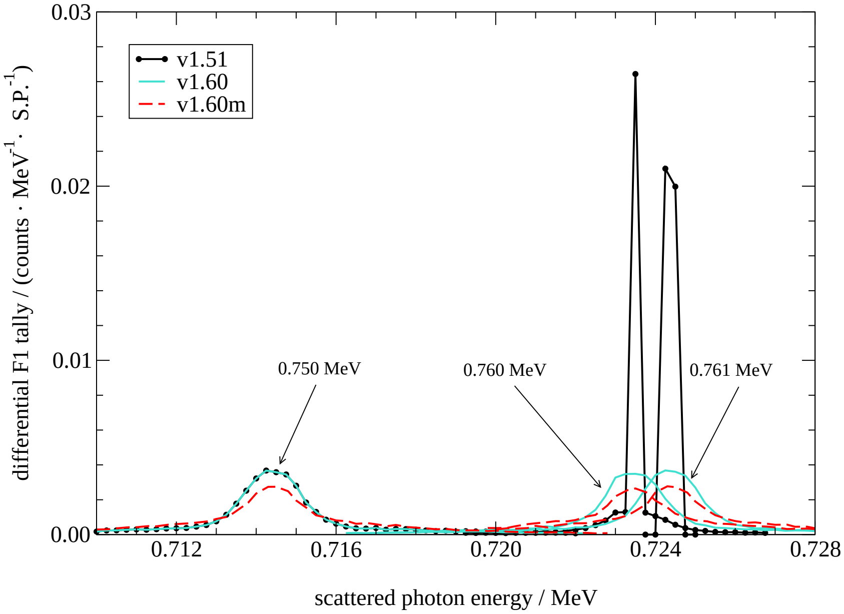

Figure 3.2: MC-calculated spectra for three incident photon energies scattered at 15° in silicon. The energies indicated by the arrows represent the initial energy of the source. The differential F1 tally gives the spectrum of photons per starting particle (S.P.) that were scattered at an angle of $(15 \pm 0.01)°$.

was calculated, with each E' corresponding to a particular p_z. To determine the shape of the DB spectrum, the occurrence of each E' was weighted by the appropriate PDF value.

3.2.3 Results

The spectra calculated using all three versions of MCNP5 are shown in Figures 3.2, 3.3, and 3.4 for scattering angles of 15°, 30°, and 45°, respectively. The analytical spectra are shown only in Figure 3.6, which gives a magnified view of the spectra for 30° scattering.

3.2.3.1 MCNP5 v1.51

The spectra determined using v1.51 exhibited similar behavior for all scattering angles investigated. For each θ there was an incident photon energy above which broadening was not modeled (approximately 760 keV, 384 keV, and 260 keV for 15°, 30°, and 45°,

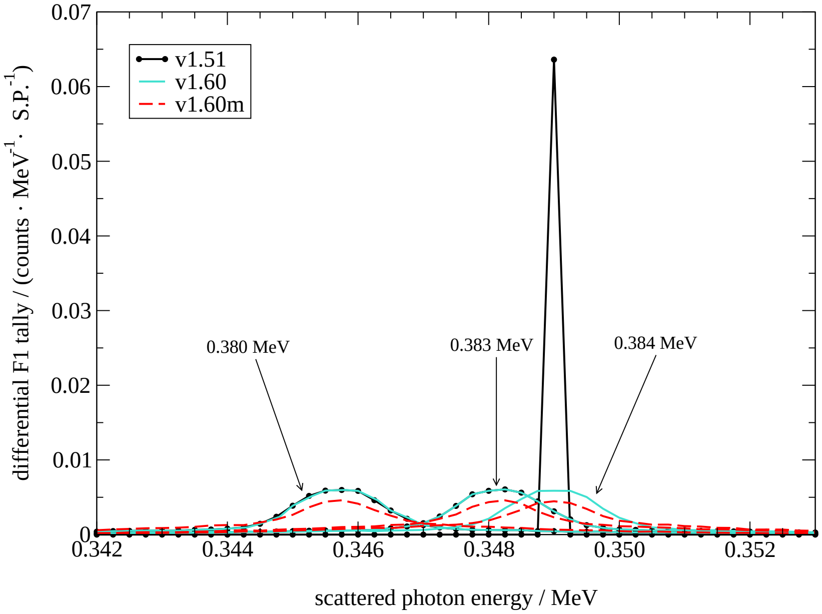

Figure 3.3: MC-calculated spectra for three incident photon energies scattered at 30° in silicon. The energies indicated by the arrows represent the initial energy of the source. The differential F1 tally gives the spectrum of photons per starting particle (S.P.) that were scattered at an angle of $(30 \pm 0.01)°$.

respectively). This discontinuity, which is briefly addressed in the release notes of MCNP5 v1.60 (Brown et al., 2010), resulted from the limited range of incoherent scattering function data, $S(\nu, Z)$, contained in the photon data library. These data are used to account for the effects of bound electrons on the angular distribution of scattered photons. Prior to entering the DB algorithm in MCNP5, θ is sampled according to a KN distribution that has been modified by $S(\nu, Z)$. This is a two-step process in which θ is: (1) sampled according to the KN distribution and (2) accepted or rejected according to the corresponding $S(\nu, Z)$. When θ is accepted, the DB algorithm should be called.

MCNP5 v1.51 always properly performs step (1) and uses θ to locate $S(\nu, Z)$ in the data library. In MCPLIB04, $S(\nu, Z)$ is tabulated for each element, Z, as a function of the

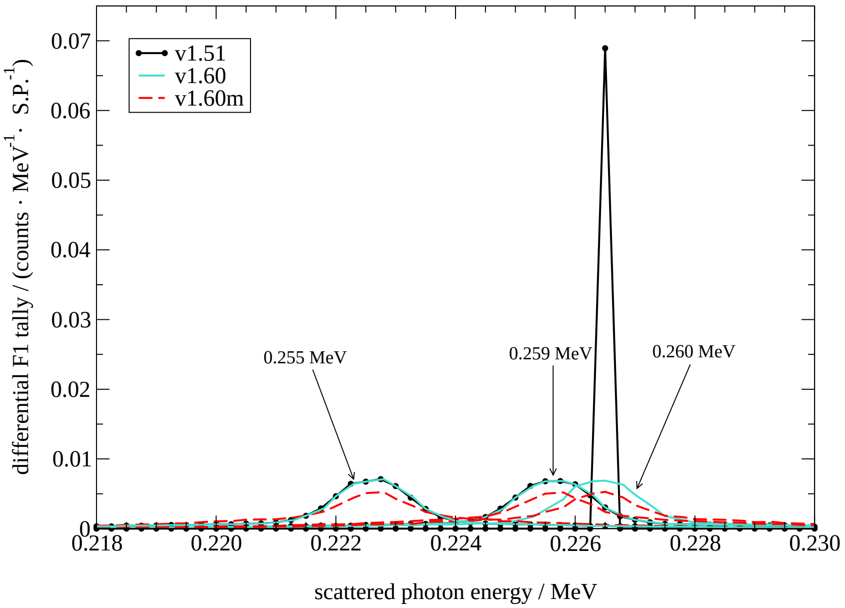

Figure 3.4: MC-calculated spectra for three incident photon energies scattered at 45° in silicon. The energies indicated by the arrows represent the initial energy of the source. The differential F1 tally gives the spectrum of photons per starting particle (S.P.) that were scattered at an angle of $(45 \pm 0.01)°$.

recoil electron momentum, ν. This is defined as

$$\nu = \frac{\sin\left(\frac{\theta}{2}\right)}{\lambda}, \tag{3.3}$$

where λ is the wavelength of the incident photon and ν is given in natural units. Incoherent scattering function data are provided for $(0 \leq \nu \leq 8)\,\text{Å}^{-1}$. When ν falls within this range, MCNP5 performs step (2) and, if θ is accepted, the DB algorithm is called. However, when ν is outside of the tabulated range, step (2) is not performed due to the lack of $S\,(\nu, Z)$ data, and MCNP5 simply accepts θ from step (1). In this case, although θ is accepted properly, v1.51 does not proceed to the DB algorithm, and the KN free electron approximation is applied. Figure 3.5 shows the incident photon energy at which this error occurs as a function of θ. The data in Figure 3.5 were calculated using Equation 3.3 for ν equal to $8\,\text{Å}^{-1}$.

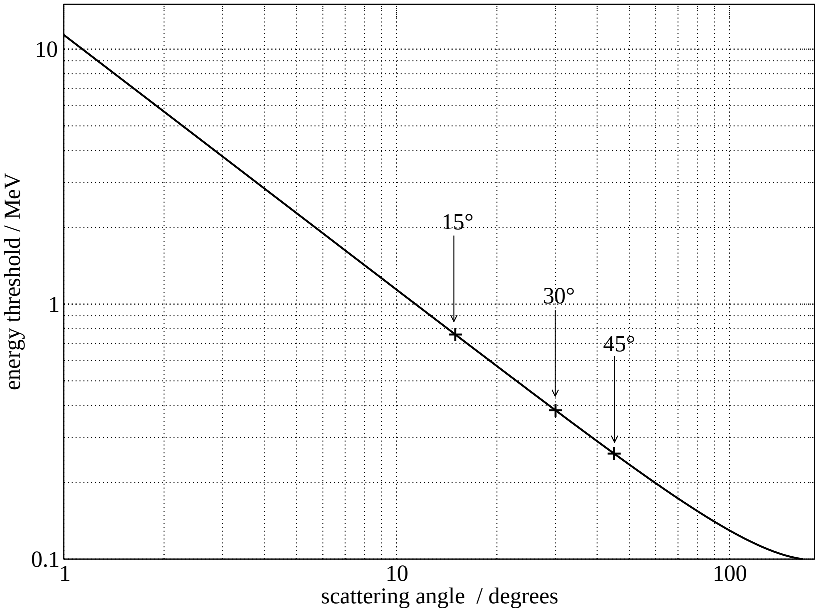

Figure 3.5: Energy above which MCNP5 v1.51 does not model DB as a function of scattering angle. The plus signs highlight the scattering angles that were investigated in this work. Note that the figure is plotted on a logarithmic scale. These data were calculated using Equation 3.3 for ν equal to $8\,\text{Å}^{-1}$.

3.2.3.2 MCNP5 v1.60

The spectra calculated using v1.60 indicate that energy broadening was modeled for all E and θ tested. This confirms that v1.60 calls the DB algorithm any time θ is accepted, regardless of the existence of $S(\nu, Z)$ for the particular E and θ used. The amount of energy broadening that is modeled with v1.60 is the same as that seen with v1.51, indicating that the same DB model is used in both versions.

3.2.3.3 MCNP5 v1.60m

Figure 3.6 shows a magnified view of the spectra that were calculated for 30° scattering with all three versions of the code, with the analytically calculated spectra shown for comparison. The other scattering angles showed similar behavior. From Figure 3.6, it is clear that more energy broadening was modeled in v1.60m than in v1.51 and v1.60. Furthermore, the shapes

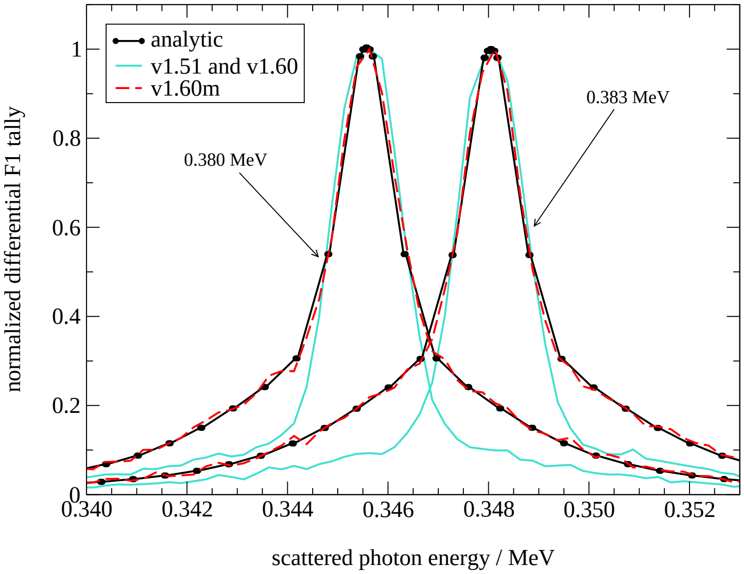

Figure 3.6: Magnified view of MC-calculated spectra for 30° scattering in silicon. The analytical spectra are shown for comparison. The energies indicated by the arrows represent the initial energy of the source. The differential F1 tally gives the spectrum of photons per starting particle that were scattered at an angle of (30 ± 0.01)°. The spectra have been normalized at the energy for which p_z equals 0 (i.e., the center of each spectrum).

of the analytically calculated spectra and the MC-calculated spectra agreed well, indicating that v1.60m accurately models DB. These results show that the form of the electron subshell data has a substantial effect on the scattered spectrum. Analysis of the MCPLIB04 data library shows that, of the five electron subshells in silicon, only three subshells ($1s^2$, $2p^6$, and $3p^2$) are sampled when used with v1.51 and v1.60. All five subshells are sampled when MCPLIB04 is used with v1.60m. The consequence of the inappropriate sampling in v1.51 and v1.60 is shown in Table 3.1, which compares the relative sampling of each subshell when using the PDF and CDF data.

3.2.4 Recommendation

Since it was first introduced, the practical implementation of DB in MCNP5 has changed with each release of the code. This work investigated the DB model in the two most recent

Table 3.1: Probability of sampling each subshell in silicon with a binary search using data in CDF (correct) and PDF (incorrect) form.

	Sampling Probability		
Subshell	Using CDF data	Using PDF data	% Error for PDF data
$1s^2$	$\frac{2}{14}$	$\frac{2}{14}$	0
$2s^2$	$\frac{2}{14}$	0	-100
$2p^6$	$\frac{6}{14}$	$\frac{4}{14}$	-33.3
$3s^2$	$\frac{2}{14}$	0	-100
$3p^2$	$\frac{2}{14}$	$\frac{8}{14}$	+300

versions of the code (v1.51 and v1.60). In v1.51, DB is not modeled for combinations of E and θ that result in recoil electron momenta beyond the range of data stored in the library. This was addressed in MCNP5 v1.60, in which energy broadening is modeled for all combinations of E and θ. However, v1.60 models only partial energy broadening when used with the MCPLIB04 photon data library, due to the inappropriate form of the electron subshell data. Modification of the source code to correctly sample the electron subshell resulted in a more accurate DB model.

The errors found with v1.51 (below the energy threshold) and v1.60 may be eliminated by changing the form of the electron subshell data that is used. In response to this study, Los Alamos National Laboratory has released a new photon data library, MCPLIB84 (White, 2012), which contains subshell sampling data in CDF form. It is recommended that MCNP5 v1.60 be used with this new data library when accurate incoherent scatter modeling is required.

3.3 Phase-space files

A phase-space file (PSF) is a collection of data that specifies the type, energy, position, and direction of particles that are crossing a particular plane. Phase-space files are often used in external beam studies in which the source and treatment head are held constant,

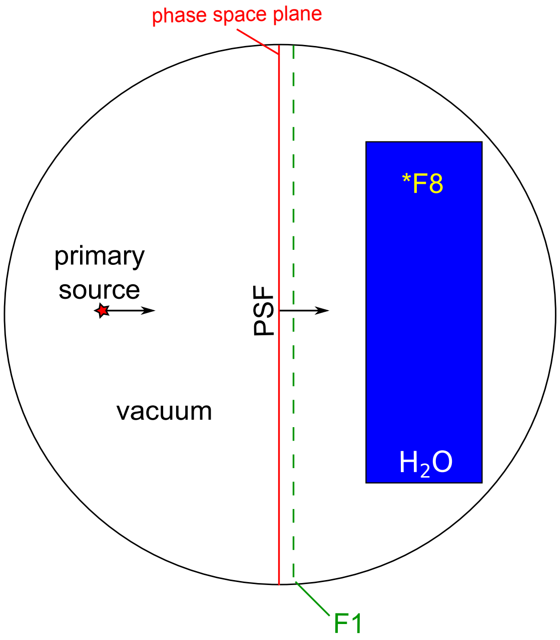

Figure 3.7: Geometry and scoring planes for the two simulations that were run to test the implementation of PSFs in MCNP5. Only one source (the primary source or PSF) was used in each simulation.

but the subsequent parts of the geometry change. MCNP5 allows users to write and read PSFs with the *source surface write* (`SSW`) and *source surface read* (`SSR`) cards. This work investigated the implementation of PSFs in MCNP5 using a simple simulation geometry.

3.3.1 Monte Carlo techniques

Two simulations were run to test the implementation of PSFs in MCNP5 v1.60. These simulations were run with coupled photon and electron transport and used the MCPLIB84 and EL03 data libraries. The simulation geometry, which consisted of a slab of water inside of a vacuum sphere, was identical for the two simulations (see Figure 3.7). The source definitions for the two simulations were different.

In the first simulation, a point source was positioned 12 cm from the surface of the water slab. The source emitted the 6 MV photon spectrum from Sheikh-Bagheri and Rogers (2002) and was directed normal to the surface of the water slab. The number of source particles

(`NPS`) run for this simulation was 2×10^7. Using the `SSW` card, a PSF was written at a plane between the source and water slab. Only particles that were directed towards the water were recorded in the PSF. In addition to the PSF, two quantities were scored. First, the F1 current tally was scored at a plane between the PSF plane and the water slab. This tally was binned by energy and cosine to look at the spectrum that was incident on and backscattered from the water. Second, a *F8 energy deposition tally was used in the water slab to determine the total energy deposited.

In the second simulation, the source information was read from the PSF using the `SSR` card. The simulation was run for an `NPS` of 2×10^7, and tallies that were identical to those in the first simulation were used. No variance reduction was used for either simulation.

3.3.2 Results

The F1 current tally results are shown in Figure 3.8. This figure focuses on the low-energy region of the spectrum because no discrepancies were observed at higher energies. In Figure 3.8, the spectra that were incident on (solid line) and backscattered from (dashed line) the water slab are shown.

The photons from the primary source were nondivergent and unscattered prior to being written to the PSF. Due to the simplicity of this model, the primary source and PSF were expected to be identical. In MCNP5, the PSF is written in a binary format. A FORTRAN program was used to read and display the phase-space information for each particle. Analysis of the first 50 particles from the primary source and in the PSF indicated that the two sources were indeed identical. This was also reflected in the F1 tally that was incident on the water slab, as shown in Figure 3.8. Since the spectra incident on the water slab were identical in both simulations, the backscattered spectra should also have been identical; however, it is evident from Figure 3.8 that the backscattered spectra were different. The spectrum from the PSF simulation had a larger 511 keV peak than did the

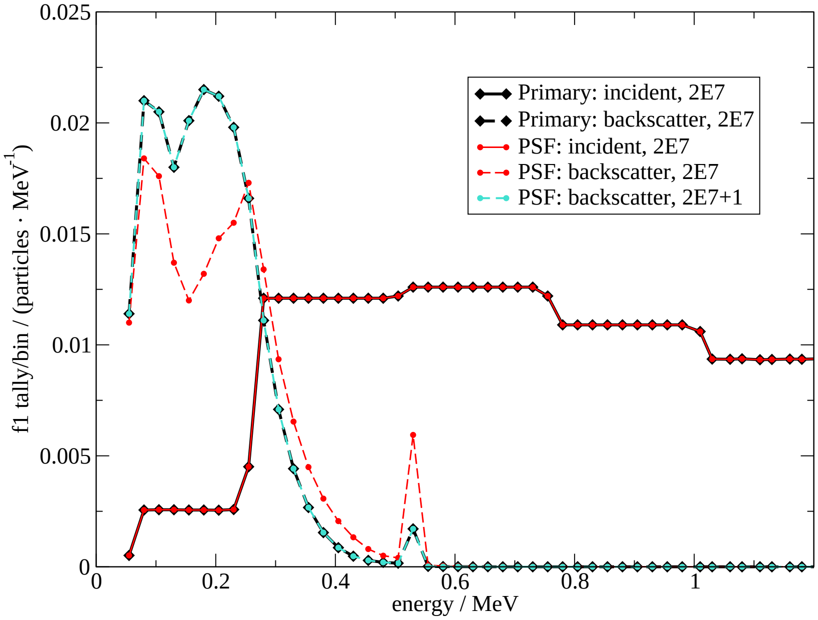

Figure 3.8: F1 current tally for a 6 MV point source directed at a water slab. The curves show the incident and backscattered F1 tallies for the primary source case (diamonds) and the PSF case (circles). The legend designates how many particles were run for each simulation.

straightforward simulation. In addition, the shape and magnitude of the spectrum below the 511 keV peak was different. The energy deposition results are shown in Table 3.2. Like with the F1 tally results, there was significant disagreement between the results of the two simulations.

Two potential causes were investigated in the diagnosis of this problem. Both tests involved the investigation of photons that are created in the water slab. First, the same two simulations were run with photon transport only. In these simulations, the TTB approximation, which MCNP5 uses as a default in photon-only problems, was turned off. This tested if the bremsstrahlung photons that were created in the original set of simulations were being inappropriately weighted when using the PSF. The second set of simulations used a lower-energy polyenergetic photon source. The maximum energy of this source was 1 MeV, which would ensure that pair production would not occur. This tested if the annihi-

Table 3.2: Energy deposition tally results for PSF test.

Source	`NPS`	*F8 tally ($\mathrm{MeV} \cdot \mathrm{S.P.}^{-1}$)	Difference from point source (%)
Point source	2×10^7	$0.701867 \pm 0.03\%$	—
PSF	2×10^7	$1.153180 \pm 0.02\%$	64.30
PSF	$2 \times 10^7 + 1$	$0.701869 \pm 0.03\%$	0.0003

lation photons that were created in the original set of simulations were being inappropriately weighted. The results of both of these tests were similar to those of the initial simulations, thus indicating that neither the TTB model or annihilation photons were responsible for the inconsistencies.

A final test was run in which, rather than using the same `NPS` as was used to write the PSF, one extra particle was run (i.e., $2 \times 10^7 + 1$). The results of this simulation are shown in Figure 3.8 and Table 3.2. When running one extra particle, the discrepancies between the two simulations were eliminated for both tallies. This solution is not understood because the uncertainty in the simulation should be negligibly affected by running one additional history.

3.3.3 Recommendations

The results of this study indicate that the use of PSFs may not be reliable in MCNP5. Although the PSF that was created did contain the correct information, there was a problem in how the PSF particles were treated in the subsequent run. This problem appeared only for cases in which the number of particles used to write the PSF and call the PSF were the same. When the `NPS` was increased by one, this problem did not persist. Because of this unexplained inconsistency, PSFs should be used with caution in MCNP5. It is recommended that more particles be used in subsequent simulations than were used to create the PSF.

Chapter 4

General MC and measurement methods

This thesis work involved the simulation and measurement of two megavoltage photon sources. While the specific techniques used to characterize each source were slightly different, the general methods were consistent. This chapter addresses the methods common to the characterization of both sources.

4.1 Monte Carlo methods

Monte Carlo (MC) investigations for this work were performed using Version 5.1.60 of the Monte Carlo N-Particle code (MCNP5) (X-5 Monte Carlo Team, 2005) with the MCPLIB84 photon (White, 2012) and EL03 electron (Adams, 2000) cross-section libraries . The Integrated Tiger Series (ITS) transport option was used for simulations that included electron transport because previous works have shown it is more accurate than the default electron transport algorithm in MCNP (Jeraj et al., 1999; Scarantino et al., 2005; Davis, 2009).

4.1.1 CS system characterization

This work used a simulation technique to characterize the response of the reverse-electrode germanium (REGe) detector to a range of photon energies. These simulation data were compiled in a detector response function (DRF) that was used to correct measurements for detector efficiency and artifacts introduced by the measurement system. The following section discusses the simulation geometry and methods that were used to generate these data.

4.1.1.1 Simulation geometry

In order to simulate a detector response that will accurately correct measurements, the simulation geometry must reflect measurement conditions. For basic measurement systems, the DRF accounts for the detector only, excluding the effects that shielding and collimation have on the spectrum (Beach, 2005; Beach and DeWerd, 2007); however, for Compton-scattering (CS) spectrometry, the components of the scattering geometry have a substantial effect on the spectrum. To account for these effects, the DRF simulations for this work included a model of the entire measurement system, including the detector, its shielding, and the scattering rod.

All measurements in this work used the same detector and shielding components, both of which were modeled in MCNP5. The REGe detector model was modified from an MC model of the same detector that was created by Beach at the UWMRRC (2005). This older model included the coaxial germanium crystal, electrodes, aluminum crystal holder, and aluminum housing. To verify the general construction of Beach's model, a radiograph of the REGe detector was taken using the Artis Zeego multi-axis C-arm CT system (Siemens AG, Erlangen, Germany) at the University of Wisconsin. This radiograph, shown in Figure 4.1, indicated that the detector had more components than were included in Beach's model. Following these findings, the detector geometry was modified by the addition of a signal

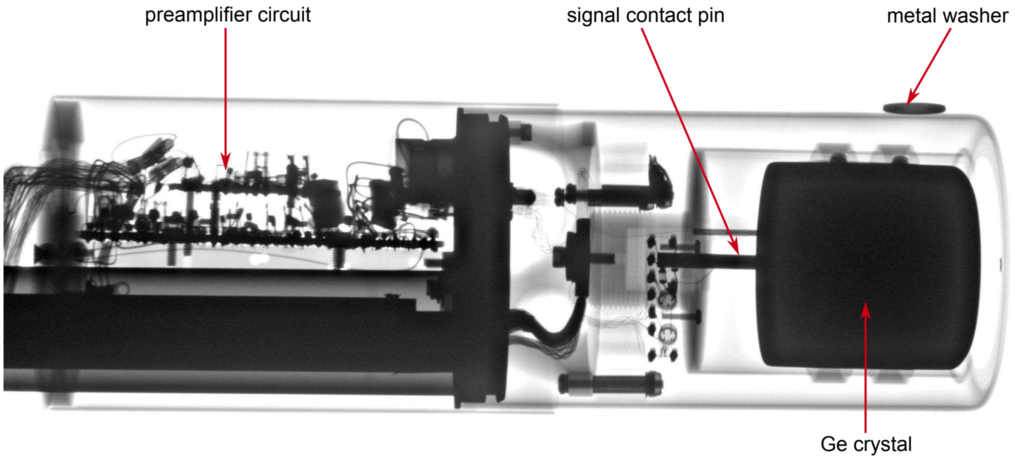

Figure 4.1: Side-view radiograph of the REGe detector. The metal washer was used as a reference for positional orientation.

contact pin and preamplifier. The signal contact pin (Ostby Barton [Warwick, RI], model IP125J) was a gold-plated beryllium-copper probe that was modeled in the coaxial core hole of the detector to provide a connection between the inner electrode and preamplifier. As an approximation, the preamplifier was modeled as a homogeneous aluminum cylinder behind the detector. These components were neglected in Beach's model because they were expected to have a negligible effect on low-energy photon detection; however, since high-energy photons undergo substantial backscatter from post-detector materials, they were necessary for the present work. Figure 4.2 shows the detector model that was developed for this work, with the model developed by Beach shown for comparison. These figures were rendered using MCNP5's Visual Editor (VisEd) software. The detector was modeled inside a cylindrical lead shield, as shown in Figure 4.3, to simulate measurement conditions. The details of the lead shield design are discussed in Section 4.2.1.2.

The source and scattering geometry (e.g., scatterer-to-detector distance, scattering angle) were different for each measurement. Thus, a separate DRF was created for each unique measurement configuration. For the DRF simulations that were applied to ^{60}Co measurements, an isotropic cylindrical volume source (2 cm in diameter, 2 cm in height)

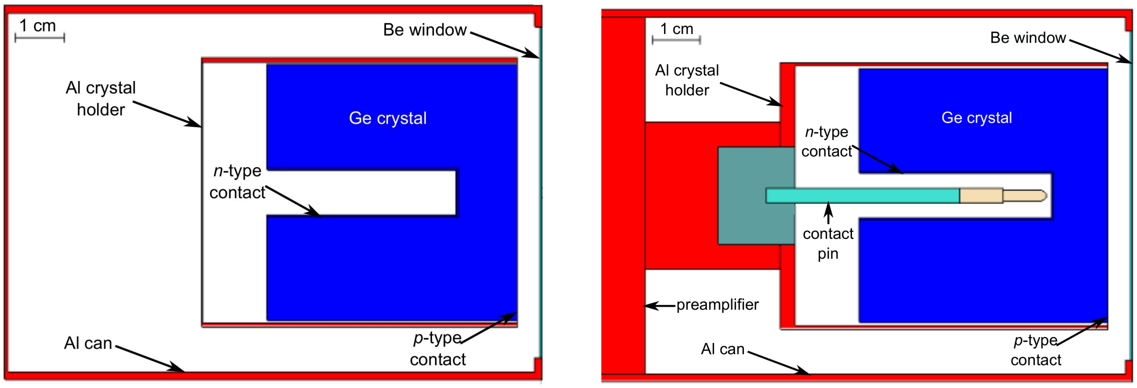

(a) (b)

Figure 4.2: VisEd rendering of the REGe detector created for (a) Beach's work and (b) this work.

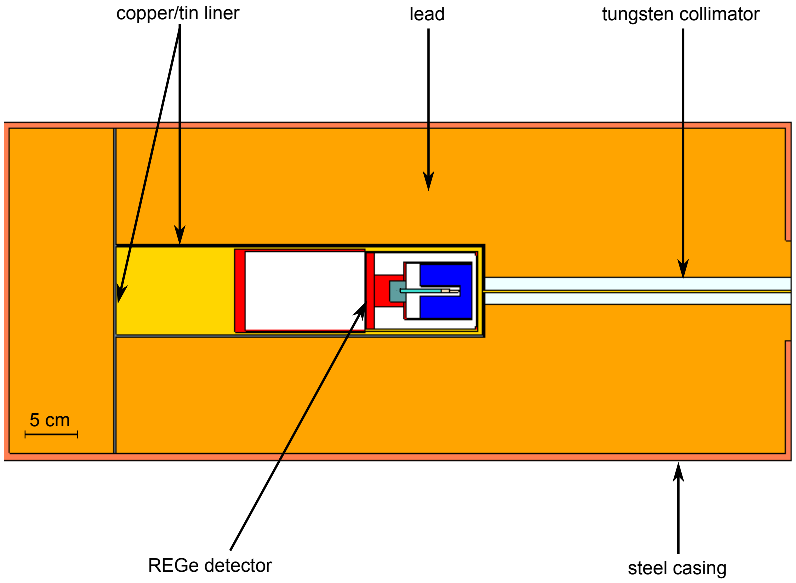

Figure 4.3: VisEd rendering of the REGe detector inside the lead shield.

was modeled. For the linear accelerator DRF simulations, a mathematically collimated point source was used. In all cases, the scattering rod was positioned at the intersection of the central axis of the beam and the detector's collimating aperture.

4.1.1.2 Variance reduction

Variance reduction (VR) techniques are used to increase a simulation's precision for a given number of particle histories. Without VR, the DRF simulations in this work would have required a prohibitive number of particles to achieve sufficient statistical precision. This work used the forced-collision and DXTRAN sphere VR techniques (X-5 Monte Carlo Team, 2005).

The forced-collision technique is often used to sample collisions in optically thin cells where interactions are not likely to occur (X-5 Monte Carlo Team, 2005). Any photon entering a forced-collision cell is split into an uncollided part and a collided part. MCNP5 calculates the weights of the split particles by determining the expected weight crossing the cell and the expected weight colliding within the cell. These weights are then assigned to the uncollided and collided particles, respectively, while conserving the weight of the initial photon. In this work, the forced-collision technique was used to increase the number of photons that interacted in the scattering rod.

The DXTRAN technique is the only technique in MCNP5 that allows a particle's scattering angle to be biased. It is particularly useful in problems where a region is inadequately sampled due to the rarity of scatter in its direction. MCNP5's implementation of this technique is discussed in detail in Section 3.1.2. In the DRF simulations, one set of DXTRAN spheres was used in front of the detector's collimating aperture to ensure that any particle colliding in the scattering rod was scattered toward the detector.

4.1.1.3 Detector response function calculation

The detector's response to monoenergetic photons was determined using a full model of the CS spectrometry system for each scattering angle, θ. The MCNP `pstudy` script was used to create a series of input files that were run separately, each with a different monoenergetic source energy, E_s, that was related to the centroid energy of an MCA channel, E_{ch}, by

$$E_s = \frac{E_{ch}}{1 - \frac{E_{ch}}{0.511}\left(1 - \cos\theta\right)}, \tag{4.1}$$

where E_s and E_{ch} are given in MeV. Thus, each source energy was defined as the energy that would scatter into a specific channel, assuming scattering from free electrons. In addition, the Gaussian energy broadening (GEB) tally-modifier option was used to model the detector's finite energy resolution. The magnitude of this broadening was determined from full-width-at-half-maxima (FWHM) measurements of the energy calibration peaks.

For each monoenergetic simulation, the energy deposited in the active volume of the germanium detector was scored using the F8 pulse-height tally with energy bins matching the energy calibration of the system. The results of the individual detector response simulations were then compiled into square matrices where the columns represented source energy and the rows represented detected energy.

4.1.2 System model verification

Each measurement in this work was corrected using an MC-generated DRF, the accuracy of which depended on the source and detector models that were used. The MC model of the detector and CS system was verified by comparing simulated and measured pulse-height distributions (PHDs) for the Theratronics T1000 ^{60}Co teletherapy unit (see Chapter 6 for details on this irradiator).

Each simulated PHD included a full model of the T1000 ^{60}Co unit for a (10 x 10) cm^2 field. In addition, the scattering rod and CS geometry were accurately modeled. The simulated PHD was determined using an energy-binned F8 pulse-height tally in the volume of the detector crystal. Each simulation used the appropriate energy binning and GEB parameters to allow for a direct comparison between simulated and measured PHDs.

4.1.2.1 Detector model

As discussed in Section 4.1.1.1, the REGe detector model was modified from a model of the same detector that Beach created (2005). The changes to the model included the addition of a signal contact pin and preamplifier. The effect of these additional components on the simulated PHD was investigated for a ^{60}Co spectrum that was scattered at 31.3° from an aluminum rod. PHD simulations were performed using the two detector models. With the exception of the detector, the simulation geometries were identical. Figure 4.4 shows the results of these simulations, with the measured PHD shown for comparison. All PHDs were normalized to the value for the scattered 1.33 MeV photon peak.

The positions and magnitudes of the scattered ^{60}Co peaks agreed for the measured and two simulated PHDs; however, there was disagreement in the lower-energy region. The PHD determined using Beach's detector model included significantly fewer photons below the scattered peaks than did the other simulated or measured PHDs. In addition, the shape and magnitude of this region for the updated detector model's PHD and the measurement generally agreed. This indicates that, not only did the posterior detector components substantially affect the PHD, but they were appropriately represented in the modified detector model.

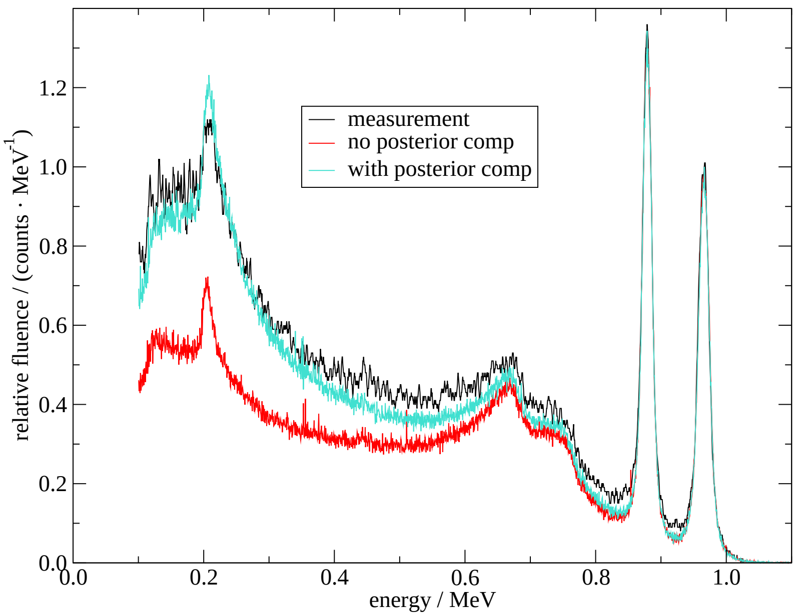

Figure 4.4: Simulated PHDs for the T1000 ^{60}Co spectrum using two different MC models of the REGe detector. The measured PHD is shown for comparison. The PHDs represent scattering at 31.3° from an aluminum rod.

4.1.2.2 DB model

Section 3.2 presented an investigation on the implementation of Doppler broadening (DB) in MCNP5. The conclusions of that investigation were drawn from comparisons of simulations to analytical data. The present section investigates the effect of DB on PHDs by comparing simulations to measured data for the scattered ^{60}Co spectrum. The simulations included a full model of the T1000 system and the shielded REGe detector. PHDs were calculated for scattering at 31.3° from an aluminum scattering rod using versions 1.51 and 1.60m of MCNP5. Both simulations were run with the MCPLIB04 photon data library. The results of these simulations are shown in Figure 4.5, with the measured PHD shown for comparison. This figure features only the scattered ^{60}Co emissions with each PHD normalized at the position of the scattered 1.33 MeV photon peak.

According to the findings presented in Section 3.2, v1.51 did not model DB above incident photon energies of 0.367 MeV for scattering at 31.3° (see Figure 3.5 for the threshold

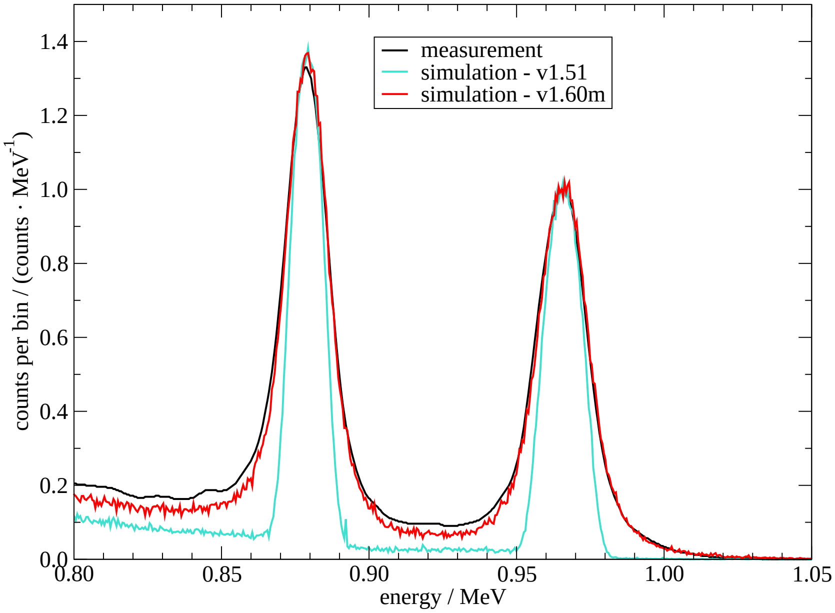

Figure 4.5: Simulated and measured PHDs for the T1000 spectrum that has been scattered at 31.3° by an aluminum rod. These simulated data were generated with MCNP5 v1.51 and v1.60m using the MCPLIB04 photon data library.

above which DB was not modeled). Thus, v1.51 did not model DB for the ^{60}Co emissions in this particular measurement geometry. This is evident from the shapes of the peaks in Figure 4.5, which were sharper than the measured peaks and had no low- or high-energy tails. The peaks that were calculated with v1.60m showed excellent agreement with the measurement in both magnitude and shape.

4.1.2.3 Simulated pulse-height distributions

Sections 4.1.2.1 and 4.1.2.2 presented verifications of the REGe detector model and incoherent scattering model in MCNP5. These verifications were performed by comparing simulated and measured PHDs for the T1000 ^{60}Co spectrum that was scattered at 31.3° using an aluminum scattering rod. To demonstrate that these characterizations are valid for all measurement geometries, simulated PHDs were calculated for the other three T1000 CS geometries that were investigated in this work. Each simulation modeled the same conditions (i.e., scattering angle, scatterer-to-detector distance) as its analogous ^{60}Co spectrum measurement, which are discussed in detail in Section 6.3.

The simulated PHDs for each of the CS geometries are shown in Figure 4.6, with the measured PHDs shown for comparison. Each PHD is normalized at the energy of the scattered 1.33 MeV peak. These results indicate that the MC models and simulation methods used are applicable to all CS geometries for the T1000 unit. Following this initial characterization, this methodolog6y was validated for use with other sources and geometries.

4.1.3 Source and spectra simulations

A complete model of each megavoltage source was created in MCNP5. These models were verified by comparing simulated data to measured data for cross-beam profiles and percentage depth-dose curves. The details of the models, along with the techniques used to verify their accuracy, can be found in Chapters 6 and 7 for the ^{60}Co and linac sources, respectively.

Spectra for both sources were determined for a variety of physical source parameters using two MCNP5 tallies. The F4 cell-based fluence tally was used to score the spectrum at 100 cm from the source in concentric cylindrical rings. This tally gives the average fluence in a cell based on a track-length estimator. Spectra were also calculated using the F5 point detector tally, which gives a deterministic estimate of the fluence at a point. Contributions to this tally come directly from the source and from each collision throughout the calculation.

4.2 Measurement methods using the Compton spectrometer

Measurements in this work were performed using a CS spectrometry technique. The following section describes the measurement system, procedure, and corrections that were used for the measurement of two megavoltage photon sources.

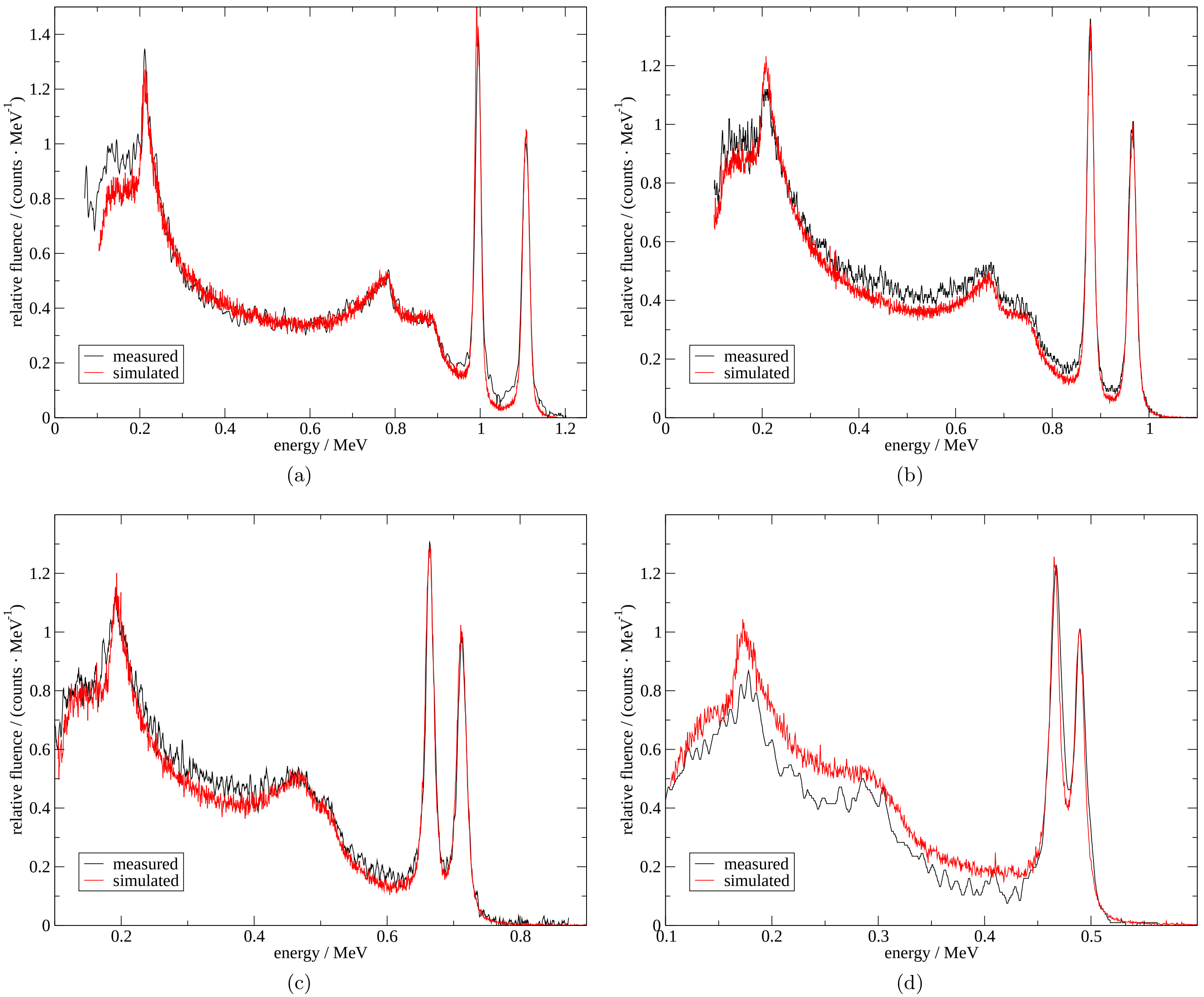

Figure 4.6: Simulated PHDs for CS experiments with the T1000 ^{60}Co source that were performed at scattering angles of (a) 22.8°, (b) 31.3°, (c) 48.1°, and (d) 70.1°. The measured PHDs are shown for comparison.

4.2.1 Spectrometry system

4.2.1.1 System electronics

The REGe detector (Model GR2519) from CANBERRA was used for the measurements performed in this work. This closed-ended coaxial detector is so-named because its electrodes are in the opposite configuration from conventional coaxial detectors. Namely, the *p*-type electrode (ion-implanted boron) is on the outside of the detector, and the *n*-type (diffused lithium) is on the inside. With this configuration of electrodes, the detector is less susceptible to radiation damage than in the opposite configuration. This detector was selected due its energy resolution (nominally 1.9 keV FWHM for 1332 keV photons) and extended dynamic range (up to 10 MeV). It had a 0.5 mm-thick beryllium window, allowing for the detection of photons down to 5 keV (CANBERRA Industries). The system was cooled with liquid nitrogen using a horizontal dipstick cryostat and a 30 L liquid nitrogen dewar.

The system was biased to -4500 V using a high voltage power supply (CANBERRA, Model 3106D). The germanium crystal was connected to a series of nuclear instrumentation module (NIM) components that provided signal processing prior to analysis with the Genie$^{\text{TM}}$ 2000 Gamma Analysis Software package from CANBERRA, Inc. The NIM components in the detector chain were: a transistor-reset preamplifier (CANBERRA, Model 2101NSL), a fast-spectroscopy linear amplifier with pile-up rejection (CANBERRA, Model 2024), and a multichannel analyzer (CANBERRA, Multiport II). The unipolar amplifier output was used for all measurements. A photograph of the NIM electronics modules is given in Figure 4.7.

4.2.1.2 Shielding and collimation

Substantial shielding was required to reduce background contributions that came from head leakage and room scatter. This was accomplished with a custom-made cylindrical shield

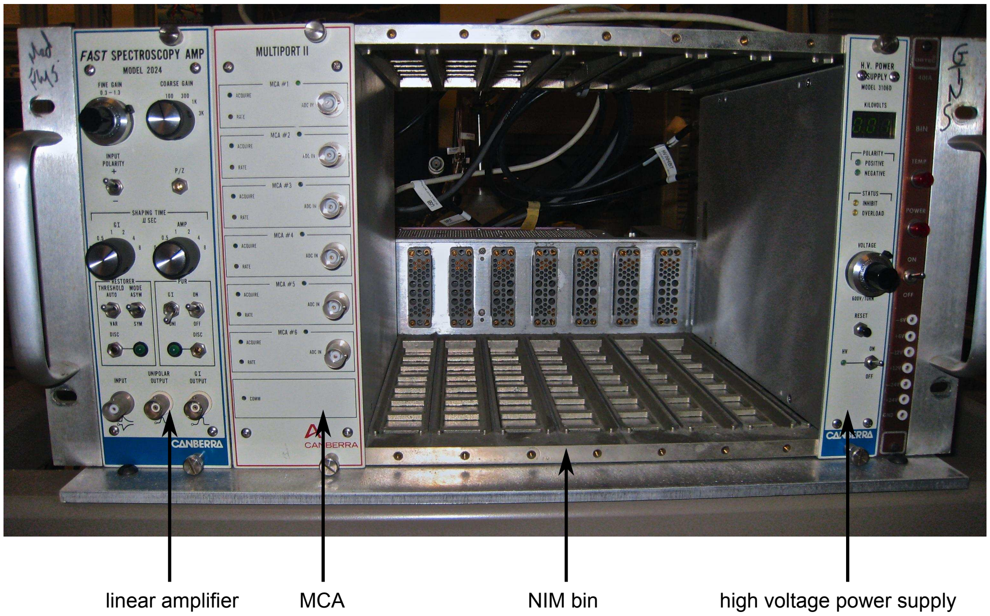

Figure 4.7: Photograph of the NIM electronics used for spectra measurements.

that was designed in collaboration with Hopewell Designs, Inc. (Alpharetta, GA). The shield provided a minimum of 10 cm of lead around the detector, with 30 cm of lead in front. A cavity in the shield allowed for the insertion of the detector. This cavity was lined with a 0.032 in-thick (0.081 cm) layer of tin followed by a 0.06 in-thick (0.152 cm) layer of copper. Graded liners such as this are often used in low-level counting systems (Gilmore, 2008) to reduce the amount of fluorescence originating in the shield and reaching the detector. In this graded liner, the tin layer absorbed the lead fluorescent x rays ([72 to 82] keV) and the copper absorbed the tin fluorescent x rays ([25 to 29] keV).

The collimating aperture was defined by an insert that fit into the front end of the shield. The insert was composed of lead cast around a piece of tungsten. A 2 mm-diameter aperture, which was precisely cut using electrical discharge machining, ran through the tungsten. The insert had an aluminum face with a grid pattern of holes to allow for various devices to be attached to the front of the system. Figure 4.8 shows the collimator insert and its aluminum face.

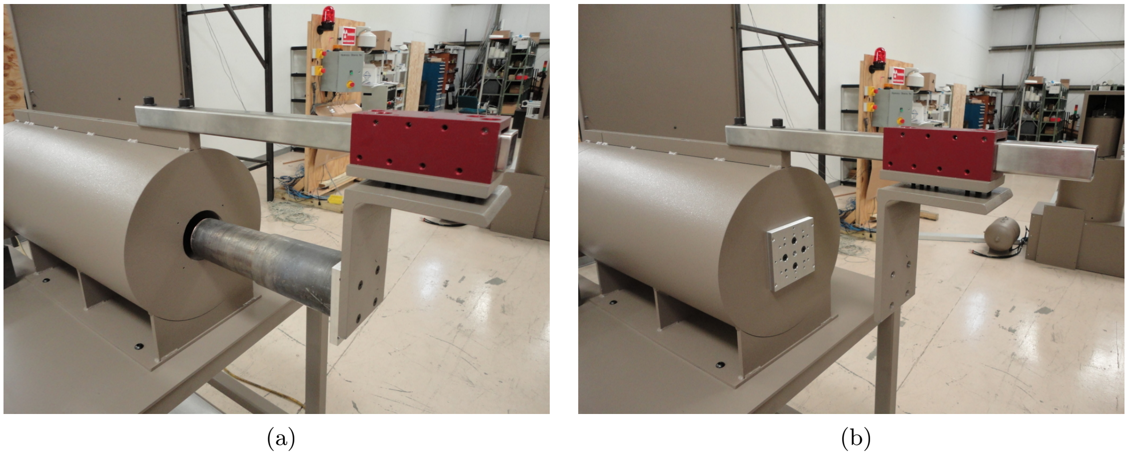
(a) (b)

Figure 4.8: (a) Removable lead and tungsten collimating aperture and (b) its aluminum face with a grid pattern for attachments. The rectangular extrusion was used for inserting and removing the collimator. It was removed for measurements.

The detector and cryostat were positioned inside the shield. A cutout in the back of the shield allowed the dipstick to pass from the detector into the liquid nitrogen dewar, which remained unshielded. A lead collar was placed around this portion of the dipstick to limit the room scatter entering the detector region. The lead shield, dewar, and electronics were placed on a mobile cart that allowed for vertical adjustment of the detector within ±6 cm of 130 cm. The height of the apparatus was changed using bottle jacks placed at each end of the cart, and was secured with lifting nuts on threaded rods. Figure 4.9 shows the shield with the detector inside.

As seen in Figure 4.9, the entire liquid nitrogen dewar was positioned below the cart's tabletop. Due to this arrangement, the detector had to be raised approximately 4 in from its nominal position so it could slide into the shield. With the detector in this raised position, a 4 in-long aluminum cold finger extension (CFE) from CANBERRA was attached to the dipstick so it extended to the bottom of the dewar (see Figure 4.10). A coiled indium wire between the CFE and dipstick provided the thermal connection.

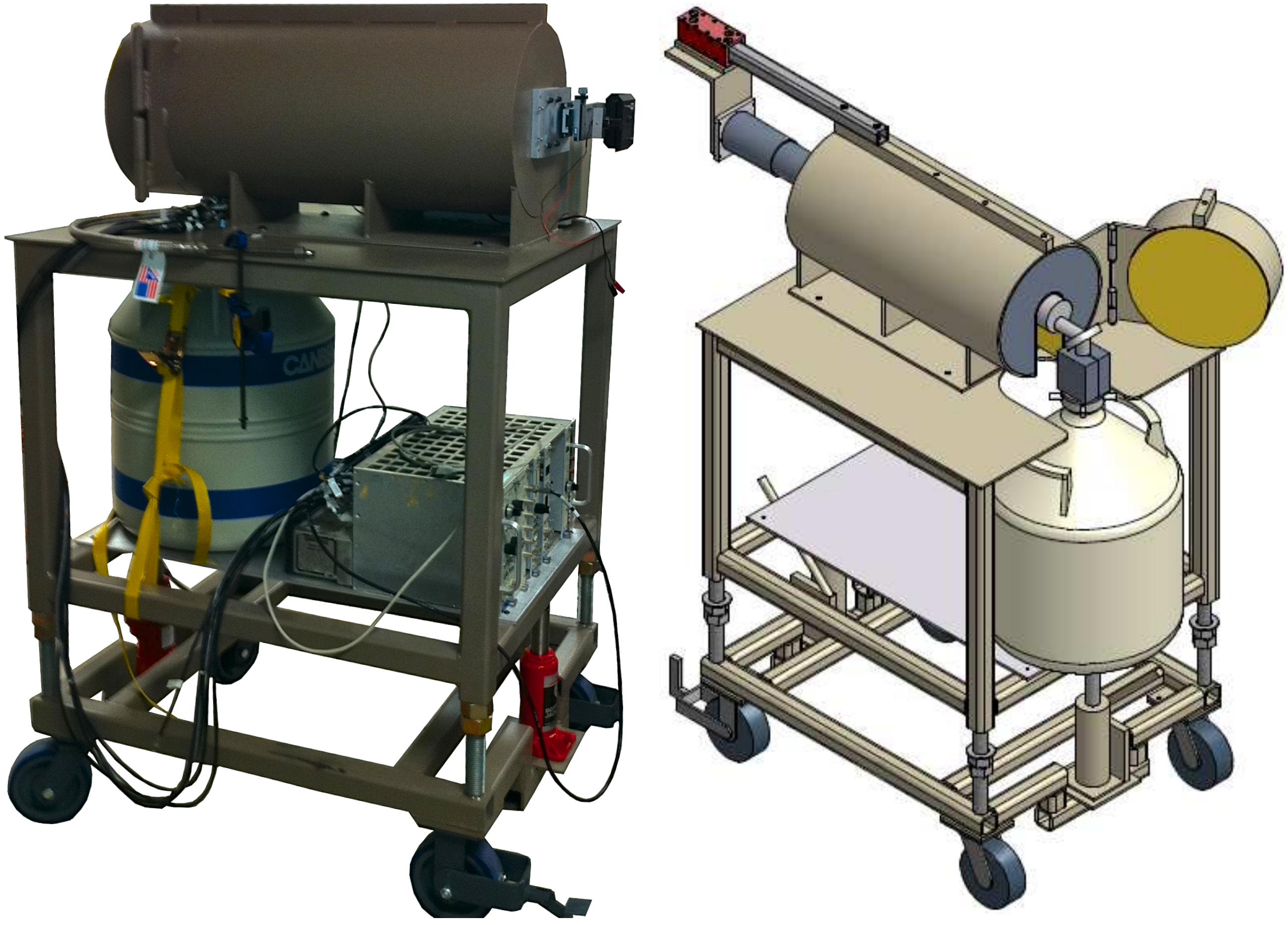

(a) (b)

Figure 4.9: (a) Photograph and (b) schematic of the custom-designed shield and collimating aperture with detector inserted.

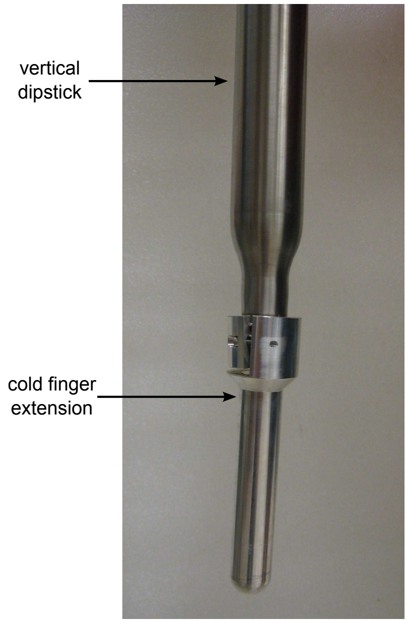

Figure 4.10: Four inch-long cold finger extension that was attached to the dipstick.

4.2.2 Measurement setup and procedure

4.2.2.1 Energy calibration

For each measurement, an energy calibration measurement was performed using a Type D multinuclide standard source (Isotope Products, Inc., Valencia, CA) that was NIST-traceable for energy. This source provided calibrated lines up to 1836 keV. Due to the low activity of the source (13.36 μCi on May 1, 2008), the 2 mm collimator insert had to be removed from the lead shield to achieve reasonable count rates. The multinuclide source was positioned in the center of the 3.75 in-diameter (9.525 cm) opening at the front of the shield.

The collection time for each measurement was 12 hours. Following measurement acquisition, the Genie$^{\text{TM}}$ 2000 software was used to identify the seven most prominent peaks in the collected spectra (see Table 4.1). The channel-to-energy calibration for the system was then determined using a linear fit generated by the Genie$^{\text{TM}}$ 2000 program.

Table 4.1: Peaks from the multinuclide source that were used for energy calibration.

Isotope	Emission energy (keV)	FWHM (keV)
^{210}Pb	46.54	1.774
^{241}Am	59.54	1.831
^{109}Cd	88.04	1.994
^{57}Co	122.06	1.717
^{137}Cs	661.66	3.778
^{60}Co	1173.24	5.813
^{60}Co	1332.50	6.080

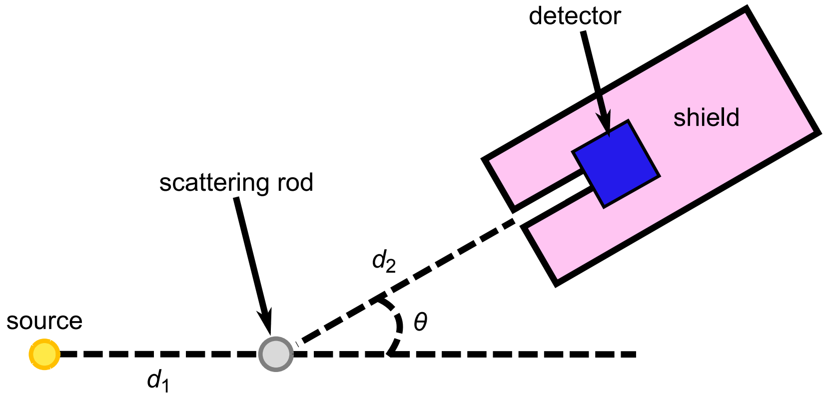

Figure 4.11: Top view diagram of a general CS spectrometry measurement setup.

4.2.2.2 CS measurements

Measurement setup CS spectrometry measurements were performed for two megavoltage sources, a ^{60}Co teletherapy unit and a linear accelerator. These measurements were performed using an aluminum scattering rod and the shielded REGe detector. Figure 4.11 shows a schematic of the general measurement system that was used for these measurements. The specific arrangements of components (i.e., d_1, d_2, and θ) were different for each measurement and are discussed in detail in Sections 6.3 and 7.3.

For all measurements, the scattering rod was positioned at the intersection of the collimating-aperture axis and central axis of the field. The scattering rod was aligned on the central axis using in-room lasers in the ^{60}Co and linac vaults. The lasers in these vaults intersected at the radiation isocenter for each unit. The detector was then precisely aligned with the scattering rod using a positioning laser that was attached to the aluminum plate on the front of the detector's shield. The scattering angle, θ, was defined as the angle between the in-room lasers and this removable laser.

Positioning-laser alignment The positioning laser was used to precisely align the collimating aperture to the scattering rod. The accuracy of this technique required the coincidence of the laser and the collimating aperture; thus, prior to any measurements, bore-sight adjustments were performed to align these two axes. Two lasers were used for the bore-sighting adjustments: the positioning laser and a reference laser. Positioning devices were constructed to hold each of these lasers and to allow translational and rotational movement. Each positioning device consisted of two lead-screw drives and a mirror mount, all from Edmund Optics (Barrington, NJ). Aluminum laser holders were machined and attached to each mirror mount. Figure 4.12a shows one of the positioning devices with a laser in place.

The apparatus that held the reference laser was positioned at the back of the lead shield. The optics devices on this apparatus were adjusted until the reference laser's crosshair projected through the 30 cm-long collimator. The position of the crosshair was marked on a piece of graph paper that was approximately 20 cm in front of the shield. The positioning laser was then attached to the aluminum face on the collimator (see Figure 4.12b). The projection of the positioning laser's crosshair was adjusted until it matched that of the reference laser. This procedure was repeated at several different distances, resulting in the coincidence of the collimating aperture and positioning laser within 0.1°. Following this alignment, the position of the front laser was locked using set screws on all of the optics devices.

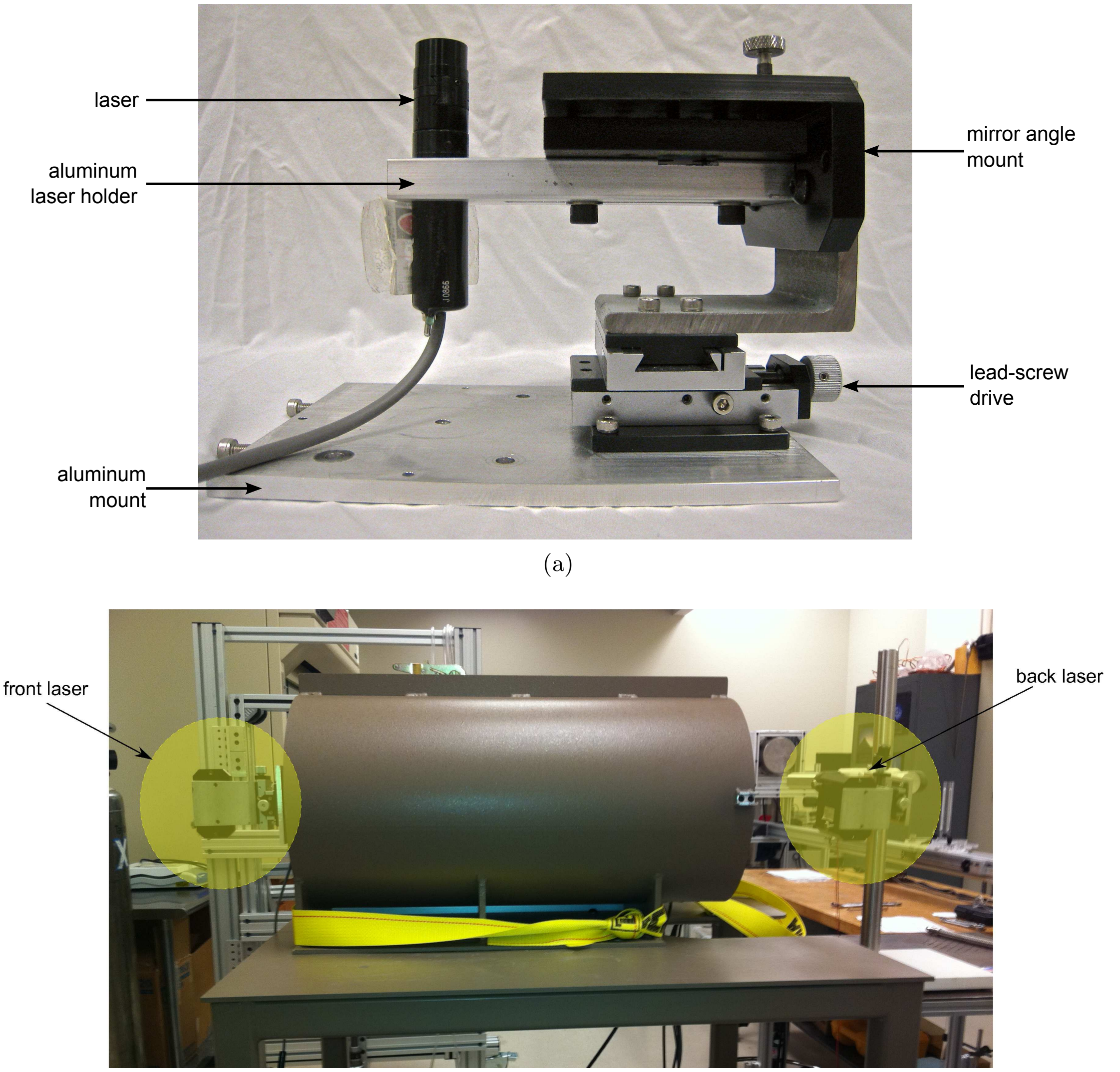

(a)

(b)

Figure 4.12: (a) Photograph of a laser positioning device and (b) arrangement of the positioning and reference lasers for the bore-sight adjustments.

4.2.2.3 Background measurements

In spectrometry, background photons are defined as measured photons that come from an unintended source. For CS spectrometry, the source of interest is the set of singly scattered photons from the scattering rod that travel through the collimating aperture of the shield (Matscheko and Carlsson, 1989). Thus, background for these measurements is attributed to environmental radiation, multiply scattered photons, room-scattered photons, and transmission photons.

In this work, a background measurement was performed for each CS measurement configuration. For the background measurements, the collimating aperture was plugged with 16 cm of tungsten and blocked externally with lead. All other aspects of the system were unchanged (e.g., primary source, scattering rod). This additional shielding attenuated all CS photons from the scattering rod without appreciably changing the rest of the system. Background was removed from each spectrum measurement using channel-by-channel subtraction. In cases where the acquisition times for the CS measurement and background measurement were different, each channel of the background PHD was scaled by a ratio of the acquisition times.

4.2.3 Measured spectra unfolding

After correcting for background, each spectrum was unfolded from its measured PHD using the iterative Gold deconvolution technique, which was discussed in detail in Section 2.1.3.1. This method was selected because its solutions are always real and positive. The Gold deconvolution was implemented using a script that was written in the Octave programming language. For each spectrum, a minimum of 10,000 iterations were performed.

Unfolding methods are used to correct for artifacts that are accounted for in the detector response function. Conventionally, the detector response accounts for interactions in the detector and the peak broadening that occurs due to detector resolution. In this

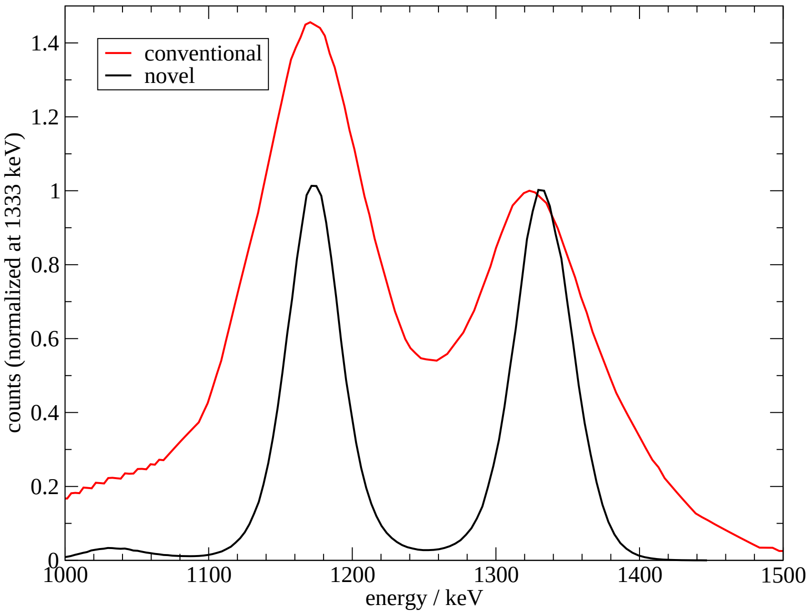

Figure 4.13: Spectra that have been unfolded from a measured PHD of the T1000 ^{60}Co system for scattering at 70.1°. Unfolding was performed using Gold deconvolution with a conventional (red) and detailed (black) detector response function.

work, a more detailed detector response was used to also account for the CS relations and interactions in the shield, as was discussed in Section 4.1.1.

The effect of the detail in the detector response function was demonstrated by unfolding the spectrum from a measurement of the T1000 ^{60}Co unit for scattering at 70.1° from an aluminum rod. The spectrum was unfolded using both a detailed and conventional detector response function. The detailed detector response was determined using the methods described in Section 4.1.1. The conventional detector response was determined using similar methods, but did not account for the CS geometry, which was manually corrected for after applying the Gold deconvolution. Figure 4.13 shows the spectra, featuring only the ^{60}Co peaks, that were unfolded using the conventional and detailed detector response functions. According to this figure, the two ^{60}Co peaks are not resolvable from one another in the spectrum that was unfolded using the conventional detector response; however, with a sufficient number of iterations, the Gold deconvolution returns fully resolved ^{60}Co peaks when the detailed detector response is used.

Chapter 5

Verification of CS spectrometry technique

Prior to characterizing the megavoltage sources in this work, the Compton-scattering (CS) spectrometry technique was demonstrated using both Monte Carlo (MC) and measurement methods. The MC simulations were performed for a 6 MV linear accelerator field with the purpose of verifying that the proposed measurement system was capable of measuring the CS spectrum above background. The measurement demonstration was performed for a high dose rate ^{192}Ir brachytherapy source with the purpose of verifying that the CS spectrometry system worked in practice for a relatively high fluence rate source with well-known peak energies.

5.1 Monte Carlo methods

The expected performance of the CS spectrometry system for the measurement of a 6 MV linear accelerator field was assessed by performing MC simulations. The purpose of these simulations was to demonstrate that the magnitude of the measured pulse-height distribution (PHD) from CS photons was larger than the unintended background PHD from room scatter and leakage. The system's expected performance was evaluated based on the relative magnitudes of the spectra at the detector from both primary and secondary sources. The details of the MC simulation methods are discussed in the following sections.

5.1.1 General simulation geometry

The CS spectrometry system, including the source, scattering rod, and shielded spectrometer, was modeled in the Monte Carlo N-Particle (MCNP5) code to simulate the measurement of a 6 MV linear accelerator field. The system was modeled inside of a generic (25 x 25 x 14) ft^3 treatment vault with 6 ft-thick walls of Portland concrete (Berger et al., 2005a). The treatment vault was modeled because it was expected to impact background measurements.

The primary photon source for these simulations was a point source that was mathematically collimated to produce a field with a circular cross-sectional area (radius, $r = 5.64\,\mathrm{cm}$) equivalent to a (10 x 10) cm^2 square field at 100 cm from the source. The source was directed at a wall that was about 500 cm away. The 6 MV photon spectrum for a generic Varian linear accelerator (Sheikh-Bagheri and Rogers, 2002) was used for the primary source. An aluminum scattering rod (2 mm in diameter, 4 cm in length) was placed 100 cm from the source on the central axis of the beam. The scattering rod was oriented such that its cylindrical axis was perpendicular to the floor. The modified REGe detector model, which was discussed in detail in Section 4.1.1.1, was used for these simulations. The detector and shield were modeled at 30° relative to the central axis of the source, with the scattering rod centered in front of the collimating aperture. The scatterer-to-detector distance was 300 cm. Figure 5.1 shows the general geometry that was used for these simulations.

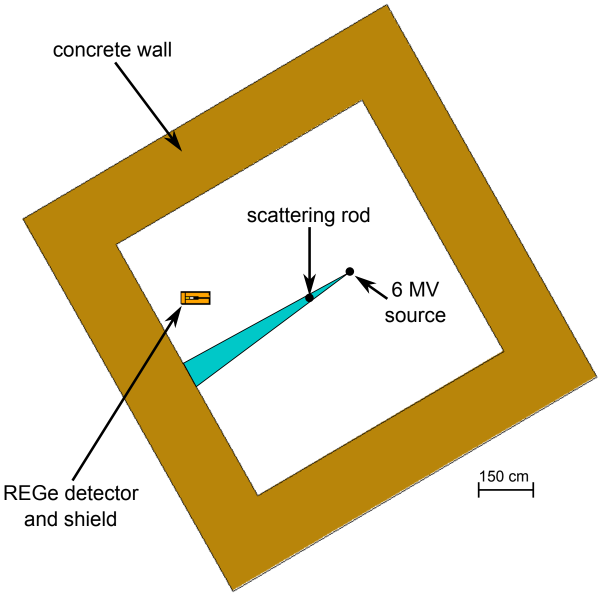

Figure 5.1: Visual Editor (VisEd) rendering of the geometry used for the demonstration of the CS technique. Note that the sizes of the source and scattering rod have been increased for visibility. The blue triangular region illustrates the projection of the mathematically collimated source.

5.1.2 Variance reduction

The purpose of these simulations was to determine the relative magnitudes of the spectra that would be incident on the detector from both primary and secondary sources. The specific sources that were considered were (1) the CS photons from the scattering rod that passed through the collimating aperture (i.e., the intended signal), (2) the background CS photons from the scattering rod that penetrated the detector shield, (3) the background room-scattered photons that penetrated the detector shield, and (4) the background leakage photons that penetrated the detector shield. Due to the small size of the scattering rod, the narrow collimating aperture, and the thickness of the lead shield, photons from each of these sources were unlikely to reach the detector in an analog simulation. In order to achieve reasonable statistics, these analog simulations would require a prohibitive number of particle histories to be run. To mitigate these problems, multiple variance reduction techniques were used in this work, including forced collisions, the DXTRAN technique, and weight windows.

The forced-collision technique, which was discussed in Section 4.1.1.2, was used to increase the number of photons that interacted in the scattering rod. The DXTRAN technique, which was discussed in Section 3.1.2, was used to bias the direction of the photons from the scattering rod towards the detector. Finally, the weight window technique, which will be discussed presently, was used to increase the likelihood of particles to penetrate the detector shield.

Weight windows (WWs) are used to preferentially track particles that are likely to contribute to a tally, but may not do so in an analog simulation. With this technique, a range of acceptable particle weights is specified at each position in phase space (i.e., position and energy) using an upper and lower weight bound that defines a window. When particles enter a given region in phase space, their weights are compared against the corresponding WW. For particles with weights that are below the window, a Russian roulette (RR) game is played in which particles survive with a specified probability. The weights of the particles that survive the RR game are then increased to be within the window. Particles with weights that are above the window are split into multiple particles, each with a weight that is within the window.

For complicated problems, the appropriate choices for weight bound values are often non-intuitive. In these situations, MCNP5's weight window generator (WWG), which semi-automatically determines appropriate WWs, is particularly useful. This generator may be used to create spatial windows (i.e., a single WW for a given spatial region) or space-energy windows (i.e., multiple WWs for a given spatial region, each of which applies to a particular energy range). The spatial regions may be defined by cells or by a user-specified mesh that is overlaid on the geometry. In this work, spatial WWs were defined in the detector's lead shield using the WWG. A cylindrical mesh was overlaid on the geometry to divide the shield

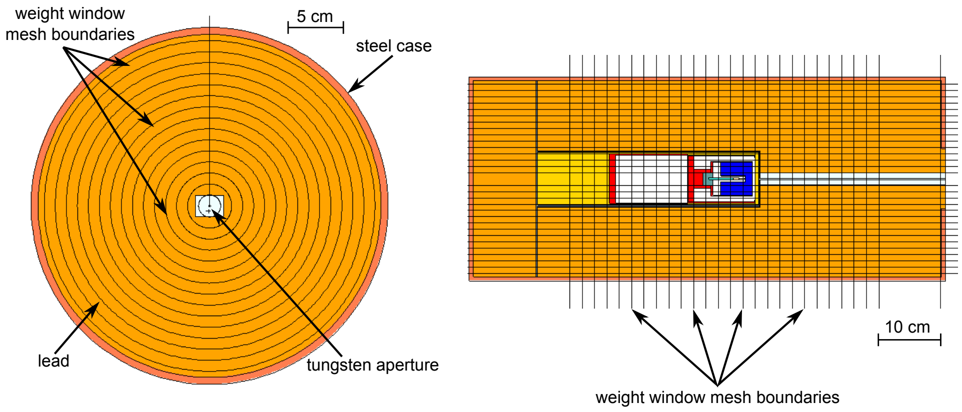

(a) (b)

Figure 5.2: VisEd rendering of the cylindrical mesh for cross sections of the detector in directions that were (a) perpendicular to and (b) parallel to the collimating aperture. The mesh was used to define position-dependent WWs for shielding simulations.

into shells that were segmented along the axis of the shield (see Figure 5.2). A WW was specified within each voxel of the mesh, allowing MCNP5 to preferentially follow particles that were likely to reach the detector region.

The WWG optimizes WW boundaries to minimize the variance of a specific tally. In order for the WWG to create nonzero weight boundaries, particles must contribute to the tally that is being optimized upon; however, for thick shielding problems, it is uncommon for particles to reach the desired tally region. In these problems, the WWG will not work unless intermediate steps are taken to ensure particles contribute to the tally. For each set of weight windows in this work, a series of simulations was run in which the lead and tungsten in the shield were modeled with lower than nominal densities (nominal density, $\rho_{\mathrm{Pb}} = 11.34\,\mathrm{g\cdot cm^{-3}}$, $\rho_{\mathrm{W}} = 19.3\,\mathrm{g\cdot cm^{-3}}$). In the first simulation of this series, the lead and tungsten were modeled with densities of $0.5\,\mathrm{g\cdot cm^{-3}}$. With these parameters, photons easily reached the detector region, and initial WWs were created. In each subsequent simulation, the densities of the shield components were increased, and a new set of WWs was generated from the old set. Progressing iteratively in this way, WWs were optimized to minimize the variance of the tally at the detector for the full-density shield.

5.1.3 Relative detector contribution simulations

Four simulations were run to determine the relative PHDs for each of the sources that were investigated. Each of these simulations used a selection of the methods described in Sections 5.1.1 and 5.1.2. For each simulation, an energy-binned F8 pulse-height tally was used in the detector volume to score the PHD. The integral F8 tally in the detector was also used to score the total number of expected pulses. The following sections discuss the details of each of these simulations.

5.1.3.1 CS photons through detector aperture

The expected PHD from the CS photons that traveled through the collimating aperture (i.e., the intended signal) was determined using a simulation method similar to that which was used for the simulated PHDs in Section 4.1.2.3. This simulation used the forced-collision variance reduction technique in the scattering rod. A 0.3 cm-diameter DXTRAN sphere was positioned directly in front of the collimating aperture to bias the direction of the photons that interacted in the scattering rod.

5.1.3.2 CS photons through detector shield

The expected PHD from the CS photons that penetrated the shield was determined using the forced-collision, DXTRAN, and WW variance reduction techniques. Collisions were forced in the scattering rod, and the direction of the CS photons was biased using the DXTRAN technique. The DXTRAN sphere for this simulation was centered approximately 15 cm in front of the shield and had a diameter of 24 cm. With this geometry, the DXTRAN sphere biased scattered photons towards the entire shield rather than towards just the collimating aperture. For this simulation, the collimating aperture was plugged with tungsten, and WWs were used in the detector shield.

5.1.3.3 Room-scattered photons through detector shield

The largest expected contribution to the room-scattered background PHD came from the wall that was directly in front of the source and exposed by the primary beam. To determine the expected PHD from this source, a 30 cm-diameter DXTRAN sphere was placed between the wall and the side of the lead shield. This DXTRAN sphere biased the direction of wall-scattered photons towards the detector. No scattering rod was used for these simulations, and the collimating aperture was plugged with tungsten. The WW technique was used in the detector shield for this simulation, as well.

5.1.3.4 Leakage photons through detector shield

To determine the PHD due to linac leakage, a simulation was run in which the 6 MV spectrum shined directly on the shield from the primary source location. For this simulation, a 20 cm-thick lead wall was placed between the source and shield (see Figure 5.3). This was done because extra shielding was expected to be necessary to attenuate linac leakage. A thickness of 20 cm was selected using an iterative process. Only the WW variance reduction technique was used.

This simulation used different mathematical collimation than was discussed in Section 5.1.1, where the source was directed towards the scattering rod rather than towards the shield. Because of this difference, these leakage results had to be normalized for comparison with the other simulations. Two steps were used in this normalization process. First, because all MCNP5 tally results are normalized per starting particle, it was necessary to define the relationship between starting particles in the leakage simulation and starting particles in the other simulations. This was done by assuming that the 6 MV source was isotropic. For an isotropic source, the fluence in vacuum at a specific distance from the source is constant, regardless of direction. Thus, a scaling factor was determined so that the normalized fluence at 100 cm from the leakage source was the same as that for the primary source. The

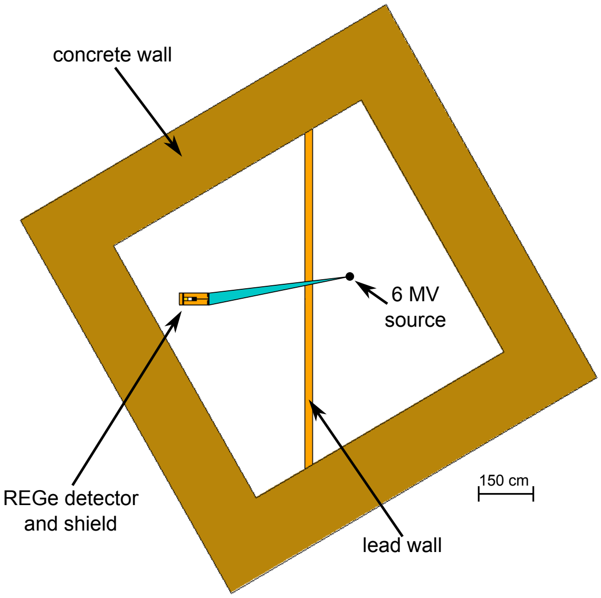

Figure 5.3: VisEd rendering of the geometry used for the simulation of the leakage PHD. This geometry included an additional 20 cm-thick lead wall between the source and detector. Note that the size of the source has been increased for visibility. The blue triangular region illustrates the projection of the mathematically collimated leakage source.

scaling factor was found by taking a ratio of the primary and leakage source fluences, which were simulated using an F5 point detector tally in vacuum. This initial scaling described the leakage for an isotropic source; however, it is known that linear accelerator sources are not isotropic. To a first order approximation, leakage can be assumed to constitute approximately 0.1 % of the primary beam fluence (NCRP Report 151, 2005). Thus, the second normalization step involved dividing the scaled leakage PHD and total number of pulses by a factor of 1000.

5.1.4 Results

The expected PHDs for each of the sources that were investigated are shown in Figure 5.4. The PHD for the CS photons that traveled through the collimating aperture (Figure 5.4a) featured peaks near 250 keV and 511 keV. The 250 keV peak resulted from backscattered

Table 5.1: Expected total number of pulses in the detector for each of the sources that were investigated. The results have been normalized per starting particle.

Source of tally contribution	F8 tally $\left(\frac{\text{pulses}}{\text{starting particle}}\right)$
CS photons through aperture	5.99560×10^{-11}
CS photons through shield	7.07911×10^{-15}
Wall-scattered photons	1.66992×10^{-15}
Leakage photons	1.80187×10^{-15}

photons from the posterior components in the detector, and the 511 keV peak resulted from annihilation photons in the detector and shielding. These peaks sat on a continuous distribution of pulses with a maximum energy that was slightly above 2 MeV. The PHD for the CS photons that penetrated the shield (Figure 5.4b) showed similar peaks and maximum-energy pulses; however, this PHD exhibited more higher-energy pulses relative to the 250 keV peak. The PHD for the wall-scattered photons (Figure 5.4c) showed a relatively flat distribution of pulses and a 511 keV annihilation photon peak. Finally, the PHD for the leakage source (Figure 5.4d) showed a pronounced 511 keV peak and a continuous high-energy tail with a maximum energy near 4.5 MeV.

According to Figure 5.4, the PHD from the CS photons that traveled through the collimating aperture was orders of magnitude larger than the PHDs from the other sources. This was confirmed by the total number of expected pulses for each source (see Table 5.1), in which the signal through the collimating aperture was about four orders of magnitude larger than any background component. These MC results indicate that the CS spectrometry technique is viable for the measurement of a 6 MV photon spectrum.

5.2 Measurement methods

The focus of this thesis work was on megavoltage photon sources; however, as a demonstration of the CS spectrometry technique, spectra measurements of the Varian VariSource$^{\text{TM}}$

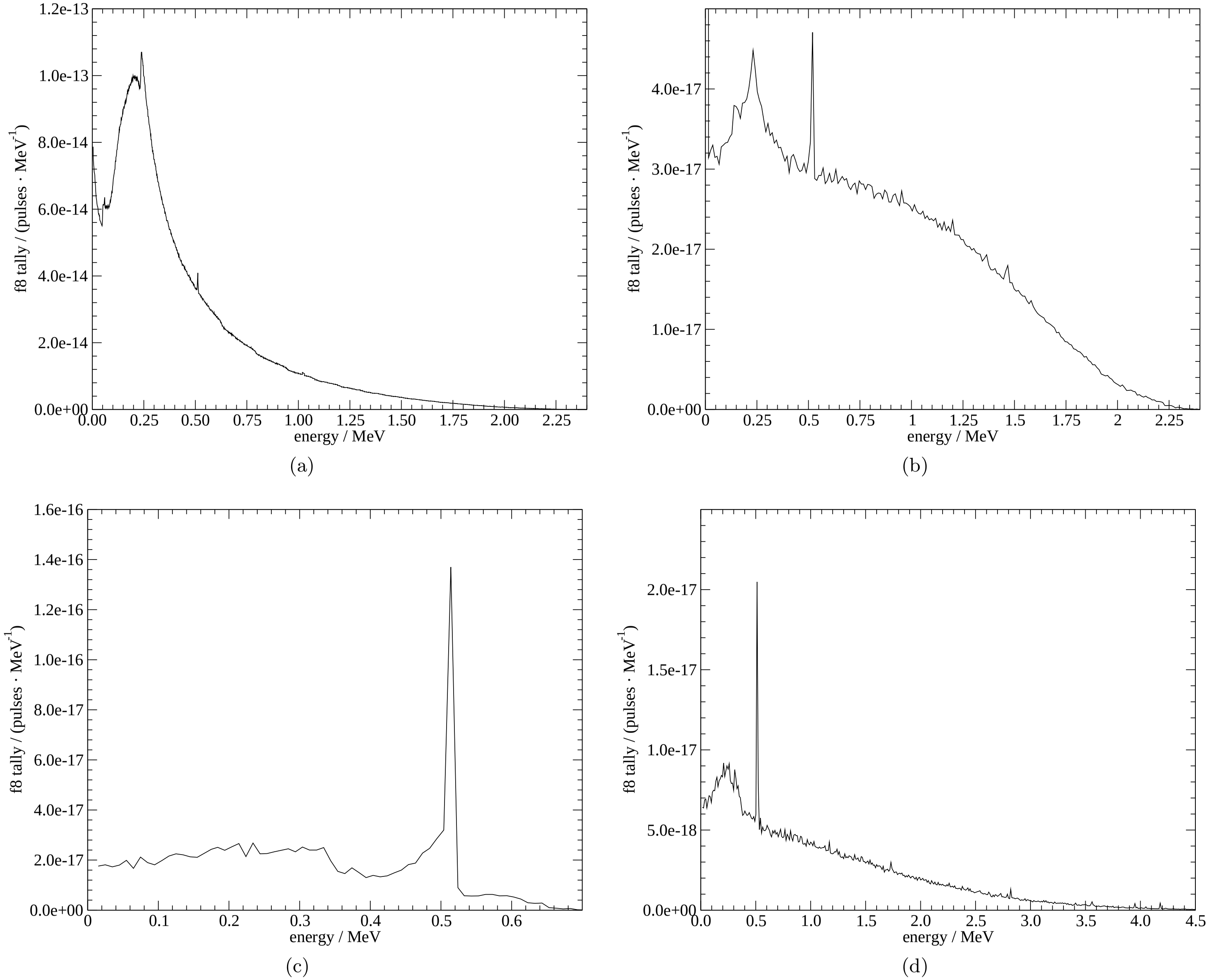

Figure 5.4: Simulated PHDs for (a) CS photons that traveled through the collimating aperture, (b) CS photons that penetrated the detector shield, (c) wall-scattered photons that penetrated the detector shield, and (d) leakage photons that penetrated the detector shield. The results have been normalized per starting particle. Note that the ordinate-axis scale is different for each subfigure.

(VS2000) high dose rate ^{192}Ir source at the University of Wisconsin Accredited Dosimetry Calibration Laboratory were completed. This section discusses the details of the system and the spectroscopic characterization that was performed using the CS spectrometry technique.

5.2.1 VS2000 source description

The VS2000 ^{192}Ir source was chosen to perform an initial demonstration of the CS spectrometry measurement technique. These preliminary measurements were performed prior to designing and commissioning the custom lead shield that was discussed in Section 4.2.1.2. This source was selected because it had a mean energy of about 400 keV, so the REGe detector did not require substantial shielding to reduce the background signal. In addition, the source activity was high enough that primary beam measurements were not possible, and the CS spectrometry technique was mandatory.

5.2.2 Spectrometry system

The REGe detector and NIM electronics modules that were discussed in Section 4.2.1.1 were used in the measurement of the VS2000 spectrum; however, different shielding and collimation were used for these measurements. The detector and dewar were positioned on a mobile spectrometry cart that was constructed by Moga (2011). This system was constructed of aluminum extrusion framing and allowed for variable vertical detector positioning.

The detector was placed inside of a cylindrical low-background shield from CANBERRA (Model 717). This copper-lined shield provided 2.5 cm of lead around the cylindrical portion of the detector. A collimating insert was attached to the front of the cylindrical shield, providing 2.54 cm of lead shielding and 0.641 cm of copper shielding. A 1 cm-diameter aperture extended through this insert. Figure 5.5 shows the cylindrical shield and collimator insert.

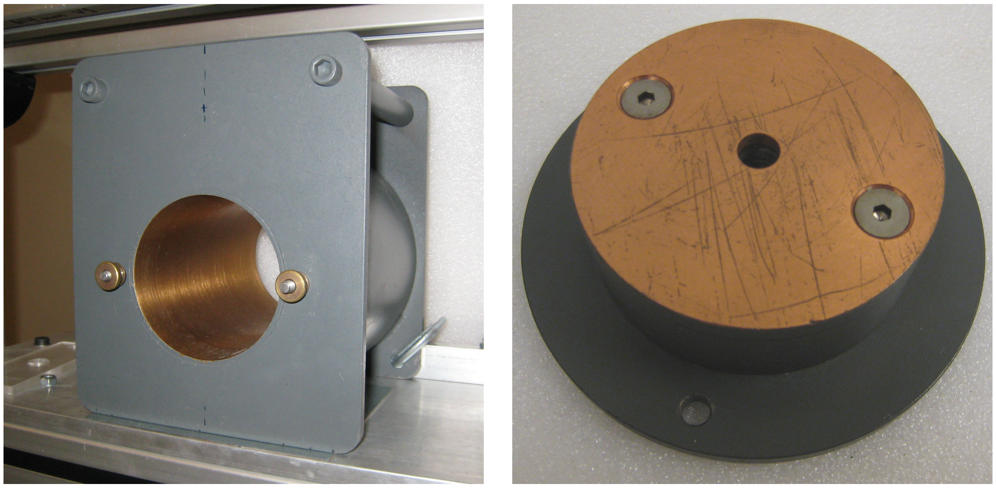

(a) (b)

Figure 5.5: Photographs of (a) the low-background shield and (b) the 1 cm-diameter collimator that were used for VS2000 spectrum measurements.

5.2.3 Measurement setup and procedure

5.2.3.1 CS measurement technique

The VS2000 source was used with a remote afterloader system that deployed the source through a plastic catheter. The terminal end of the catheter was taped to a lead brick with the catheter's cylindrical axis oriented parallel to the scattering rod's axis. This part of the catheter was surrounded by a rectangular arrangement of lead bricks that attenuated all photons that were not directed towards the scattering rod.

These CS measurements used an aluminum scattering rod that was 3.175 cm in diameter and 6.525 cm in length. This diameter was substantially large so that photons were likely to undergo multiple CS events in the scattering rod. While this is undesirable for CS spectrometry, in which conventional corrections assume only single scattering, these dimensions were sufficient for a demonstration of the technique.

Measurements were performed with the collimated detector placed at scattering angles of 50°, 60°, 70°, 80°, and 90° relative to the central axis of the source. Determination

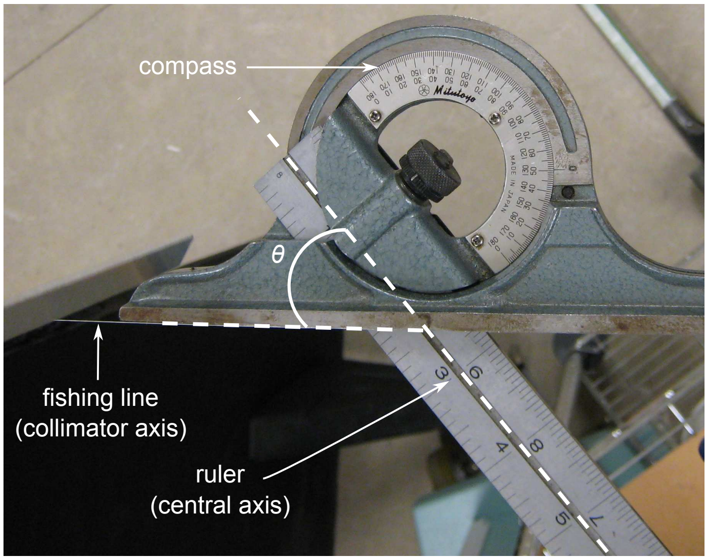

Figure 5.6: Photograph of the string alignment system that was used to determine scattering angles for the VS2000 spectrum measurements.

of the scattering angle was facilitated by the use of a string alignment system in which a monofilament line was secured between the center of the collimating aperture and the scattering rod. This monofilament line was coincident with the axis of the collimator. The scattering angle, which was defined between the monofilament line and a ruler that was secured along the central axis of the source, was measured using a precision square with a protractor head (see Figure 5.6). The scattering rod was positioned at the intersection of the monofilament line and ruler at distance of approximately 50 cm from the source. For all measurements, the REGe detector was placed approximately 300 cm from the scattering rod. The exact scatterer-to-detector distance was slightly different for each measurement. Each PHD was collected for 15 minutes. Figure 5.7 shows the experimental measurement system.

5.2.3.2 Background measurement technique

For the VS2000 measurements, background was accounted for using a different methodology than was discussed in Section 4.2.2.3. For each scattering angle, 15-minute-long background

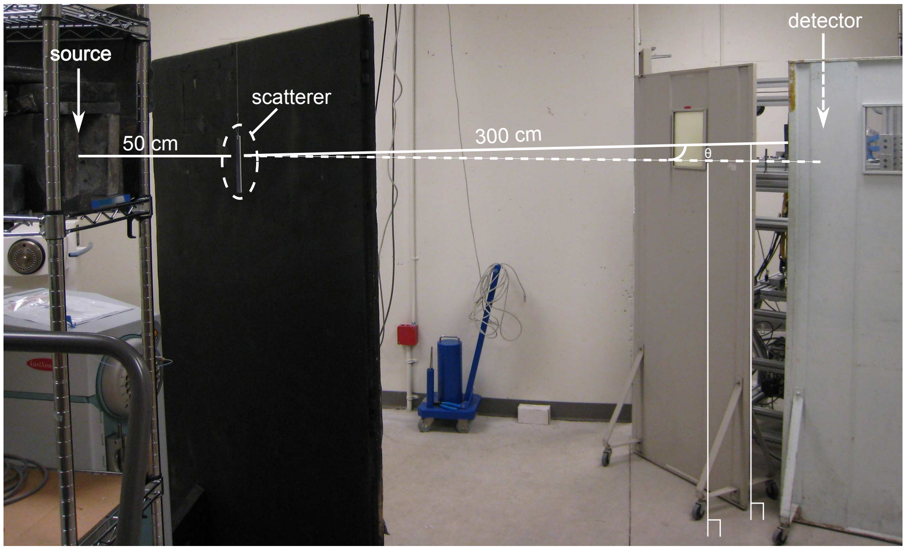

Figure 5.7: Photograph of the experimental setup for measurements of the Varian VS2000 ^{192}Ir source using the CS spectrometry arrangement.

measurements were performed with the source deployed, but without the scattering rod in place. The collimating aperture remained open for these measurements. This method accounted for room-scattered and leakage photons from the primary source. Background was removed from each spectrum measurement using channel-by-channel subtraction. This method only partially accounted for background because it neglected the background due to transmission photons coming from the scattering rod.

5.2.3.3 Measurement corrections

An energy calibration measurement was performed using a Type D multinuclide standard source (Isotope Products, Inc., Valencia, CA) with well-known emission energies. For this measurement, the source was placed inside of a poly(methyl methacrylate) holder that attached to the low-background shield around the detector. This holder centered the calibration source in front of the detector at a distance of about 5 cm. The energy calibration PHD was collected for 12 hours. Following data collection, the Genie$^{\text{TM}}$ 2000 software was used to determine a relationship between energy and PHD channel. This energy calibration was then applied to all CS measurements of the ^{192}Ir source.

The detector response was unfolded from the background-subtracted PHD according to the Gold deconvolution technique that was described in Section 2.1.3.1. The DRF for this correction was generated using an MC model of the detector, the low-background shield, and the collimator. These simulations did not model the CS geometry. Thus, the Gold deconvolution for these measurements accounted for only the artifacts introduced to the PHD by the detector, low-energy shield, and collimator. Application of the Gold deconvolution unfolded the spectrum that was incident on the detector. This spectrum was then manually corrected for the kinematic CS relations and the Klein-Nishina (KN) relationship, as was discussed in Section 2.3.

5.2.4 Results

The photon spectrum for an encapsulated ^{192}Ir source includes nearly 20 separate peaks ranging in energy from around 10 keV to 885 keV (Borg and Rogers, 1999). The fluence of each of the peaks was greatly reduced after applying the CS technique. In fact, this CS process was so efficient in reducing the fluence that some of the less-abundant peaks could not be resolved in the measured PHD. Thus, for this demonstration, only the more abundant high-energy peaks of the ^{192}Ir spectrum (295 keV, 308 keV, 316 keV, 468 keV, and 588 keV) were used.

The deconvolved spectra, prior to being corrected for the CS interactions, are shown in Figure 5.8. Due to the size of the scattering rod and collimator, the detector accepted photons that were scattered within a few-degree window around the nominal scattering angles. Thus, the shapes of the scattered peaks were broad rather than sharply peaked. The broad shapes of the peaks indicate that this geometry was not ideal for CS measurements; however, these measurements demonstrate the validity of the CS spectrometry process.

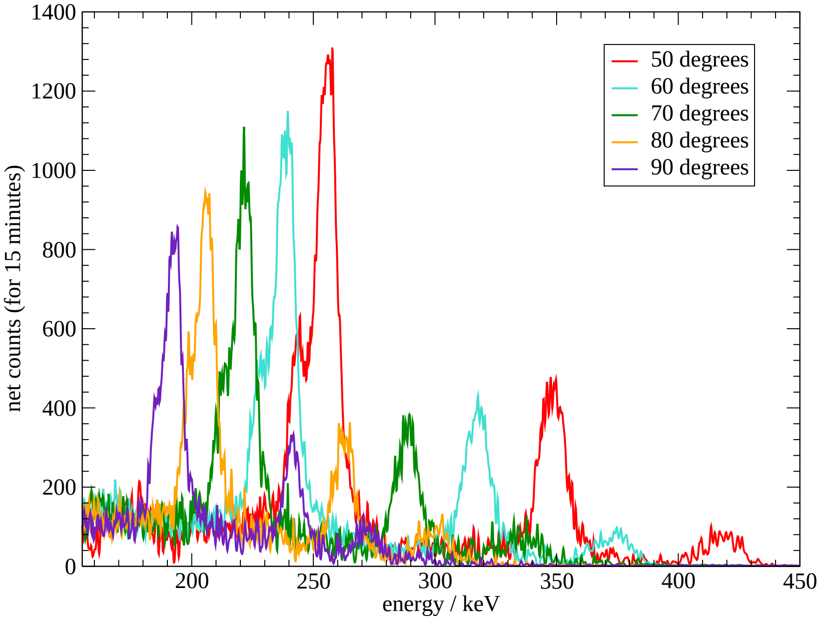

Figure 5.8: Measured spectra for CS experiments with the VS2000 ^{192}Ir source that were performed at scattering angles of 50°, 60°, 70°, 80°, and 90°. These spectra have been corrected for background and for artifacts that were introduced by the detector and collimator.

Figure 5.8 illustrates that the positions of the scattered ^{192}Ir peaks were affected by the scattering angle. Specifically, the energy of a scattered peak decreased with increasing scattering angle. In addition, the magnitude of each of the peaks was inversely related to the scattering angle.

After manually correcting for the kinematic CS relations and KN cross section, the reconstructed peaks for each of the measurements overlapped at the proper energies, as shown in Figure 5.9. Due to the CS geometry (i.e., scattering rod dimensions, collimating aperture diameter), the 295 keV, 308 keV, and 316 keV peaks were not fully resolvable from one another. Furthermore, the magnitudes of the reconstructed peaks varied with scattering angle due to attenuation in the scattering rod that was not accounted for in the measurement corrections. These inconsistencies could be avoided by refining the CS geometry or by applying a more comprehensive DRF that accounts for the scattering geometry. Despite these

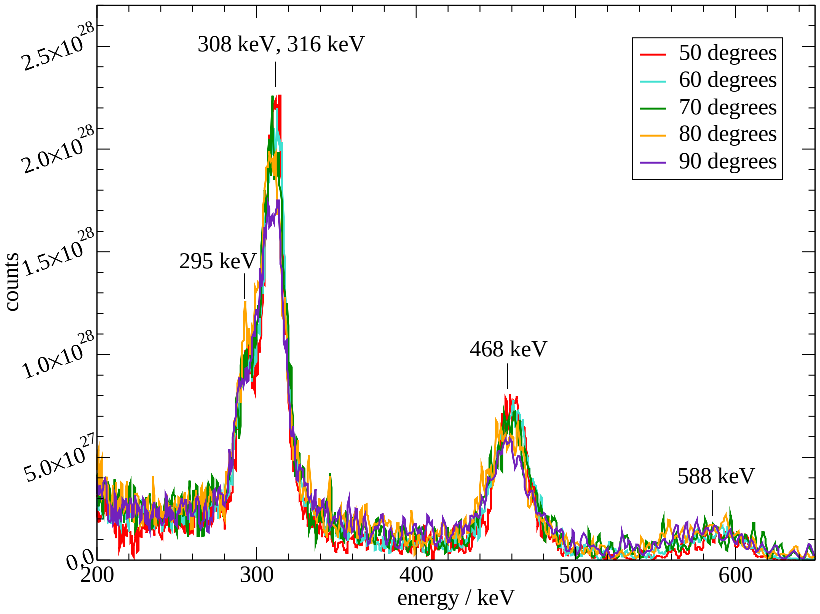

Figure 5.9: Measured spectra for CS experiments with the VS2000 ^{192}Ir source after applying corrections for the CS and KN relations.

small disagreements, these measurements demonstrate that the CS technique is viable for a medium-energy and medium fluence rate source. Furthermore, the measurement corrections that were applied adequately correct the measurements for the CS spectrometry system. These results support the use of this CS technique in the measurement of higher-energy and higher fluence rate sources.

Chapter 6

Characterization of the T1000 teletherapy spectrum

This work involved the determination of the spectrum of the ^{60}Co teletherapy system installed at the University of Wisconsin Accredited Dosimetry Calibration Laboratory (UWADCL). The following sections discuss the specifications of the system and the spectroscopic characterization that was performed using Monte Carlo (MC) simulations and measurements. Comparisons are made between these two methods.

6.1 System description

Cobalt-60 teletherapy systems consist of a source and treatment head. There are a variety of commercially available models for both of these components, which result in multiple possible system configurations. The dosimetric parameters of a teletherapy system are affected by the particular combination of these components (see Section 2.2.2.2), indicating that individual teletherapy systems must be independently characterized. The system at the UWADCL consisted of a Theratronics T1000 treatment unit (MDS Nordion, Kanata, ON, Canada) that was equipped with a 2.0 cm-diameter INIS-SF-2.7-4-SD ^{60}Co source (International Isotopes, Inc., Idaho Falls, ID). According to the source's calibration certificate, its activity was 8,461 Ci on June 18, 2008.

The source contained cylindrical pellets (1 mm tall by 1 mm in diameter) of nickel-encapsulated ^{60}Co. These pellets were double-encapsulated by two nested stainless-steel canisters with welded endcaps. The height of the inner canister, which contained the pellets, was approximately 3.0 cm; however, the height of the active material within this canister was not specified by the manufacturer. The space within the inner canister that was not occupied by ^{60}Co pellets was filled with a stainless-steel spacer. The source capsule sat inside of a tungsten sleeve that was housed in a sliding brass drawer. This drawer was shielded in the treatment head when the source was not exposed and was centered in front of the primary collimator for irradiations.

Primary collimation was provided by an immobile tungsten aperture that was created by four diverging surfaces. Secondary collimation was provided by a set of eight interlocking, movable lead leaves. These leaves were mobilized by stainless-steel bars that were attached to the primary collimator with hinges. Final collimation was provided by a set of tungsten trimmer bars that were positioned approximately 45 cm from the source.

6.2 Monte Carlo methods

MC investigations of the T1000 unit were performed using the Monte Carlo N-Particle (MCNP5) code with coupled photon and electron transport. Simulations of percentage depth-dose (PDD) curves and cross-beam profiles were used to benchmark this MC model against measurements. In addition, this model was used to perform spectroscopic characterizations of the system for a variety of source model parameters.

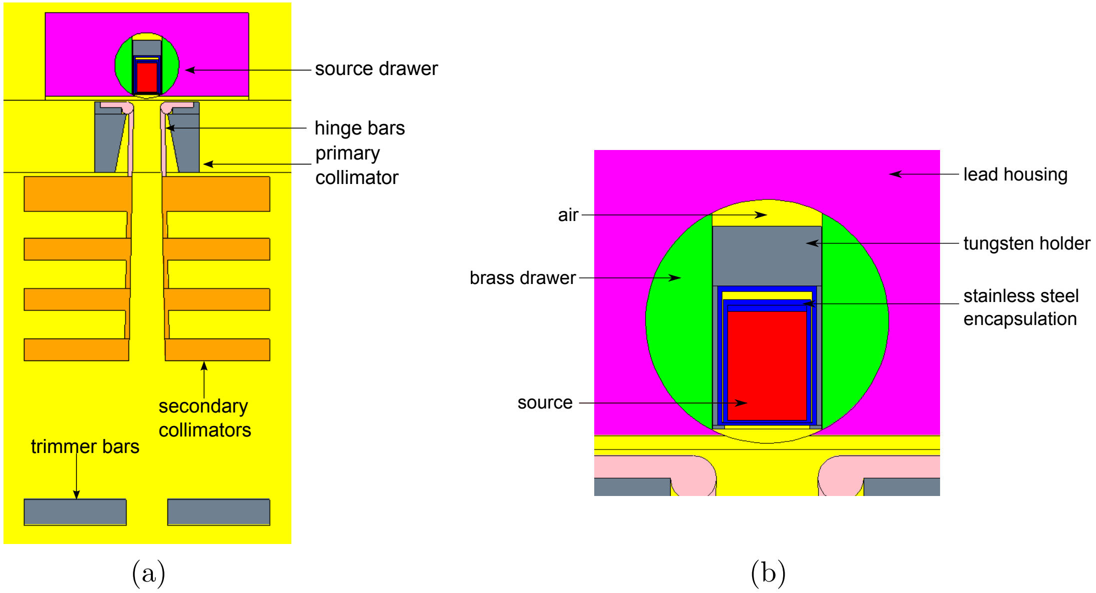

(a)

(b)

Figure 6.1: VisEd rendering of (a) the cross section of the MCNP5 geometry for the T1000 teletherapy unit and (b) a magnified view of the source.

6.2.1 Geometry of the T1000

The model of the T1000 teletherapy system was adapted from an MCNP5 model of an Eldorado 78 system (MDS Nordion, Kanata, ON, Canada) that was created by Smilowitz (2002). The head of the treatment unit was similar for these two models, but substantial differences existed in the source, source encapsulation, and collimation. The changes to the MCNP5 geometry were determined from manufacturer specifications and comparison with dosimetric measurements. Figure 6.1 shows a Visual Editor (VisEd) rendering of the system. The following discussion details the development and verification of the system model.

6.2.1.1 Verification simulations

Simulations of PDD and cross-beam profiles were performed for a (10 x 10) cm^2 field in a model of the UWADCL's (50 x 50 x 50) cm^3 water tank. For these simulations, the *F8 energy deposition tally was used to score the energy deposited in water along the central

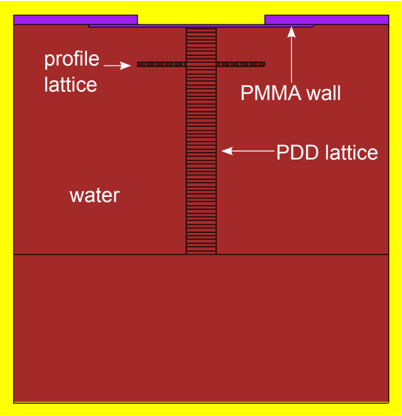

Figure 6.2: VisEd rendering of the UWADCL's water tank and the lattice geometries that were used for MC calculations.

axis and across the field. Both the PDD and cross-beam profiles were scored in a lattice geometry as shown in Figure 6.2. The voxel size was (2 x 2 x 0.5) cm^3 for the PDD calculations and (2 x 0.25 x 0.5) cm^3 for the cross-beam profile calculations. The variance reduction techniques used for these calculations were energy cutoffs, geometry splitting, and Russian roulette. A global energy cutoff of 10 keV was used for photons. The electron energy cutoff was 500 keV in all cells of the problem except for the water tank, in which it was 250 keV. Geometry splitting and Russian roulette were used to increase the number of particles in important cells in the problem and kill particles in less important cells.

6.2.1.2 Verification measurements

Measurements of PDD and cross-beam profiles were used to benchmark the MC model of the T1000 system. The PDD profile was measured for a (10 x 10) cm^2 field in a water tank. The surface of the tank was defined by a 0.28 cm-thick poly(methyl methacrylate) (PMMA) window, the back of which was placed at a source-to-surface distance (SSD) of 95 cm. These measurements were performed using two ionization chambers, an Exradin A16 microionization chamber and an Exradin A12 Farmer-type chamber (Standard Imaging, Middleton, WI). Both sets of measurements were completed using a MAX-4000 electrometer (Standard Imaging) with an applied collecting-electrode bias of +300 V (i.e., collecting negative charge). PDD measurements were performed along the central axis for depths ranging from (2 to 30) cm. Shallower depths were prohibited due to the size of the ionization chamber holder. All data were shifted to shallower depths to account for the difference between the depth of the central electrode and the effective point of measurement (Almond et al., 1999). The PDD curves were normalized at a depth of 10 cm. The cross-beam profile data used in this work were taken from McCaw et al. (2011), who performed profile measurements for the T1000 using EBT2® radiochromic film (International Specialty Products, Wayne, NJ). Measurements were performed for a (10 x 10) cm^2 field at a depth of 5 cm in Virtual Water™ (VW). An additional 5 cm-thick slab of VW was placed behind the film to provide backscatter. The film's optical density was related to dose by a sensitometric response curve that was created from calibration films. The data were normalized to the dose on the central axis.

6.2.1.3 Source capsule

The source encapsulation and housing were modeled according to manufacturer specifications. The primary source was defined inside the source encapsulation and included isotropic (1.17 and 1.33) MeV photons with equal probabilities of emission. As was discussed in Section 6.1, the source capsule was filled with an unknown active height of small cylindrical ^{60}Co pellets. Rather than model the individual pellets (physical density, $\rho = 8.9\,\text{g}\cdot\text{cm}^{-3}$), the active source was modeled as a homogeneous cylinder of ^{60}Co with a reduced density to account for source packing. This method was used by Mora et al. (1999) and Tedgren et al. (2010) for similar source geometries. Because the packing density was not specified by the manufacturer, this reduced density had to be determined for the T1000 system. Likewise, the active height of the source, which was stated by the manufacturer to be between (1.5 and 2.97) cm, had to be determined. A sensitivity study for each of these parameters was performed to establish a combination of source height and density that gave simulation results in agreement with measurements.

Sensitivity studies The source density and height affected the internal scatter in the encapsulated source. Increasing the values of these parameters was expected to increase the magnitude of the low-energy scatter exiting the treatment head. These kinds of changes in spectra tend to have a larger effect on PDD than on cross-beam profiles; thus, the sensitivity studies in this work focused on PDD simulations.

All PDD calculations were performed for a (10 x 10) cm^2 field. These simulations were completed for source densities, ρ_{MC}, of (5.7, 5.8, and 5.9) $\text{g} \cdot \text{cm}^{-3}$ and source heights, h_{MC}, of (1.5, 2.0, and 2.5) cm. The density values were selected based on similar published works, and the height values were selected to test a wide range of values. For each h_{MC}, a stainless-steel spacer filled the empty space in the inner canister. All combinations of ρ_{MC} and h_{MC} were tested. The PDD data were normalized at a depth of 10 cm. Figure 6.3 shows the results of these sensitivity studies.

The PDD was relatively insensitive to changes in ρ_{MC} and h_{MC} within the ranges that were tested. For each ρ_{MC}, the maximum standard deviation in PDD across the three heights at any depth was below 0.6 %. For each h_{MC}, the maximum standard deviation in PDD across the three densities at any depth was below 0.2 %. To determine the final ρ_{MC} and h_{MC} parameters that were representative of the unit, the results of the sensitivity studies were compared to the PDD measurements that were performed with the Exradin A16 and A12 ionization chambers. The percentage error between the calculated and measured PDD values for each ionization chamber are shown in Figure 6.4.

For the Exradin A16 measurements, the disagreement between the calculated and measured PDDs increased with depth. Specifically, the measured values became increasingly larger than the calculated values. This trend was observed for all source density-height combinations, which indicated a potential problem with the measurement results. Two pro-

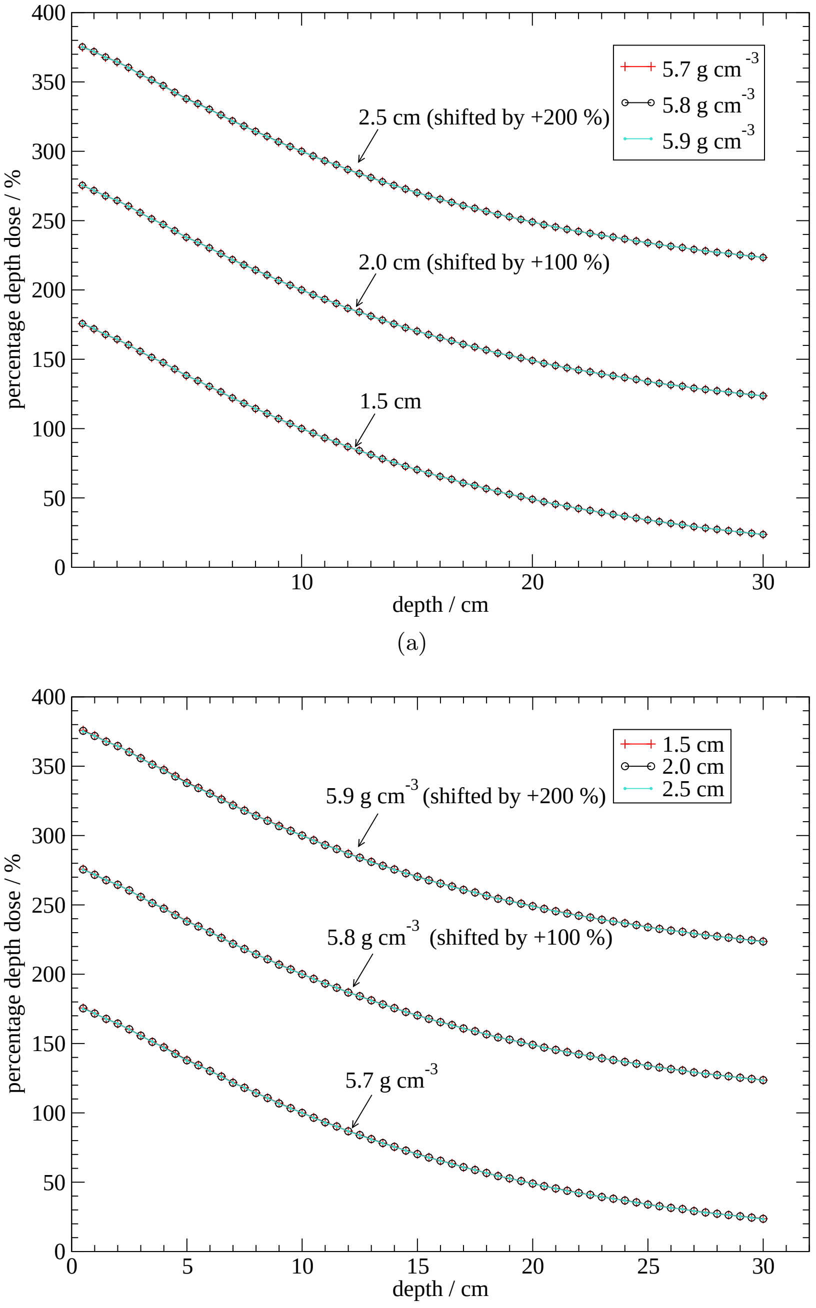

(a)

(b)

Figure 6.3: Calculated PDDs for various source densities and heights. (a) compares PDD as a function of source density, and (b) gives the same data as a function of source height. Two data sets in each plot have been offset by either 100 % or 200 % so that all data could be easily viewed on the same plot.

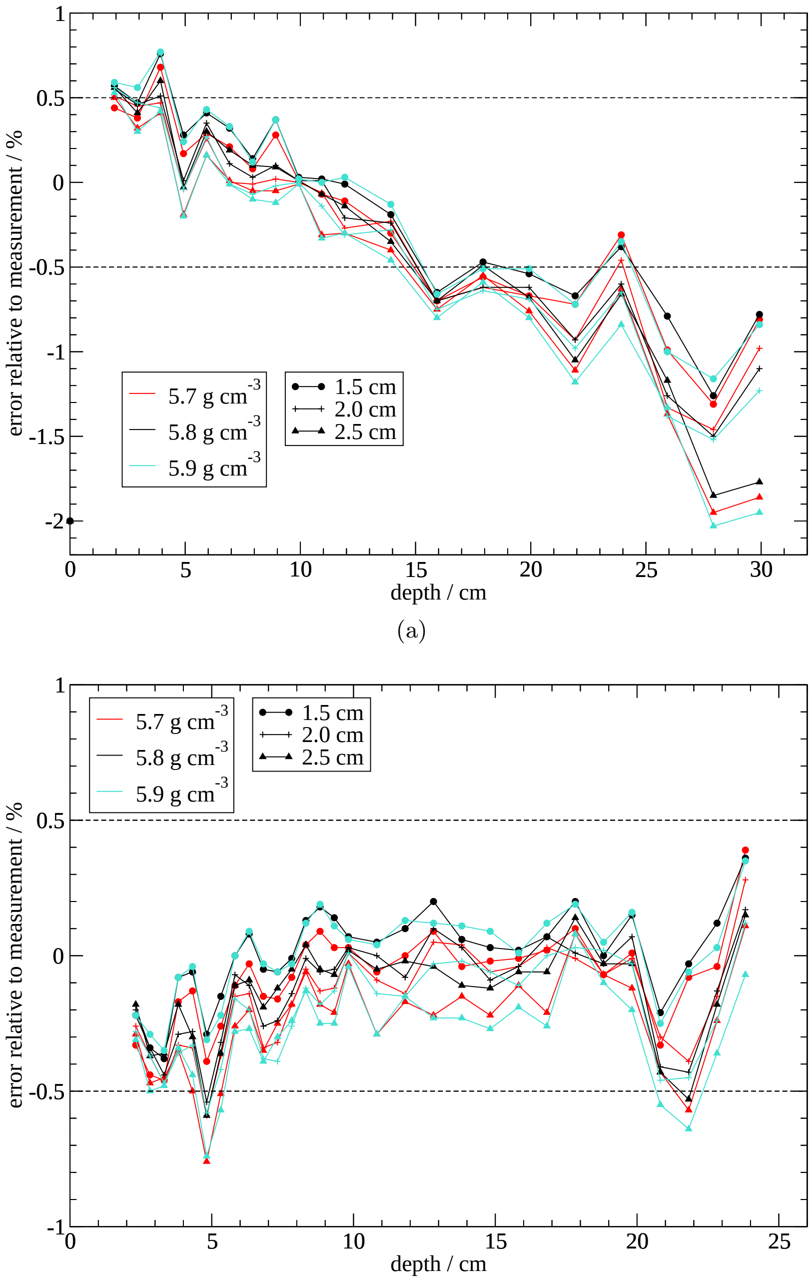

(a)

(b)

Figure 6.4: Percentage error between calculated and measured PDD values for measurements performed with the (a) Exradin 16 and (b) Exradin A12 ionization chambers.

cesses may explain this trend. First, it is known that some microionization chambers exhibit increases in signal due to the irradiation of the chamber's stem and cable (Campos and Caldas, 1991; Agostinelli et al., 2008). In this work, the amount of irradiated stem and cable increased with the measurement depth. Although the magnitude of the stem effect was not explicitly determined, this could have led to extraneous signal that would overestimate dose with depth. Second, microionization chambers with high-Z collecting electrodes have been shown to overrespond to low-energy photons (Martens et al., 2000). At megavoltage energies, Martens et al. (2000) found that the original PTW PinPoint microionization chamber (model 31006, PTW-Freiburg, Freiburg, Germany), which had a steel collecting electrode, overresponded with increasing depth and field size due to the contribution of low-energy photons. Like the PTW 31006 PinPoint chamber, the Exradin A16 chamber has a high-Z collecting electrode (silver-plated copper-clad steel) which could lead to an overestimate in dose with depth.

Final parameters Because the trends seen in Figure 6.4a may be explained by known processes, the Exradin A16 measurements were not used to benchmark the MC model of the T1000 unit. The Exradin A12 measurements did not exhibit this trend, as is evident in Figure 6.4b. Thus, the Exradin A12 measurements were used to determine ρ_{MC} and h_{MC} for the T1000 model. With the exception of a few depths, MC results for all combinations of ρ_{MC} and h_{MC} yielded PDDs for which values at all depths were within $\pm 0.5\,\%$ of the values determined with the Exradin A12. Because the differences in the MC-calculated PDDs at each depth were not statistically significant, the median value for each of the parameters ($\rho_{\mathrm{MC}} = 5.8\,\mathrm{g \cdot cm^{-3}}$, $h_{\mathrm{MC}} = 2.0\,\mathrm{cm}$) was selected. Figure 6.5a shows the agreement between the final calculated and measured PDD profiles for a (10 x 10) cm^2 field.

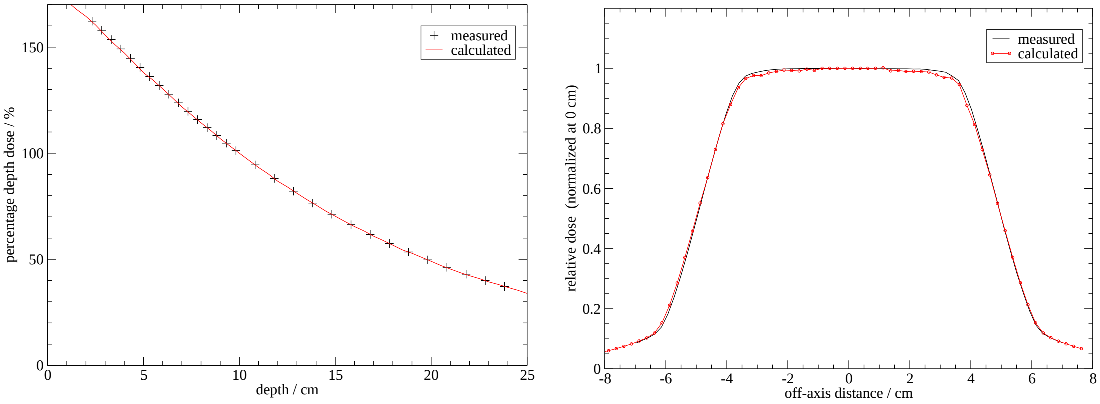

(a) (b)

Figure 6.5: Final calculated and measured (a) PDDs and (b) cross-beam profiles for a (10 x 10) cm^2 from the T1000 system.

6.2.1.4 Collimation system

The size of the primary collimator opening that was proximal to the source was provided by the manufacturer and was modeled accordingly. The remaining parameters of the collimation system (e.g., angular divergence of the primary collimator, thickness and spacing of the secondary collimator leaves, angular divergence of the secondary collimator) were not explicitly defined. As such, many dimensions used for the T1000 model were taken from the Eldorado 78 model that was developed by Smilowitz (2002). The divergence of the secondary collimator leaves was determined by comparison of cross-beam profile simulations and measurements. Figure 6.5 shows the agreement between the simulated and measured cross-beam profiles for a (10 x 10) cm^2 field.

6.2.2 Spectra determination

The spectrum of the T1000 system was also simulated using MCNP5. The in-air spectra were calculated in an air medium that had the material composition and density defined by NIST (Berger et al., 2005a). The F5 point detector fluence tally was used for these spectra calculations. No variance reduction was used, although the point detector tally itself may be construed as a variance reduction technique. The following sections discuss studies that were performed to determine the sensitivity of the spectrum to various source parameters and structural components.

6.2.2.1 Source parameter sensitivity

An MC model is generally benchmarked by comparing measured and calculated PDD and cross-beam profiles; however, as was discussed in Section 6.2.1, the PDD for the T1000 unit was insensitive to changes in source density and source height. These parameters affect the amount of scatter within the source capsule and, thus, affect the spectrum. The effects of source density and height on the T1000 spectrum were simulated for ρ_{MC} of (5.7, 5.8, and 5.9) $\mathrm{g \cdot cm^{-3}}$ and h_{MC} of (1.5, 2.0, and 2.5) cm. All combinations of ρ_{MC} and h_{MC} were investigated. The spectra were calculated in air for a field size of (10 x 10) cm^2. All spectra were normalized to the peak height at an energy of 1.33 MeV. Figure 6.6 shows the results of this study.

As seen in Figure 6.6, the shape of the spectrum changed with the source density and height. This figure features three general groups of spectra, each which corresponds to a specific source height. This particular grouping occurred because the source height variation was larger than the source density variation for this investigation; however, it is likely that the grouping is actually dependent on the product of source height and source density. In general, each spectrum has two prominent peaks from the primary ^{60}Co emissions. Between these two peaks and in the lower-energy region, there are distributions of photon energies that originate from scatter within the source capsule and its surrounding housing. The magnitude of these scatter regions increased with source height. The results of these simulations are compared to measurement results in Section 6.4.

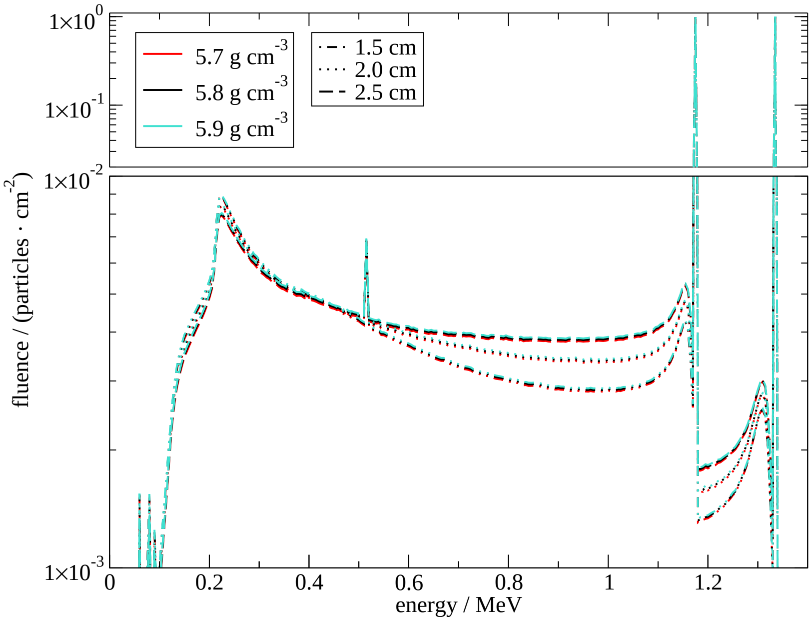

Figure 6.6: Calculated spectra for the T1000 ^{60}Co system for various source densities and heights. The spectra have been normalized at the position of the 1.33 MeV peak.

6.2.2.2 Structural contributions

The effects that the T1000 structural components had on the spectrum were investigated in a series of simulations in which ρ_{MC} was $5.8\,\mathrm{g}\cdot\mathrm{cm}^{-3}$ and h_{MC} was 2.0 cm. In the first simulation of this series, the source was modeled as an air-filled canister that isotropically emitted 1.17 MeV and 1.33 MeV photons. The remainder of the geometry was modeled as air. In the next simulation, the source was modeled realistically as a capsule that was filled with cobalt material. Each subsequent simulation included an additional feature of the T1000 structure. The specific components that were modeled in each investigation are shown in Table 6.1. For each investigation, the spectrum, which was calculated at 100 cm from the source, was normalized to the differential fluence value at 1.33 MeV. The results of this study are shown in Figure 6.7.

When the entire geometry was modeled as air (Simulation 1), the spectrum at 100 cm was dominated by the two ^{60}Co emissions. A low-energy continuum that was small in magnitude

Table 6.1: Description of the series of MC simulations that were performed to investigate the effect of the T1000 structure on the spectrum.

Simulation #	Structures modeled
1	None
2	Source capsule
3	Source capsule, housing
4	Source capsule, housing, primary collimator
5	Source capsule, housing, primary collimator, secondary collimator, trimmer bars

was present due to scattering events and bremsstrahlung from interactions in the air. The addition of the cobalt material and capsule structure (Simulation 2) led to a more substantial relative amount of low-energy scatter that was further increased by the housing (Simulation 3). The addition of the primary collimator (Simulation 4) altered the magnitude and shape of the low-energy distribution. Specifically, the relative magnitude of the scatter below approximately 700 keV decreased while the relative magnitude of the scatter above 700 keV increased. Finally, the secondary collimators and trimmer bars (Simulation 5) decreased the relative magnitude of the scatter while substantially affecting the shape of the scatter regions just below each of the primary ^{60}Co peaks. These results demonstrate that the spectra of ^{60}Co teletherapy systems are strongly affected by their structural components, and each combination of components should be characterized independently.

6.3 Measurement methods

The spectrum of the T1000 system was characterized using Compton-scattering (CS) measurements, as well. The following section discusses the measurement techniques that were used and the resulting spectra that were determined.

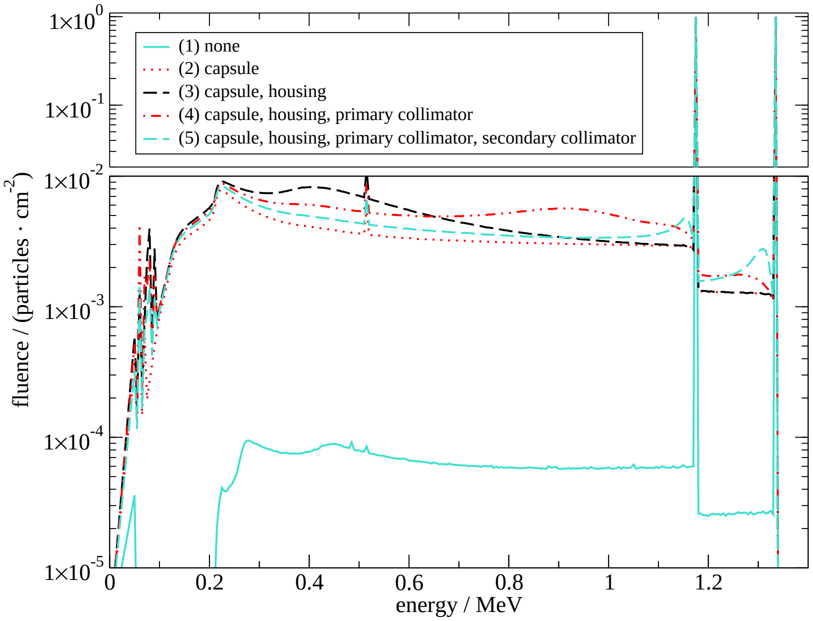

Figure 6.7: Contributions to the T1000 spectrum from various structural components. All spectra were normalized at the position of the 1.33 MeV peak.

6.3.1 Compton spectrometry setups

The central-axis photon spectrum was measured for a (10 x 10) cm^2 field using the four different CS measurement arrangements that are shown in Table 6.2. Figure 6.8 shows two photographs of the CS spectrometry system that was used for these measurements.

The basic electronics components that were used for these measurements were discussed in Section 4.2.1.1. The fast-spectroscopy linear amplifier was operated with a shaping time of 4 μs, a coarse gain of 100, and a fine gain of 0.55. All measurements were performed using the unipolar output from the linear amplifier.

Each pulse-height distribution (PHD) was acquired for at least five hours. Background measurements were performed for each of the measurement arrangements, as well. For these measurements, the collimator was plugged with a 16 cm-long tungsten rod. An additional 10 cm of lead was placed in front of the collimating aperture. The acquisition time for each background measurement was at least four hours.

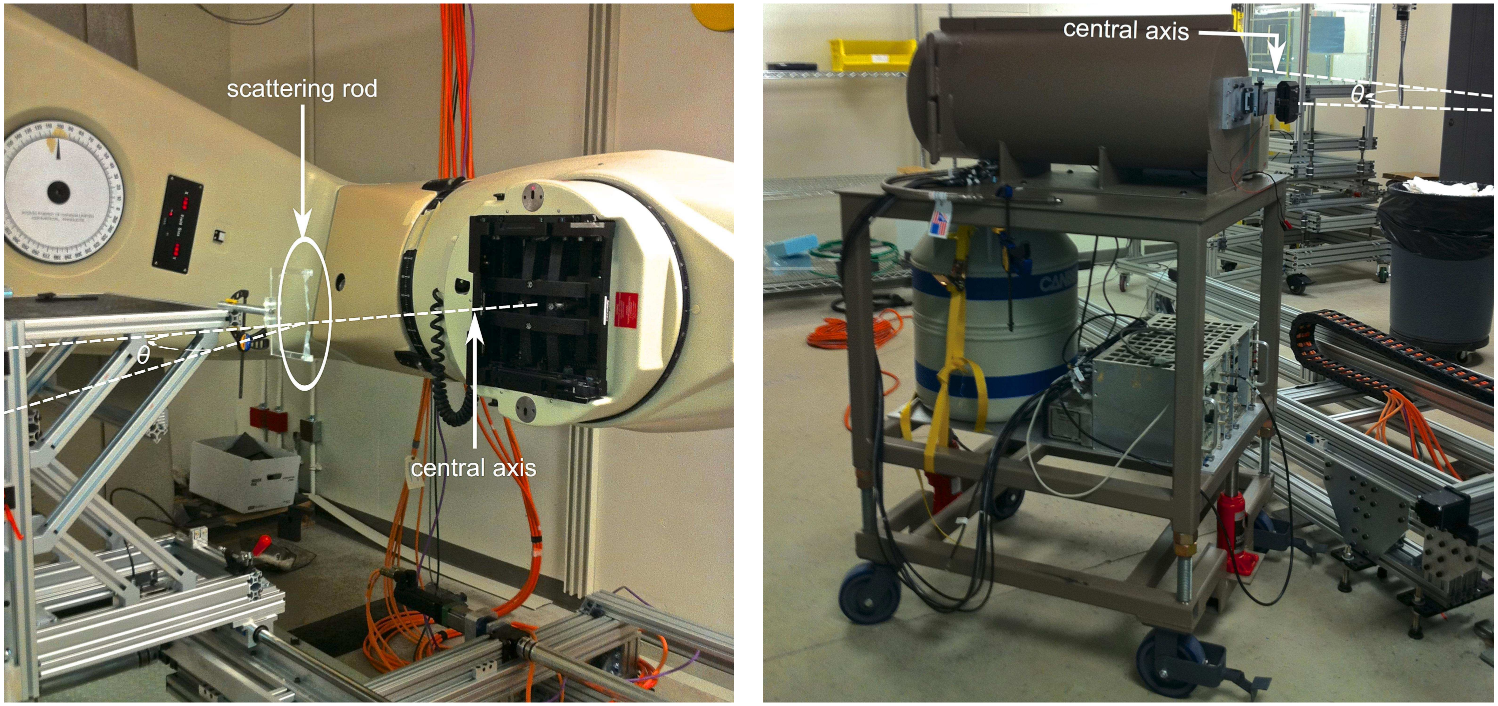

(a)

(b)

Figure 6.8: Photographs of the CS spectrometry system that was used for spectra measurements of the T1000 ^{60}Co system. (a) shows the scattering rod centered on the central axis, and (b) shows the detector and its shielding that are aligned with the scattering rod. In this figure, the alignment laser is attached to the front of the collimator.

Table 6.2: CS spectrometry parameters that were used to measure the spectrum of a (10 x 10) cm^2 field for the T1000 ^{60}Co system.

θ (degrees)	Source-to-scatterer distance (cm)	Scatterer-to-detector distance (cm)
22.8	100	250
31.3	100	150
48.1	100	200
70.1	100	160

The CS and background measurements were smoothed using the Genie$^{\text{TM}}$ 2000 moving-average smoothing function. The background PHDs were scaled to account for the differences in acquisition times from their corresponding CS measurements. The CS measurements were then corrected for background using channel-by-channel subtraction. Finally, the background-subtracted PHDs were corrected for artifacts that were introduced by interactions in the detector, shield, and CS geometry using the Gold deconvolution technique (see Section 2.1.3.1). The corrected measurements represented the primary spectrum at 100 cm from the source.

6.3.2 Results

The background-corrected PHDs, which have not been corrected for the detector response or CS geometry, are shown in Figure 6.9. Each of the PHDs exhibited two defined peaks, which correspond to the primary ^{60}Co emissions, and a lower-energy continuum. Similar to what was observed with the VS2000 ^{192}Ir PHDs in Section 5.2.4, the positions of the scattered ^{60}Co peaks were affected by the scattering angle. In particular, the CS peak energies decreased with increasing scattering angle. The centroid of each of the peaks in Figure 6.9 agreed with the energy predicted by the equation for CS from free electrons within $\pm 2\,\text{keV}$ (see Equation 2.17). These values are labeled in Figure 6.9.

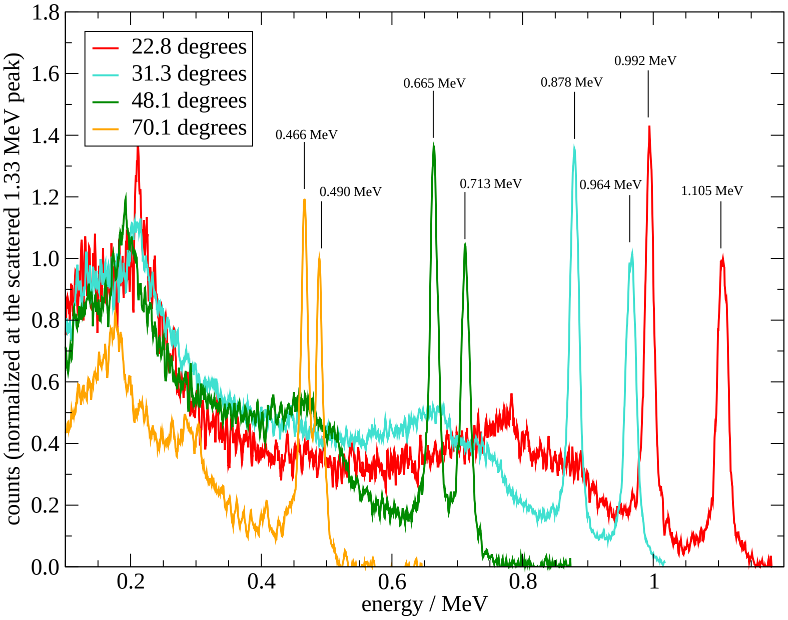

Figure 6.9: Measured PHDs for CS experiments with the T1000 ^{60}Co system that were performed at scattering angles of 22.8°, 31.3°, 48.1°, and 70.1°. These PHDs have been corrected for background only. Each PHD was normalized at the energy of the scattered 1.33 MeV peak. The peak labels represent the scattered peak energy that was calculated assuming CS from free electrons.

Although the pure ^{60}Co source emitted two discrete photon energies, the scattered peaks had substantial width. The broadening of these CS peaks occurred for a few reasons. First, due to the CS measurement geometry, the detector accepted photons that were scattered within a small window around the nominal scattering angles. Table 6.3 shows the minimum and maximum scattering angles that were accepted by the detector based on the source diameter (2 cm), scattering rod dimensions (diameter, 0.6 cm; length, 2.25 cm), source-to-scatterer distance (100 cm), scatterer-to-detector distance (variable), and collimating aperture diameter (0.2 cm). The method that was used to determine these values is discussed in Appendix A. In addition to this window of scattering angles, each of the scattered peaks was affected by Doppler broadening. This process, which was described in Section 2.3, causes a distribution of scattered photon energies for a single scattering angle and incident energy. Finally, the REGe detector and electronics modules exhibited inherent peak broadening

Table 6.3: Minimum and maximum scattering angles, θ, that were accepted by the detector due to the measurement geometry for each of the CS measurements.

Nominal θ (degrees)	Minimum θ (degrees)	Maximum θ (degrees)
22.8	21.97	23.70
31.3	30.41	32.26
48.1	47.26	48.97
70.1	69.26	70.95

due to the statistical distribution of charge carriers produced for a given energy deposition and fluctuations in the signal amplification process. For the electronics settings that were used, the system had a full-width-at-half-maximum of 3.7 keV for a 661 keV peak. The combination of each of these processes caused the peak broadening seen in Figure 6.9. The magnitude of this broadening was inconsequential for the measurements made with the smaller scattering angles (22.8° and 31.3°); however, for the larger scattering angles (48.1° and 70.1°), the CS peaks were not fully resolvable due to the broadening. Using the conventional CS corrections that were discussed in Section 2.3.2, this loss in resolution is permanent; however, using the unfolding method that was developed for this work (see Section 4.2.3), the loss in resolution can be accounted for.

In addition to the scattered ^{60}Co peaks, each PHD exhibited a low-energy continuum. This continuum resulted from two components. First, as was seen in the simulations in Section 6.2.2, the T1000 spectrum at 100 cm from the source in air had a low-energy continuum due to scatter in the source capsule and treatment head. Thus, a portion of the low-energy regions in the PHDs can be attributed to these photons. The larger component of the low-energy continuum came from interactions in the REGe detector and shield. This portion of the PHD was corrected for using the detector response function (DRF).

Figure 6.10 shows the corrected CS spectra that were obtained by applying a minimum of 10,000 iterations of the Gold deconvolution, which accounted for artifacts that were introduced by the entire CS system, using the measurement-specific DRFs. Each of the

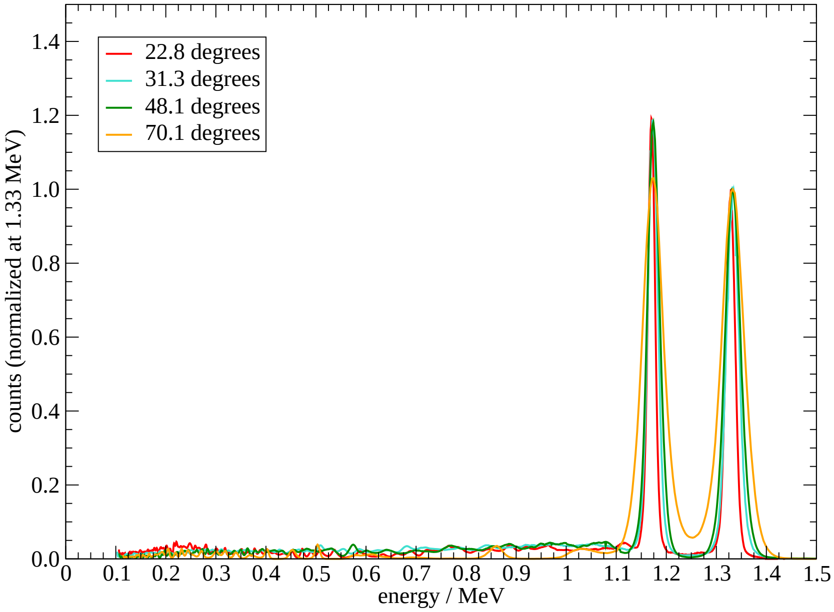

Figure 6.10: Measured spectra for CS experiments with the T1000 ^{60}Co system that were performed at scattering angles of 22.8°, 31.3°, 48.1°, and 70.1°. These spectra were unfolded from their respective PHDs by applying a minimum 10,000 iterations of the Gold deconvolution. Each spectrum was normalized at the position of the 1.33 MeV peak.

spectra were normalized at the position of the 1.33 MeV peak. This figure shows that the reconstructed peaks for each of the measurements overlapped at the proper energies. In addition, the peaks for the measurements completed at large scattering angles were resolvable. The peak broadening in each of the spectra was slightly different due to the variations in the scattering geometries that were used. These differences could potentially be reconciled by applying more iterations of the deconvolution.

The unfolding method that was developed for this work provided adequate corrections to the ^{60}Co peaks. In addition, with the exception of the spectrum for 70.1° scattering, the low-energy regions showed good agreement among the spectra that were corrected with this technique. The reason for the discrepancy with the 70.1° spectrum stems from the simulated PHD shown in Section 4.1.2.3 (Figure 4.6d). This figure shows that the simulated PHD (i.e., the expected measured PHD) had a larger low-energy component than the measurement did. Thus, the corrections for the measured PHD overcorrected this low-energy region.

6.4 Spectra comparisons

The following section discusses how the spectroscopic variations that were seen in Sections 6.2 and 6.3 affect two metrics that are commonly used to describe source output. The relative fluences for various portions of the spectra will be discussed. In addition, the average energies of the spectra will be compared.

6.4.1 Relative fluence contributions

For all of the simulated and measured spectra, the magnitudes of the two equiprobable ^{60}Co emissions were slightly different; however, the areas under the peaks were similar, as is shown in Table 6.4, which presents the relative fluences for various portions of each spectrum. These results show that the low-energy continuum (below 1.0 MeV), which is attributable to scattering in the source and housing, comprises approximately 25 % of the total fluence. The remainder of the fluence is nearly equally split between the two primary ^{60}Co emissions, with the 1.17 MeV fluence being slightly larger.

6.4.2 Average energy

For each calculated and measured spectrum, the fluence-weighted average energy, E_{av}, was determined according to

$$E_{\mathrm{av}} = \frac{\sum\limits_{i=1}^{i_{max}} E_i \cdot \Phi\left(E_i\right)}{\sum\limits_{i=1}^{i_{max}} \Phi\left(E_i\right)}, \tag{6.1}$$

where E_i is the average energy, and $\Phi\left(E_i\right)$ is the fluence, for the spectroscopic bin i. Table 6.5 presents these results. For the MC-generated spectra, the mean average energy of

Table 6.4: Relative percentages of the total fluence for a (10 x 10) cm^2 field from the T1000 system that came from the portions of the spectrum that were below 1.0 MeV, between (1.0 and 1.25) MeV, and above 1.25 MeV. The “Parameters” column indicates the source density and height for the MC spectra and the angle of measurement for the measured spectra.

		Relative fluence (%)		
Method of spectrum determination	Parameters	Below 1.0 MeV	(1.0 to 1.25) MeV (i.e., 1.17 MeV peak)	Above 1.25 MeV (i.e., 1.33 MeV peak)
MC	$5.7\,\mathrm{g \cdot cm^{-3}}$; 1.5 cm	25.8	38.5	35.7
	$5.7\,\mathrm{g \cdot cm^{-3}}$; 2.0 cm	26.2	38.5	35.3
	$5.7\,\mathrm{g \cdot cm^{-3}}$; 2.5 cm	26.4	38.6	35.0
	$5.8\,\mathrm{g \cdot cm^{-3}}$; 1.5 cm	25.9	38.5	35.6
	$5.8\,\mathrm{g \cdot cm^{-3}}$; 2.0 cm	26.4	38.4	35.2
	$5.8\,\mathrm{g \cdot cm^{-3}}$; 2.5 cm	26.6	38.5	34.9
	$5.9\,\mathrm{g \cdot cm^{-3}}$; 1.5 cm	26.0	38.4	35.6
	$5.9\,\mathrm{g \cdot cm^{-3}}$; 2.0 cm	26.6	38.3	35.1
	$5.9\,\mathrm{g \cdot cm^{-3}}$; 2.5 cm	26.8	38.4	34.8
Measurement	22.8°	25.7	39.1	35.2
	31.3°	23.8	39.9	36.3
	48.1°	19.2	41.0	39.8
	70.1°	5.0	47.6	47.4

Table 6.5: Fluence-weighted average energies for the spectra from the T1000 unit that were determined using MC and measurement methods. The "Parameters" column indicates the source density and height for the MC spectra and the angle of measurement for the measured spectra.

Method of spectrum determination	Parameters	E_{av} (MeV)
MC	$5.7\,\text{g}\cdot\text{cm}^{-3}$; 1.5 cm	1.051
	$5.7\,\text{g}\cdot\text{cm}^{-3}$; 2.0 cm	1.051
	$5.7\,\text{g}\cdot\text{cm}^{-3}$; 2.5 cm	1.053
	$5.8\,\text{g}\cdot\text{cm}^{-3}$; 1.5 cm	1.050
	$5.8\,\text{g}\cdot\text{cm}^{-3}$; 2.0 cm	1.050
	$5.8\,\text{g}\cdot\text{cm}^{-3}$; 2.5 cm	1.051
	$5.9\,\text{g}\cdot\text{cm}^{-3}$; 1.5 cm	1.049
	$5.9\,\text{g}\cdot\text{cm}^{-3}$; 2.0 cm	1.049
	$5.9\,\text{g}\cdot\text{cm}^{-3}$; 2.5 cm	1.050
Measurement	22.8°	1.035
	31.3°	1.047
	48.1°	1.052
	70.1°	1.132

the spectrum was 1.050 MeV with a standard deviation of 0.133 % across all density and source height combinations. Thus, E_{av} was not sensitive to changes in source parameters for the MC-generated spectra. For the measured spectra, the mean average energy of the spectrum was 1.067 MeV $\pm\,4.1\,\%$ (including the 70.1° measurement) and 1.045 MeV $\pm 0.9\,\%$ (excluding the 70.1° measurement). Each of the spectroscopic determinations led to E_{av} values that were a few hundred keV below the commonly assumed average encapsulated ^{60}Co energy of 1.25 MeV.

Chapter 7

Characterization of the Varian Clinac iX 6 MV spectrum

This work involved the determination of the spectrum from a Varian Clinac iX linear accelerator that was installed at the University of Wisconsin Carbone Cancer Center (UWCCC). The following sections discuss the specifications of the system and the spectroscopic characterization that was performed using Monte Carlo (MC) simulations and measurements.

7.1 System description

The Varian Clinac iX linear accelerator at the UWCCC produced both (6 and 10) MV photon beams. These high-energy bremsstrahlung beams were produced using accelerated electrons that interacted in a two-layer button-style target made of tungsten and copper. The majority of the bremsstrahlung photons were produced in the tungsten layer while the copper provided fast heat dissipation. The primary collimation for the system was provided by an immobile conical tungsten aperture. Situated below the primary collimator, an energy-specific flattening filter was used to produce a flat radiation field at a depth of 10 cm in a water phantom. Secondary collimation was provided by two sets of layered tungsten jaws that moved in opposite directions from one another. In addition, this system was equipped with a set of multi-leaf collimators (MLCs) that was housed directly below the bottom set of jaws.

7.2 Monte Carlo methods

Monte Carlo (MC) investigations of the 6 MV beam from the Clinac iX were performed using the Monte Carlo N-Particle (MCNP5) code with coupled photon and electron transport. Simulations of percentage depth-dose (PDD) and cross-beam profiles were used to benchmark the MC model against measurements. In addition, the model was used to perform spectroscopic characterizations of the system for a variety of source model parameters.

7.2.1 Geometry of the Clinac iX

7.2.1.1 Verification simulations

The PDD and cross-beam profiles were simulated for a range of field sizes in a model of a (50 x 50 x 50) cm^3 water tank. For these simulations, the *F8 energy deposition tally was used to score the energy deposited in water along the central axis and across the field. Both the PDD and cross-beam profiles were scored in a lattice geometry. The voxel size was (2.5 x 2.5 x 0.5) cm^3 for the PDD calculations and (2.5 x 0.25 x 0.5) cm^3 for the cross-beam profile calculations.

The variance reduction techniques used for these calculations were energy cutoffs, geometry splitting and Russian roulette. A global energy cutoff of 10 keV was used for photons. The electron energy cutoff was 500 keV in all cells of the problem except for the water tank, in which it was 250 keV. Geometry splitting and Russian roulette were used to increase the number of particles in important cells in the problem and kill particles in less important cells.

7.2.1.2 Verification measurements

Measurements of PDD and cross-beam profiles were used to benchmark the MC model of the Clinac iX system. PDD measurements were performed using a Farmer-type Exradin A12 ionization chamber (Standard Imaging, Middleton, WI) and a MAX-4000 electrometer with an applied collecting-electrode bias of +300 V (i.e., negative charge collection). Measurements were completed in a water tank that provided one-dimensional chamber translation with a source-to-surface distance of 100 cm. Measurements were performed for field sizes ranging from (4 x 4) cm^2 to (20 x 20) cm^2 at the surface of the water tank. Data were acquired along the central axis for depths between (0 and 25) cm with step sizes of 0.2 cm from (0 to 2) cm depth, 0.5 cm from (2 to 20) cm depth, and 1 cm for (20 to 25) cm depth. The data were shifted to shallower depths by 0.183 cm to account for the difference between the depth of the central electrode and the effective point of measurement (Almond et al., 1999). All data sets were normalized at a depth of 10 cm.

Cross-beam dose profiles were measured using Kodak X-Omat V radiographic film (Carestream Health, Inc., Rochester, NY). The films were processed using an SRX-101A developing system (Konica Minolta, Tokyo, Japan) and were scanned using an Epson® Expression® 10000 XL flatbed document scanner (Epson America, Long Beach, CA). For all irradiations, the field edges were defined by the jaws with the MLCs retracted. Prior to profile measurements, five films were irradiated to generate a sensitometric response curve that related the film's digitized pixel values to dose. For these irradiations, the films were sandwiched between two 5 cm-thick slabs of Virtual Water™ (VW). The slabs of VW were secured together with tape to minimize air gaps between the film and VW. The phantom was oriented such that the plane of the film was centered on and parallel with the central axis of the beam. The surface of the phantom was positioned 100 cm from the source. The 6 MV photon beam was used to irradiate the films with doses of (10, 20, 30, 40, and 50) cGy at a depth of 5 cm. Using the PDD data from the UWCCC, the corresponding doses at a depth of 10 cm were calculated to be (7.75, 15.5, 23.2, 31.0, and 38.7) cGy, respectively. After developing and scanning the films, ImageJ (National Institutes of Health, Bethesda, MD) was used to determine the pixel value that corresponded to each of these ten doses. A macro that performed logarithmic interpolation on these data was written using Microsoft Excel Visual Basic for Applications. This program was used to determine the dose for each pixel in subsequent profile measurements.

Profiles were measured for field sizes ranging from (5 x 5) cm^2 to (20 x 20) cm^2 at depths of (5 and 10) cm in a VW phantom with a source-to-surface distance of 100 cm. The phantom consisted of four slabs of 5 cm-thick VW. For each profile measurement, a piece of film was placed between two slabs in the phantom, resulting in a minimum of 10 cm of VW backscatter material. Following processing and scanning, a 15 pixel-wide region-of-interest across the center of each profile was analyzed and converted to dose profiles using the interpolation program. The profiles were normalized to the average dose value between ±1 cm from the central axis.

7.2.1.3 Beam-line model

A detailed model of the Varian Clinac iX linac was created using MCNP5. The MC model in this work was created specifically for the 6 MV photon beam. The geometric specifications used in the model were determined from technical drawings included in the *Monte Carlo Data Package: High Energy Accelerator* document from Varian Medical Systems. The MC model included the components that influenced the production (i.e., target), shaping (i.e., primary collimator, flattening filter, jaws), and monitoring (i.e., ionization chamber, field mirror) of the photon beam. The components that were not modeled (e.g., iron structural and shielding components, electronics and motors, and retracted MLCs) were omitted because they were not expected to substantially affect the central-axis spectrum. A Visual Editor (VisEd) rendering of the model is shown in Figure 7.1.

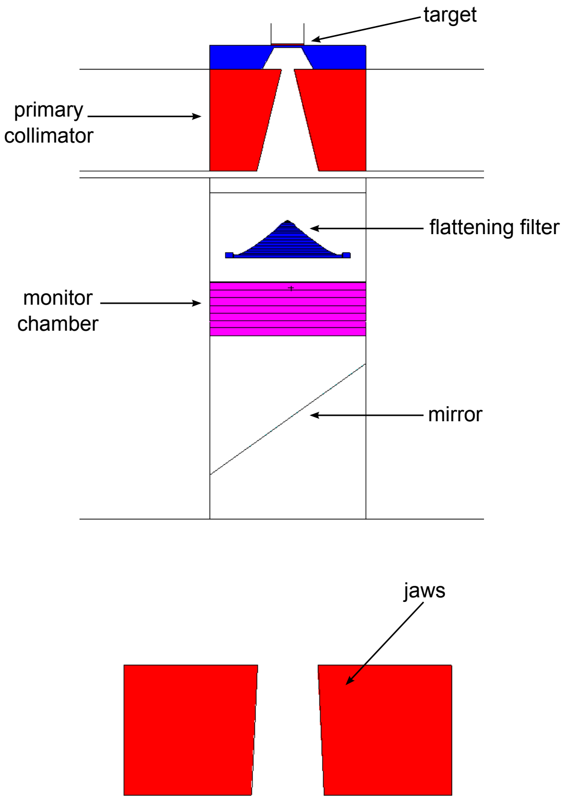

Figure 7.1: VisEd rendering of the Varian Clinac iX. This cross section features only one set of jaws.

The Varian MC package, which contained specifications about the physical structures in the unit, did not include information about the primary electron beam. The electron source parameters, including spatial spread; energy spread; and mean electron energy, were determined from comparisons of simulated and measured PDD and cross-beam profiles.

Sensitivity studies According to the work of Chibani et al. (2011), the average energy of a primary electron beam is best found by matching simulated and measured PDDs for a small field size. In addition, the radial distribution of the primary electron beam can be found by matching simulated and measured profiles for either a small or large field size. For a 6 MV beam, Chibani et al. found that the electron spot size had a negligible effect on PDD and vice versa. Thus, for this work, the mean electron energy was determined by comparisons with PDD, and the source size was determined by comparisons with the cross-beam profile.

A sensitivity study was performed to determine the appropriate mean energy, E_{av}, of the primary electron beam that gave simulation results in agreement with measurements for a (4 x 4) cm^2 field. PDD simulations were performed for E_{av} of (5.9, 6.0, 6.1, 6.2, and 6.3) MeV with a Gaussian energy spread of 3 % at the full-width-at-half-maximum (FWHM). For these simulations, the spatial distribution of the electron source was Gaussian in the x- and y-directions with a FWHM, D, of 0.14 cm. In addition, the divergence, θ, of the primary electron beam was 0.0°. The results of these simulations are shown in Figure 7.2a, and their comparisons with measurements are shown in Figure 7.2b. The shallow portions of the PDD curves indicate a decrease in relative dose with increasing energy, as was expected. The impact of this trend is reflected in Figure 7.2b for depths shallower than the normalization depth of 10 cm. For E_{av} less than 6.0 MeV, the MC simulations overpredicted PDD, and for E_{av} greater than 6.1 MeV, the simulations underpredicted PDD. Beyond the normalization depth, it is challenging to determine the impact of E_{av} based on the PDDs alone; however, the percentage differences shown in Figure 7.2b indicate that energies below 6.0 MeV underpredicted PDD while energies above 6.0 MeV overpredicted PDD.

A sensitivity study was also performed to determine the appropriate spot size for the 6 MV beam. Cross-beam profile simulations were performed for a (5 x 5) cm^2 field with a source that was Gaussian in the x- and y-directions with D of (0.08, 0.10, 0.12, 0.14, and 0.16) cm. For these simulations, the average energy of the source was 6.0 MeV and the divergence was 0.0°. The results of these simulations are shown in Figure 7.3. The profiles indicate that the (5 x 5) cm^2 profile for the 6 MV photon beam is relatively insensitive to changes in the FWHM of the primary electron beam.

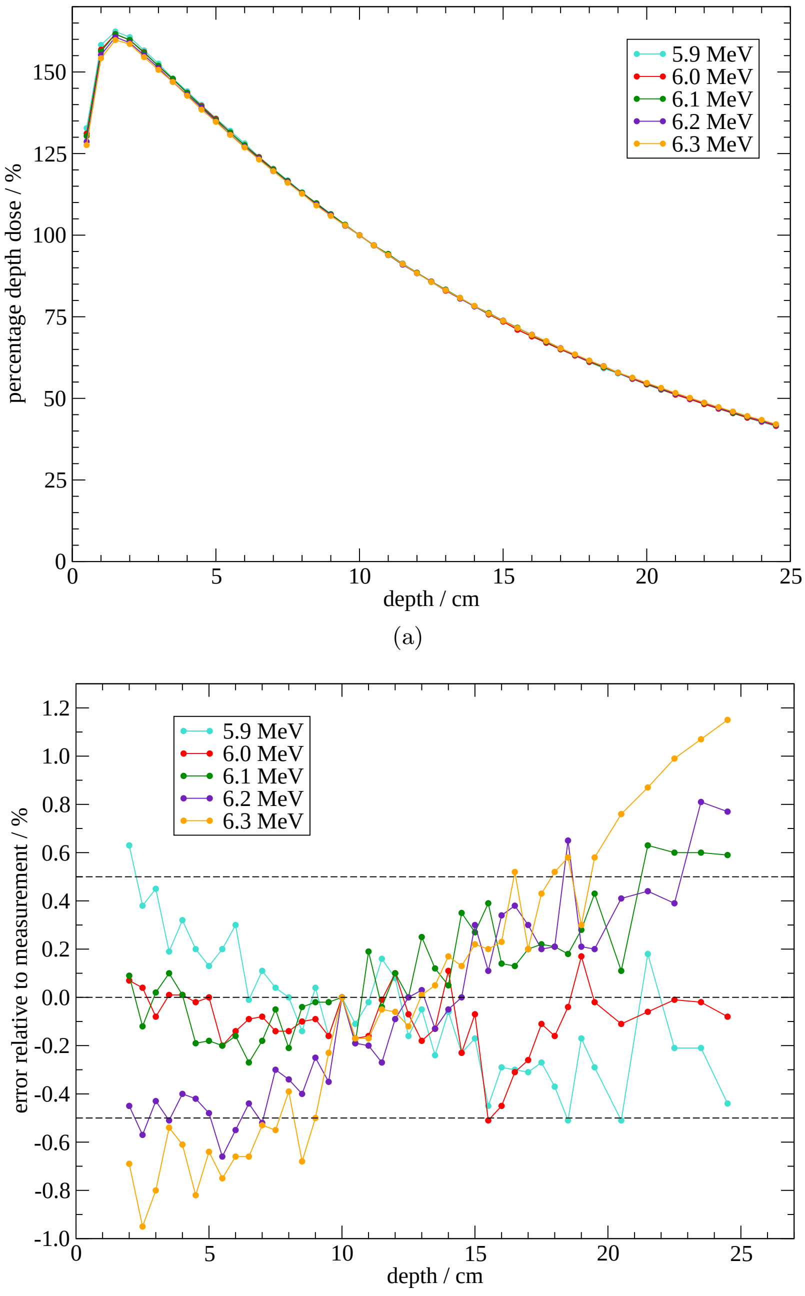

(a)

(b)

Figure 7.2: (a) Calculated PDDs for variations in the mean energy, E_{av}, of the primary electron beam for a 6 MV linac beam, and (b) the percentage error between calculated and measured PDD values. These data correspond to the (4 x 4) cm^2 field.

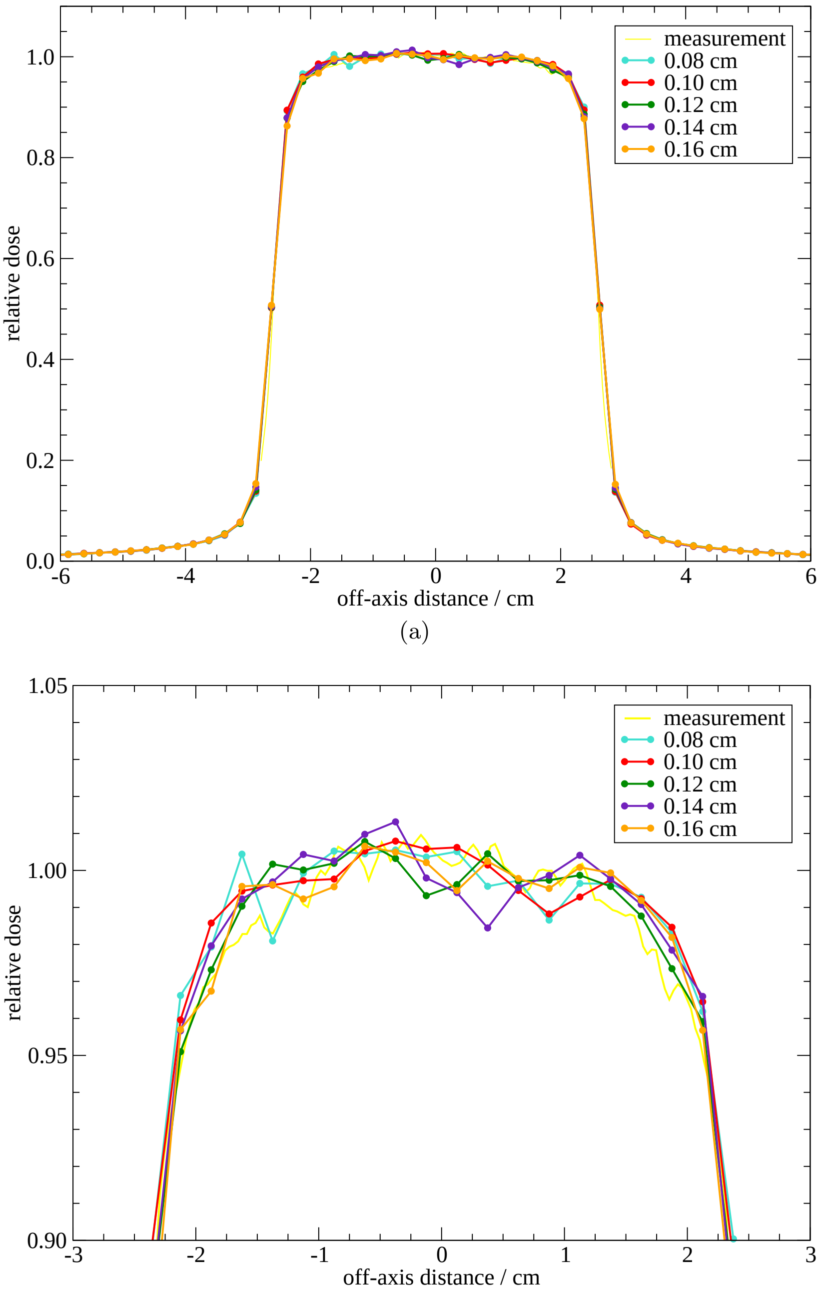

(a)

(b)

Figure 7.3: Calculated and measured profiles for variations in the FWHM of the primary electron beam for the (5 x 5) cm^2 field of a 6 MV photon beam. (a) shows the full profiles, and (b) shows a magnified view of the flat portion of the profiles.

Final parameters The 6.0 MeV simulation yielded PDDs within ±0.5 % of the values determined with the Exradin A12 chamber at all depths. Based on these findings, the final E_{av} was determined to be 6.0 MeV. The profiles did not show a strong dependence on FWHM; however, the profile with a FWHM of 0.12 cm showed the best agreement with the measurement in the shoulder region. Thus, the final primary electron beam spot size was Gaussian with a FWHM of 0.12 cm.

7.2.2 Spectra determination

The effects of the primary electron beam parameters (mean energy, spatial spread, and divergence) on the spectrum were determined for simulations in which the parameters were varied one at a time around the final solution of $E_{\mathrm{av}} = 6.0\,\mathrm{MeV}$, $D = 0.12\,\mathrm{cm}$, and $\theta = 0.0°$. The specific parameters that were tested were E_{av} of (5.9, 6.0, 6.1, 6.2, and 6.3) MeV, D of (0.08, 0.10, 0.12, 0.14, and 0.16) cm, and θ of 0.0°, 0.5°, and 1.0°. For the divergence sensitivity study, the primary electron source was modeled as a mathematically collimated point source that was positioned at a distance, d, above the target such that the maximum off-axis distance of an incident electron was 0.06 cm (see Figure 7.4). For all simulations, in-vacuum spectra were calculated using the F4 cell-based fluence tally in cylindrical rings with radii of (5, 10, 15, and 20) cm. The tally rings were positioned a distance of 100 cm from the source. To isolate the effects of the primary electron beam and stationary primary collimation system, the jaws were not included in these simulations. Each spectrum was normalized to its total fluence.

The shape of the spectrum was affected by changes in E_{av} at all off-axis distances that were investigated, as shown in Figure 7.5. The effect of E_{av} can be viewed best in the magnified spectra shown in Figure 7.5b. These spectra indicate that the relative number of low-energy photons decreased with larger E_{av}. Furthermore, the maximum energy of the spectrum increased with E_{av}.

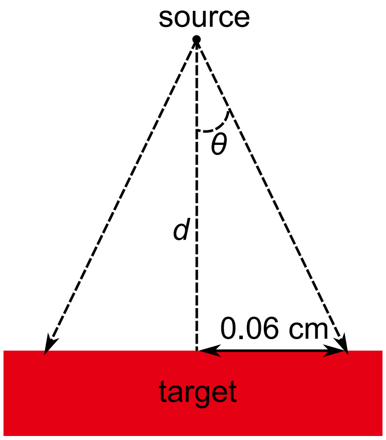

Figure 7.4: Diagram illustrating the source geometry that was used for the divergence spectrum-sensitivity test. The source was modeled as a mathematically collimated point source that emitted photons in a cone with a half angle, θ, of 0.0°, 0.5°, or 1.0°. The point source was positioned at a distance, d, above the target so that the maximum off-axis distance of an incident electron was 0.06 cm.

The spectra that were found for changes in D are shown in Figure 7.6. These spectra indicate that the shape of the spectrum was affected by changes in the size of the primary electron beam, but only for the off-axis spectra with large radii (i.e., [15 and 20] cm). Specifically, the relative number of low-energy photons decreased with larger values of D. This indicates that the average energy of the off-axis spectrum increased slightly with the size of the primary electron beam.

Of the three parameters that were tested, the 6 MV spectrum was least sensitive to changes in the divergence of the primary electron beam. Figure 7.7 shows the spectra that were calculated for the various divergences that were tested. These spectra show that only the off-axis spectrum for the 20 cm-diameter ring was affected by a divergence of 1.0°. The magnified low-energy portion of the spectrum indicates that the energy of the spectrum decreased slightly with increases in the divergence.

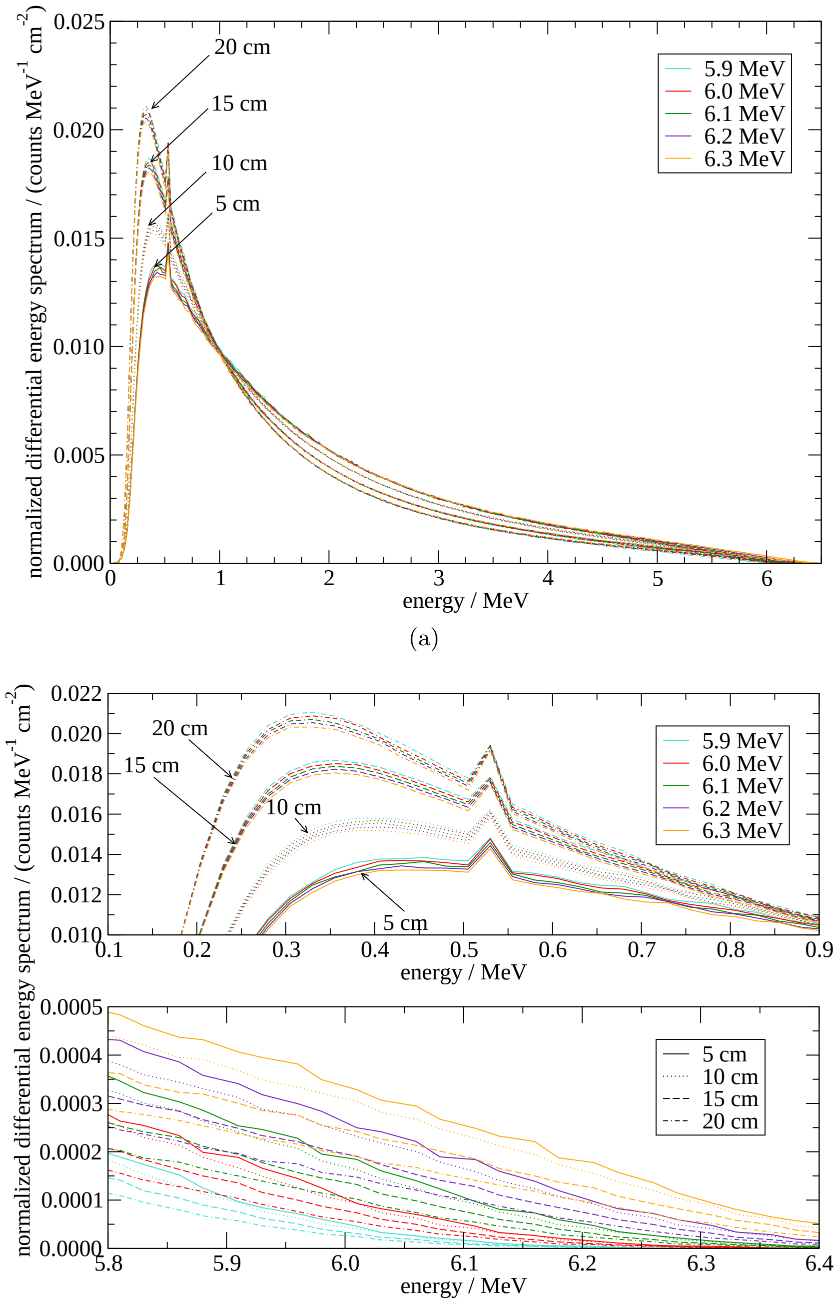

(a)

(b)

Figure 7.5: Calculated spectra for variations in the mean energy, E_{av}, of the primary electron source for a 6 MV beam from the Clinac iX. (a) shows the whole spectrum, and (b) shows magnified views of the low- and high-energy regions.

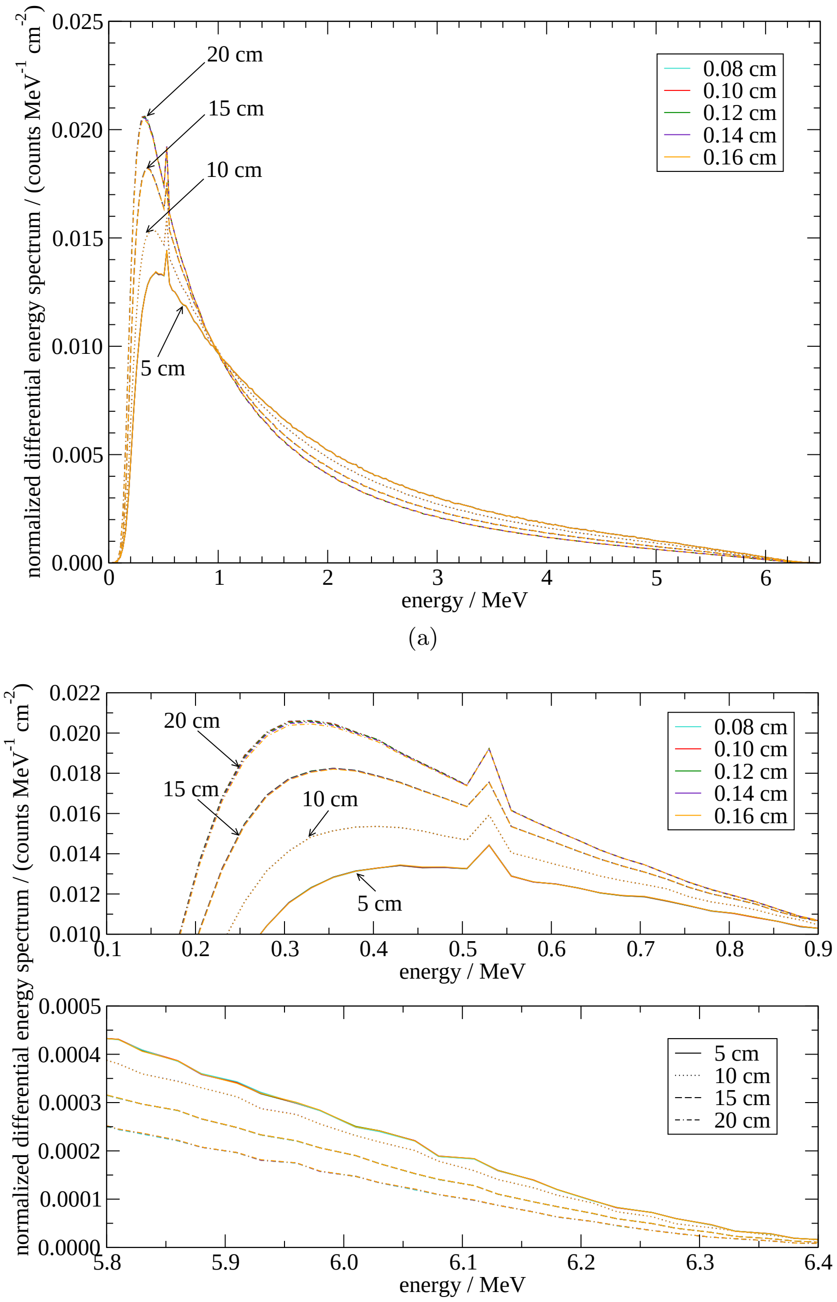

(a)

(b)

Figure 7.6: Calculated spectra for variations in FWHM of the primary electron source for the 6 MV beam from the Clinac iX. (a) shows the whole spectrum, and (b) shows magnified views of the low- and high-energy regions.

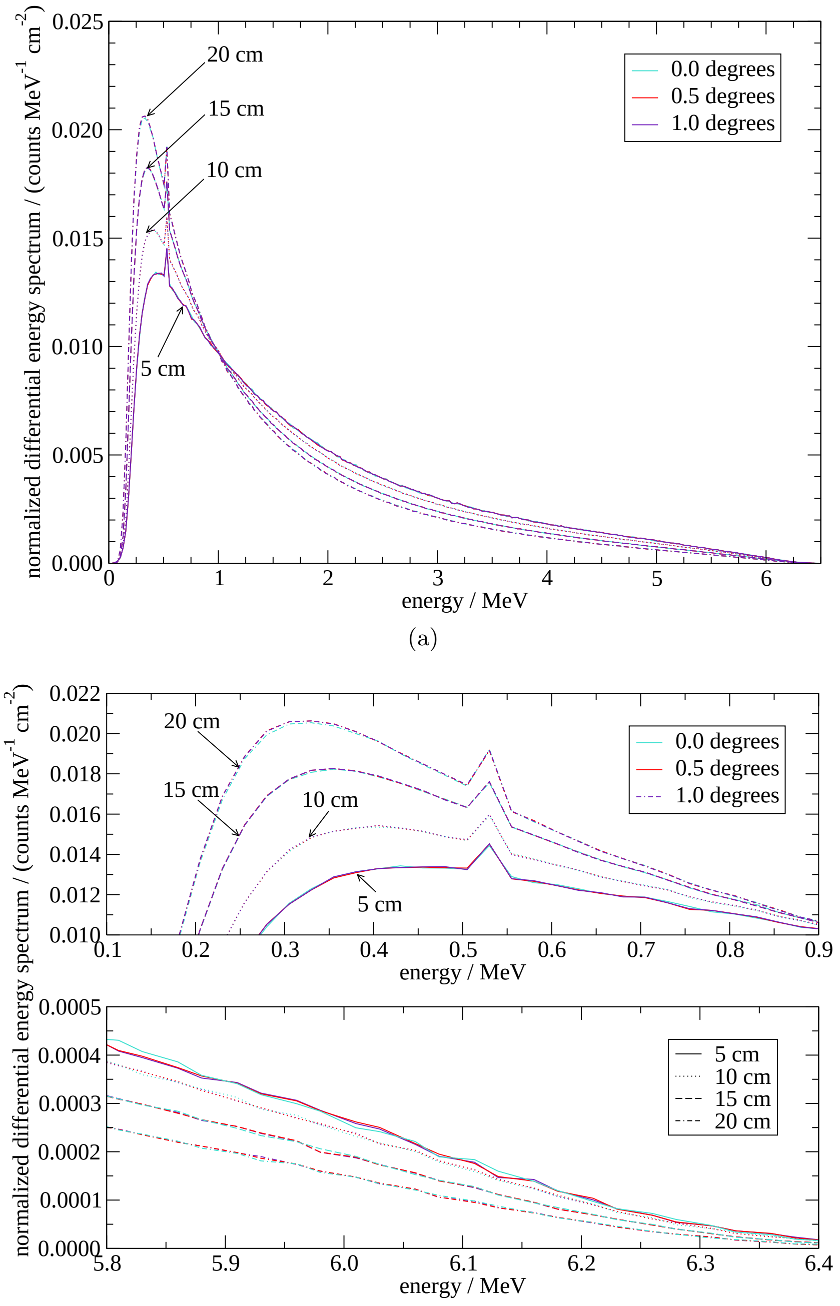

(a)

(b)

Figure 7.7: Calculated spectra for variations in the primary electron source divergence for the 6 MV beam from the Clinac iX. (a) shows the whole spectrum, and (b) shows magnified views of the low-energy region.

7.3 Measurement methods

The spectrum of the 6 MV beam was characterized using Compton-scattering (CS) measurements, as well. The following section discusses the measurement techniques that were used and the resulting spectra that were determined.

7.3.1 Compton spectrometry setups

The central-axis photon spectrum was measured for a (10 x 10) cm^2 field using a CS measurement arrangement with a scattering angle of 35°. This angle was selected so that the maximum energy of the scattered photons was near 2 MeV. This measurement was performed using a 3.0 cm-diameter aluminum scattering rod that was placed at isocenter. The scatterer-to-detector distance was approximately 280 cm. Figure 7.8 shows a photograph of the CS spectrometry system that was used for this measurement. An additional 20 cm of lead, which is not shown in Figure 7.8, was placed in front of the detector shield to attenuate linac leakage. This additional shield was built from lead bricks and had an opening to allow the CS photons to reach the collimating aperture.

The basic electronics components that were used for these measurements were discussed in Section 4.2.1.1. The fast-spectroscopy linear amplifier was operated with a shaping time of $4\,\mu$s, a coarse gain of 100, and a fine gain of 0.30. All measurements were performed using the unipolar output from the linear amplifier as well as the pile-up rejection circuit. The pile-up rejector was adjusted at the environmental background level.

The pulse-height distribution (PHD) was acquired for approximately thirty minutes at a linac repetition rate of $600\,\mathrm{MU}\cdot\mathrm{min}^{-1}$. A background measurement was performed for this measurement arrangement, as well. To determine background, the collimator was plugged with a 16 cm-long tungsten rod. An additional 10 cm of lead was placed in front of the collimating aperture. The acquisition time for the background measurement was approximately twenty minutes.

Figure 7.8: Photograph of the CS spectrometry system that was used for spectra measurements of the 6 MV beam from the Varian Clinac iX.

The CS and background measurements were smoothed using a MATLAB-based Savitzky-Golay smoothing filter. This filter was selected because it preserved the shapes of fluorescence peaks that would have otherwise been flattened using different smoothing techniques. The background PHD was scaled to account for the difference in acquisition time from the corresponding CS measurement. Channel-by-channel subtraction was used to correct the CS measurement for background.

7.3.2 Results

Figure 7.9 shows the raw measured PHD which has not been corrected for background or detector response. The PHD featured many peaks, which is uncharacteristic for a megavoltage bremsstrahlung spectrum. These peaks came from lead fluorescence ([72 to 82] keV) and annihilation (511 keV) events in the detector shielding. In addition to the pure fluores-

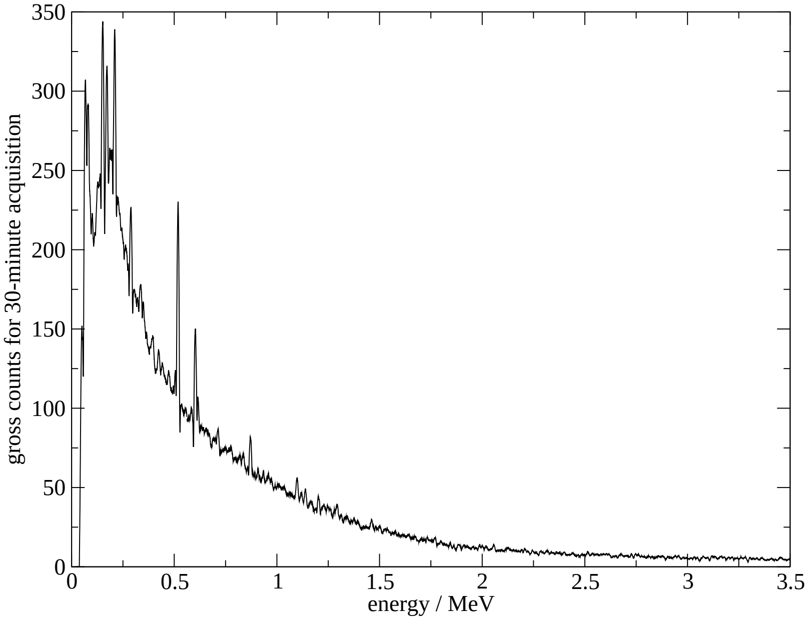

Figure 7.9: Measured PHD for the 6 MV photon beam from the Varian Clinac iX that was performed using CS spectrometry at a scattering angle of 35°. This PHD has not been corrected for background or the CS relations.

cence and annihilation peaks, the spectrum included summation peaks from these events. Summation peaks (or pulse pile-up) occur when a detection system is unable to differentiate between two or more separate energy depositions in the detector, processing them as a single, higher-energy event. In general, the pulse pile-up rate increases with the measured count rate (Gilmore, 2008), and the pile-up rejector is used to prevent the processing of pulses that arrive too close to an original. In this work, the CS process was very efficient at reducing the count rate at the detector, which would indicate that pulse pile-up should not have been a problem; however, as is evident from the summation peaks in Figure 7.9, pulse pile-up was an issue even at this low count rate.

The background-corrected PHD, which has not been corrected for the detector response or CS geometry, is shown in Figure 7.10, with an MC-calculated PHD shown for comparison. This spectrum indicates that the fluorescence, annihilation, and summation peaks were

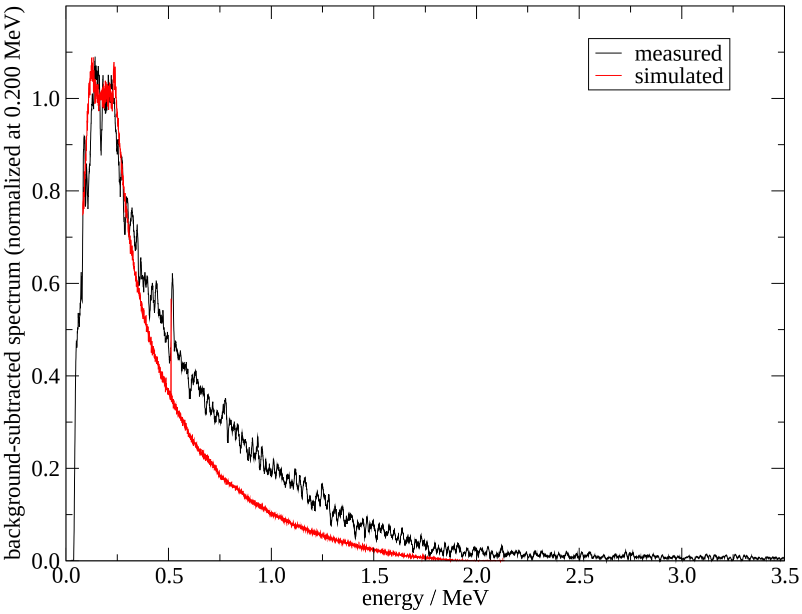

Figure 7.10: Background-corrected measured PHD for the 6 MV photon beam from the Varian Clinac iX that was performed using CS spectrometry for scattering at 35°. This PHD has been corrected for background only. A simulated PHD is shown for comparison.

largely subtracted out when background was accounted for. However, given the scattering angle of 35°, the maximum energy of the 6 MV photon spectrum should be near 2 MeV. As shown in Figure 7.10, the measured background-subtracted PHD included photons above 2 MeV, which indicates that pulse pile-up was not completely accounted for with background subtraction. The MC PHD shows no counts above 2 MeV, as expected. Given this issue, the measured PHD was not corrected for detector response or the CS relations. These preliminary measurements demonstrate that the CS spectrum from a 6 MV field is detectable; however, the high background level indicates that additional shielding is required to improve the signal-to-noise ratio.

7.3.3 Background characterization

The pulse pile-up issues that were addressed in Section 7.3.2 indicated that improvements to the CS measurement system were necessary. The primary problem with the measurement

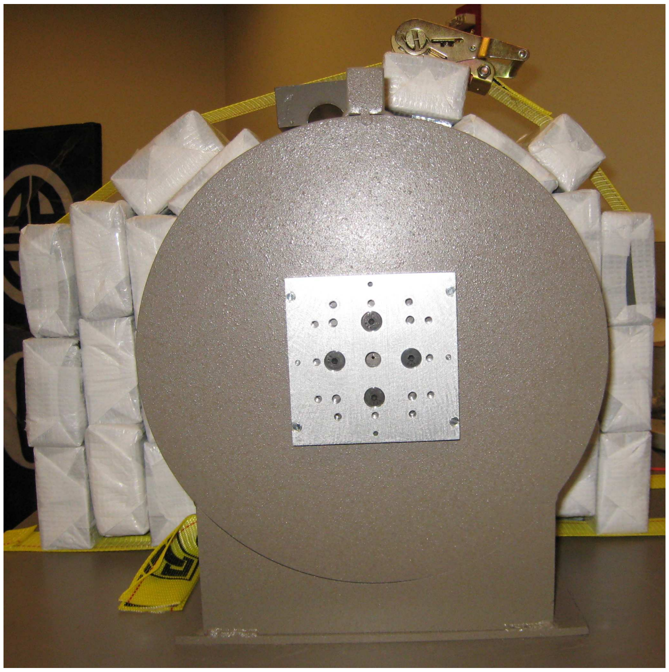

Figure 7.11: Arrangement of extra lead bricks used to reduce the number of background photons reaching the detector for the 6 MV linac spectrum measurements.

system was that too many room-scattered photons were penetrating the detector shield or creating fluorescence or annihilation photons that reached the detector. Thus, the detector shielding was an obvious area that required improvement. Measurements were performed to determine weaknesses in the shielding of the CS measurement system. These measurements were performed using the 6 MV photon beam with CS at 45° from a 3.0 cm-diameter aluminum scattering rod. The same electronics settings that were presented in Section 7.3.1 were used for these measurements.

To determine weaknesses in the detector shield, the count rate was observed as extra lead shielding was added around the existing detector shield and cold finger. PHDs were acquired for approximately 3 minutes for each shielding configuration. For each measurement, additional lead bricks were stacked around the cylindrical shield and held in place with high-load webbing (see Figure 7.11). The count rates for these measurements were not substantially different from one another and, thus, did not reveal an obvious weakness in the shield.

The CS system was further characterized by observing the count rates for the CS spectra and background spectra for field sizes of (3 x 3) cm^2 and (10 x 10) cm^2. The dead times (DT) associated with these measurements were also monitored. These measurements revealed that the count rate from the CS photons increased with field size due to the increased fluence rate from linac collimator scatter. The specific count rates were $269\,\text{counts} \cdot \text{sec}^{-1}$ and $306\,\text{counts} \cdot \text{sec}^{-1}$ for the (3 x 3) cm^2 and (10 x 10) cm^2 fields, respectively. This difference in count rate was reflected in the DT associated with each measurement (1.07 % versus 1.85 %). The background count rates and DTs from these two field sizes were not significantly different. This indicates that the increase in count rate with field size was the result of only the CS photons traveling through the collimating aperture. Therefore, this system should be able to measure differences in spectra for various field sizes.

Chapter 8

Conclusions

8.1 General MCNP5 investigations

8.1.1 Conclusions

This thesis work included three general investigations involving the compatibility and implementation of various techniques available in the Monte Carlo N-Particle (MCNP5) code. The first investigation addressed calculation inaccuracies that result from the improper use of two variance reduction (VR) techniques in MCNP5. It was found that the electron energy cutoff VR technique can impact photon-only problems by reducing the amount of bremsstrahlung photons that are produced. In addition, it was found that the DXTRAN technique produces inaccurate results when used in problems where a cell has an electron importance of zero but a photon importance that is nonzero. The second investigation involved the implementation of Doppler broadening (DB) in MCNP5. It was found that MCNP5 version 1.60 properly uses the DB algorithm for all Compton-scattering (CS) interactions; however, prior to this work, the DB data in the most up-to-date library were presented in an incorrect form for use with the DB algorithm. Following this discovery, a new photon data library was released by Los Alamos National Laboratory. Finally, the production and use of phase-space files (PSFs) was investigated. This work found that PSFs created in MCNP5 include the proper information to accurately represent a phase space; however, inaccurate calculations result from subsequent simulations that run the same number of particles that were used to generate the PSF.

8.1.2 Future work

In general, these investigations showed that, while calculations with MCNP5 are convenient for simulating radiological physics problems, the code itself is imperfect. It is important to isolate and test each technique using a simple simulation prior to applying it to a more complicated simulation. Future work for the particular investigations that were discussed in Chapter 3 should include a more detailed study of PSFs in MCNP5. This study would involve analyzing the source code to find where the problem is introduced. Following the identification of the problem, the code should be updated and benchmarked to demonstrate the usability of PSFs for a variety of simulations.

8.2 General MC and measurement methods

8.2.1 Conclusions

8.2.1.1 Monte Carlo

MC simulations served many purposes in this work. First, they were used to simulate primary photon spectra from the Theratronics T1000 system and Varian Clinac iX linear accelerator. In addition, simulations were used to determine detector response functions (DRFs) that corrected measurements for artifacts introduced by the measurement system. These simulations were critical to the accurate unfolding of measured spectra.

8.2.1.2 Measurements

Measurements in this work were performed using a Compton-scattering (CS) spectrometry arrangement in which a highly collimated, high-purity germanium detector measured photons that were scattered from the central axis by a small aluminum scattering rod. These measurements were performed using a reverse-electrode germanium (REGe) detector that was placed inside a custom-made lead shield. This shield included a graded liner of copper and tin to reduce lead fluorescence contamination. For each CS measurement, an analogous background measurement was performed where the collimating aperture was blocked with tungsten and lead. After accounting for background, each spectrum was unfolded from its measured pulse-height distribution (PHD) using the Gold deconvolution technique. The final conclusions for each of the sources that were investigated are discussed in Sections 8.4 and 8.5.

8.2.2 Future work

8.2.2.1 Monte Carlo

The MC models of the REGe detector and CS geometry were crucial for accurate unfolding of the measured spectra. Future work should include a sensitivity study to determine how changes in the model geometry (e.g., scatterer-to-detector distance, scattering geometry, detector alignment, air composition, etc.) affect measurement corrections. This study would help establish a threshold for required model accuracies. In addition to the MC geometry model, the source model is important for DRF simulations. The representation of the source (i.e., dimensions, secondary sources, etc.) for these DRF simulations should be closely investigated.

8.2.2.2 Measurements

Future measurements should include an optimization study to determine the ideal scattering geometry for the measurement of megavoltage radiation. Although it is possible to correct for many artifacts introduced by an un-optimized measurement system, it is ideal to apply as few corrections as possible to reduce uncertainties. Optimizing the scattering geometry will include identifying a scattering rod material that has a large-enough CS cross section, but exhibits minimal DB. Finally, the ideal dimensions of the scattering rod should be determined, and the arrangement of the CS system components (e.g., scatterer-to-detector distance, scattering angle) should be further investigated.

8.3 Verification of the CS spectrometry technique

8.3.1 Conclusions

8.3.1.1 Monte Carlo

The viability of the CS spectrometry technique was demonstrated using MC investigations that simulated the measurement of a 6 MV linear accelerator field. These simulations included a full model of the REGe detector, shield, and scattering rod, all of which were placed inside of a concrete treatment vault. Simulations were performed to determine the relative signals coming from both primary and secondary sources. These simulations showed that the intended signal was four orders of magnitude larger than any other signal.

8.3.1.2 Measurements

The CS spectrometry technique was also demonstrated with spectroscopic measurements of a high dose rate ^{192}Ir source. These measurements were performed using the REGe detector and a large-diameter collimating aperture. Measurements were performed at multiple scattering angles and were corrected using a conventional DRF. The measurements showed that the energies of the CS peaks decreased with increasing scattering angle. The positions of the peaks were corrected to the appropriate energies using the equations for the CS relations.

8.3.2 Future work

8.3.2.1 Monte Carlo

Although the most likely background sources were carefully accounted for, the MC simulations in this work did not model the full CS measurement. Therefore, these simulations could have neglected important sources of background. A full model of the CS measurement, including the linac vault and all sources of room scatter, would require the use of advanced variance reduction techniques. These simulations could be facilitated by the use of DXTRAN spheres and the exponential transform technique. With updates to the geometry, this model could also be used to identify weaknesses in the detector shield design. The current model of the detector and detector shield does not account for the liquid nitrogen dewar or vertical dipstick passing through the detector shield. These potential pathways for room-scattered photons could be investigated with a more complete model of the CS system.

8.3.2.2 Measurements

The purpose of the ^{192}Ir measurements was to demonstrate the practical use of the CS technique. While this goal was accomplished, these measurements exhibited broad peaks, some of which were not resolvable from one another. Future work could include improving the CS measurement system to determine a more precise spectrum. Improvements to the CS measurement geometry would allow for the measurement of spectra at various azimuthal and polar angles as well. These spectra measurements could be compared to MC-generated spectra. In addition, they could be used to determine the spectroscopic air-kerma strength of the source.

8.4 T1000 ^{60}Co teletherapy system characterization

8.4.1 Conclusions

This thesis work investigated the spectroscopic characterization of a therapy-level ^{60}Co unit using MC and measurement methods. An MC model of the Theratronics T1000 ^{60}Co unit was created with the MCNP5 MC code. This model was benchmarked by comparing simulated and measured percentage depth-dose (PDD) curves and cross-beam profiles. The model was then adjusted to determine how sensitive the PDD and spectrum were to changes in the density and height of the source model. The results of these simulations indicated that the PDD does not appreciably change as a function of these parameters; however, the shape of the spectrum is substantially affected.

Measurements of the T1000 spectrum were performed at four different scattering angles using the CS spectrometry technique. This demonstrated that the proposed measurement corrections could appropriately correct a measurement made at any angle. A background measurement was performed for each of these four measurement systems and was removed using channel-by-channel subtraction.

The scattered spectra demonstrated that the centroid energies of the ^{60}Co peaks decreased with increasing scattering angle as predicted by the conservation of energy and momentum. The measurements were then corrected using measurement-specific DRFs that accounted for interactions in the detector and shield as well as the CS relations (e.g., kinematic relations, Klein-Nishina relationship, DB). The spectrum was unfolded from each measured PHD using the Gold deconvolution technique. This technique was used by Davis (2009) to unfold a kilovoltage bremsstrahlung spectrum and by Beach (2005; 2007) and Moga (2011) to unfold low-energy brachytherapy seed spectra. Using this technique, the primary ^{60}Co emissions for each of the spectra were corrected to the proper energies. Furthermore, with the exception of the 70.1° measurement, there was good agreement in the shape of the low-energy region of the spectrum.

The MC-generated and measured spectra were compared in terms of average energy and the relative areas under three regions of the spectrum. The average spectrum energy (excluding the 70.1° measurement) was 1.045 MeV. Furthermore, it was found that approximately 25 % of the spectrum comes from scattered photons below 1 MeV.

8.4.2 Future work

8.4.2.1 Detector response

In this work, the DRF for the 70.1° CS measurement over-corrected the low-energy region. Future investigations of the T1000 ^{60}Co system should determine how accurately the CS system must be modeled for accurate spectrum unfolding. This investigation will include determination of an appropriate source model for DRF calculations. In this work, the source model for the DRF calculations was cylindrical and mimicked the shape and size of the encapsulated ^{60}Co source; however, no materials or collimators were used for these simulations. As demonstrated in Figure 6.6, a substantial portion of the low-energy scatter region was generated from interactions in the source housing and primary and secondary collimators. Because the DRF did not account for these components, the corrections that were applied may not have accurately represented this region. This should be investigated using a complete source model for the DRF simulations.

8.4.2.2 Spectra comparisons

The spectra comparisons made in this work were generated from relative spectra. Future work should address the use of absolute spectra for dosimetric comparisons. For MC simulations, this will involve scaling the simulated spectra using a “dose pair” (Smilowitz, 2002), which is the ratio of measured and simulated dose rates. For the measured spectra, this will involve verifying the accuracy of the DRF corrections. Specifically, the efficiency of the detector, the fluence rate reduction due to CS, and air attenuation will need to be verified for the model. Following the determination of absolute spectra, the spectroscopic air-kerma rate and dose rate should be found. These spectroscopic values can then be compared to values measured with ionization chambers.

Another study should investigate the dosimetric implications of the encapsulated ^{60}Co spectrum. MC studies in the literature often model encapsulated ^{60}Co sources using equiprobable (1.17 and 1.33) MeV photons or 1.25 MeV photons. The impact that the degraded spectrum has on dose distributions in water and in heterogeneous media should be investigated.

8.4.2.3 Spectra determinations

This work performed spectroscopic characterizations for the central axis of a (10 x 10) cm^2 field. Future work should include simulations and measurements of both central-axis and off-axis spectra for other field sizes. The central-axis spectra from these simulations could be compared to the MC-determined spectra from Mora (1999), Smilowitz (2002), and Tedgren et al. (2010). In addition, these spectra could be used to determine spectroscopic output factors. Off-axis spectra would be useful for studying how spectroscopic variations across the field influence dose distributions and energy response for dosimeters.

8.5 6 MV Clinac iX system characterization

8.5.1 Conclusions

This work explored MC- and measurement-based methods for obtaining the spectrum of a 6 MV linear accelerator field. A model of the 6 MV beam from a Varian Clinac iX linear accelerator was developed in MCNP5 and benchmarked using measurements of PDD and cross-beam profiles. Using this model, MC simulations were performed to determine the in-vacuum spectrum at several off-axis distances for various values of the mean energy, spatial distribution, and divergence of the primary electron beam. The spectrum was found to be sensitive to changes in the mean electron energy; however, it was relatively insensitive to changes in the spot size and divergence. Only the far off-axis spectra were changed by these parameters.

Measurements of the 6 MV beam were also performed. A CS measurement setup was used to measure the spectrum of a (10 x 10) cm^2 field that was scattered at 35° relative to the central axis. It was observed that the measured spectrum (prior to background subtraction) included fluorescence and annihilation peaks from interactions in the detector shield. After performing background subtraction, these peaks were largely accounted for; however, even after background subtraction, counts appeared in the PHD at higher energies than expected, indicating that pulse pile-up was a problem. Due to the pulse pile-up issues, efforts were made to reduce the background count rate by adding more lead shielding around the detector. The count rate and dead time were monitored as lead bricks were placed around various portions of the detector shield; however, no obvious weaknesses were found. In addition, the count rate and dead time were monitored for CS spectra from different field sizes. The results of this study showed that the CS count rate increased with field size, but the background count rate did not.

8.5.2 Future work

This work has demonstrated that the 6 MV linac spectrum is detectable above background when used with the CS technique; however, improvements to the measurement system are required for a definitive determination of the spectrum.

8.5.2.1 Shielding

The primary focus of future work should be to isolate and eliminate the sources of background that are contaminating the CS measurements. With reduced background, pulse pile-up due to fluorescence and annihilation photons should no longer be an issue. There are a few parts of the detector shield that should be considered for improvement. First, the copper and tin layers on the graded liner could be made thicker to attenuate more lead fluorescence photons. In addition, the liquid nitrogen dewar and the neck of the detector could be more carefully shielded. These poorly shielded areas could be easy pathways for room-scattered photons to reach the detector. As an alternative to adding shielding around the detector, a shielding wall could be built between the source and detector. The measurements performed in this work were done in an off-site facility. Because all measurement equipment needed to be mobile, the amount of shielding that could be used was limited. If future measurements are performed using the clinical linear accelerator that the UWMRRC is commissioning, a substantial shielding structure could be built on-site. Finally, if the pulse pile-up problem cannot be resolved experimentally, it could be accounted for using statistical models based on the differences between the MC-generated and measured PHDs.

8.5.2.2 Spectra measurements

Once the detector has been appropriately shielded, measurements with the CS technique should be relatively straightforward. Studies could be performed to determine how the central-axis spectrum varies as a function of dose rate, field size, and field shape. In addition, off-axis spectra could be measured.

8.5.2.3 Spectra comparisons

Many comparisons could be performed with these simulated and measured spectra. First, a comparison should be performed to investigate how the measured spectra compare with the spectra assumed by treatment planning systems. This study could include a comparison of the dosimetric effects of the various measured and assumed spectra when used with the treatment planning system. In addition, these spectra could be used to calculate conventional and nonstandard beam quality conversion factors for reference dosimetry. Finally, these spectra could be used to calculate measurement-based phantom-independent calibration factors to complement the work of Smilowitz (2002).

8.6 Concluding remarks

The energy spectrum is important for dosimetry and accurate treatment planning with megavoltage external beam photon sources. Currently, the most common method of spectrum determination provides only an estimate of the photon spectrum. This dissertation work has demonstrated two more-direct methods of spectrum characterization. In addition, it has introduced a novel measurement correction methodology. The results of this work support the potential for high-energy and high fluence rate spectrometry, which could eventually shift the approach to megavoltage photon dosimetry and reduce the uncertainty of dose calculations with model-based treatment planning systems.

Appendix A

Calculating scattering angle windows

This appendix derives the equations that were used to calculate the minimum and maximum scattering angles, $\theta_{\min}$ and $\theta_{\max}$, that were accepted by the detector in CS spectrometry measurements. The explanation in this section was adapted from the work of Matscheko and Carlsson (1989). For these calculations, the origin of the coordinate system is centered in the scattering rod, as shown in Figure A.1. The calculations in this section assume the following definitions for the vectors and variables that specify the CS system geometry:

$\overrightarrow{r_f}$ describes where the photon was emitted from the source,

$\overrightarrow{r_\theta}$ describes where the scattering event takes place,

$\overrightarrow{r_d}$ describes where the photon enters the detector,

f is the diameter of the source,

r is the radius of the scattering rod,

L is the length of the scattering rod,

d is the diameter of the collimating aperture,

F is the distance from the point of emission to the point of interaction,

D is the distance from the point of interaction to the point of detection,

λ is the angle between the x axis and $\overrightarrow{r_\theta}$ for θ_{min}, and

α is the angle between the x axis and $\overrightarrow{r_\theta}$ for θ_{max}.

Any scattering angle, θ, can be derived from the dot product of $(\overrightarrow{r_\theta} - \overrightarrow{r_f})$ and $(\overrightarrow{r_d} - \overrightarrow{r_\theta})$ by

$$\theta = \arccos\left(\frac{(\overrightarrow{r_\theta} - \overrightarrow{r_f}) \cdot (\overrightarrow{r_d} - \overrightarrow{r_\theta})}{|\overrightarrow{r_\theta} - \overrightarrow{r_f}||\overrightarrow{r_d} - \overrightarrow{r_\theta}|}\right).$$

For CS measurements from a cylindrical rod, θ_{min} and θ_{max} are found for scattering events on the rod's surface. The minimum scattering angle is defined for a scattering event that takes place in the x-y plane of the scattering rod with

$$\begin{aligned}
\overrightarrow{r_{f,\text{min}}} &= \left\langle -F, \frac{f}{2}, 0 \right\rangle, \\
\overrightarrow{r_{\theta,\text{min}}} &= \left\langle r\cos\lambda, r\sin\lambda, 0 \right\rangle, \\
\overrightarrow{r_{d,\text{min}}} &= \left\langle D\cos\theta + \frac{d}{2}\sin\theta, -D\sin\theta + \frac{d}{2}\cos\theta, 0 \right\rangle,
\end{aligned}$$

where λ must be determined for the system. The maximum scattering angle is defined for a scattering event that takes place on the top or bottom of the scattering rod with

$$\begin{aligned}
\overrightarrow{r_{f,\text{max}}} &= \left\langle -F, -\frac{f}{2}, -\frac{f}{2} \right\rangle, \\
\overrightarrow{r_{\theta,\text{max}}} &= \left\langle r\cos\alpha, r\sin\alpha, \frac{L}{2} \right\rangle, \\
\overrightarrow{r_{d,\text{max}}} &= \left\langle D\cos\theta - \frac{d}{2}\sin\theta, -D\sin\theta - \frac{d}{2}\cos\theta, -\frac{d}{2} \right\rangle,
\end{aligned}$$

where α must be determined for the system.

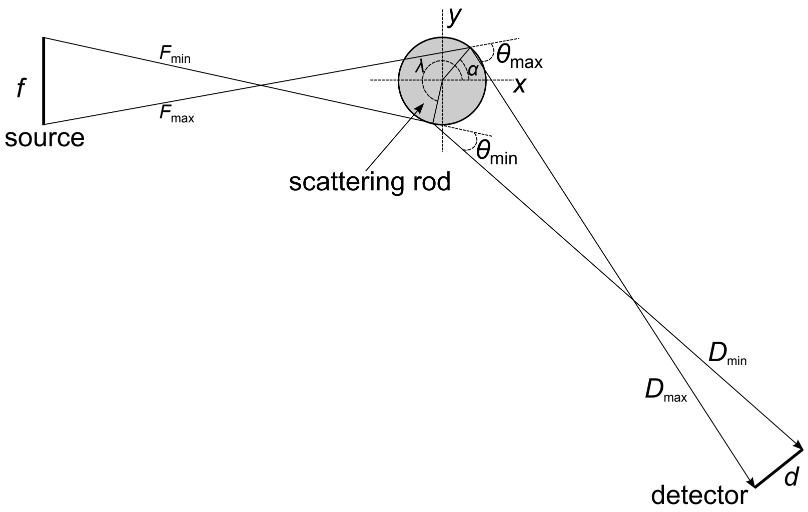

Figure A.1: Diagram that defines the variables that were used to calculate θ_{min} and θ_{max} for CS measurements. The diameters of the source, scattering rod, and collimating aperture are defined by f, $2r$, and d, respectively. The distance between the point of photon emission and the point of interaction is F, while the distance from interaction to the position of detection is D.

Using these definitions, θ_{min} and θ_{max} are found using

$$\theta_{\text{min}} = \arccos \frac{r\cos\lambda\left(D\cos\theta + \frac{d}{2}\sin\theta - F\right) + r\sin\lambda\left(-D\sin\theta + \frac{d}{2}\cos\theta + \frac{f}{2}\right) - r^2 + \frac{d}{2}\left(F\sin\theta - \frac{f}{2}\cos\theta\right) + D\left(F\cos\theta + \frac{f}{2}\sin\theta\right)}{\left[(r\cos\lambda + F)^2 + \left(r\sin\lambda - \frac{f}{2}\right)^2\right]^{\frac{1}{2}} \cdot \left[\left(D\cos\theta + \frac{d}{2}\sin\theta - r\cos\lambda\right)^2 + \left(-D\sin\theta + \frac{d}{2}\cos\theta - r\sin\lambda\right)^2\right]^{\frac{1}{2}}},$$

$$\theta_{\text{max}} = \arccos \frac{r\cos\alpha\left(D\cos\theta - \frac{d}{2}\sin\theta - F\right) + r\sin\alpha\left(-D\sin\theta - \frac{d}{2}\cos\theta - \frac{f}{2}\right) - r^2 + \frac{d}{2}\left(-F\sin\theta - \frac{f}{2}\cos\theta - \frac{L}{2} - \frac{f}{2}\right) + D\left(F\cos\theta - \frac{f}{2}\sin\theta\right) + \frac{L}{4}(-L - f)}{\left[(r\cos\alpha + F)^2 + \left(r\sin\alpha + \frac{f}{2}\right)^2 + \left(\frac{L}{2} + \frac{f}{2}\right)^2\right]^{\frac{1}{2}} \cdot \left[\left(D\cos\theta + -\frac{d}{2}\sin\theta - r\cos\alpha\right)^2 + \left(-D\sin\theta - \frac{d}{2}\cos\theta - r\sin\alpha\right)^2 + \left(-\frac{d}{2} - \frac{L}{2}\right)^2\right]^{\frac{1}{2}}},$$

through a series of calculations where λ and α are varied between 0° and 360°.

Bibliography

K. J. Adams. Electron upgrade for MCNP4B. *Los Alamos National Laboratory memorandum X-5-RN(U)-00-14*, 2000.

S. Agostinelli, S. Garelli, M. Piergentili, and F. Foppiano. Response to high-energy photons of PTW31014 PinPoint ion chamber with a central aluminum electrode. *Med. Phys.*, 35: 3293–3301, 2008.

A. Ahnesjo and M. M. Aspradakis. Dose calculations for external photon beams in radiotherapy. *Phys. Med. Biol.*, 44:R99–R155, 1999.

J. H. Aitken and W. H. Henry. Spectra of the internally scattered radiation from large ^{60}Co sources used in teletherapy. *International Journal of Applied Radiation and Isotopes*, 15: 713–724, 1964.

P. R. Almond, P. J. Biggs, B. M. Coursey, W. F. Hanson, M. S. Huq, R. Nath, and D. W. O. Rogers. AAPM's TG-51 protocol for clinical reference dosimetry of high-energy photon and electron beams. *Med. Phys.*, 26:1847–1870, 1999.

B. R. Archer and L. K. Wagner. Determination of diagnostic x-ray spectra with characteristic radiation using attenuation analysis. *Med. Phys.*, 15:637–641, 1988.

F. H. Attix. *Introduction to Radiological Physics and Radiation Dosimetry.* Wiley-VCH, Weinheim, Germany, 2004.

P. Bandžuch, M. Morháč, and J. Krištiak. Study of the Van Cittert and Gold iterative methods of deconvolution and their application in the deconvolution of experimental spectra of positron annihilation. *Nucl. Instrum. Methods Phys. Res. A*, 384:506–515, 1997.

L. J. Bartol and L. A. DeWerd. Technical note: improved implementation of doppler broadening in MCNP5. *Med. Phys.*, 39:5635–5638, 2012.

S. M. Beach. *Spectroscopic Characterization of Low Dose Rate Brachytherapy Sources.* Ph.D. dissertation, University of Wisconsin–Madison, 2005.

S. M. Beach and L. A. DeWerd. Deconvolution and reconstruction techniques of closely spaced low-energy spectra from high-purity germanium spectrometry. *Nucl. Instr. Meth. Phys. Res. A*, 572:794–803, 2007.

R. E. Bentley, J. C. Jones, and S. C. Lillicrap. X-ray spectra from accelerators in the range 2 to 6 MeV. *Phys. Med. Biol.*, 12:301–314, 1967.

M. J. Berger, J. S. Coursey, M. A. Zucker, and J. Chang. ESTAR, PSTAR, and ASTAR: Computer programs for calculating stopping-power and range tables for electrons, protons, and helium atoms (Version 1.2.3). [Online] Available: http://physics.nist.gov/star (last accessed 16 Nov 2010), National Institute of Standards and Technology, Gaithersburg, MD, 2005a.

M. J. Berger, J. H. Hubbell, S. M. Seltzer, J. Chang, J. S. Coursey, R. Sukumar, and D. S. Zucker. XCOM: Photon cross section database (Version 1.3). [Online] Available: http://physics.nist.gov/xcom (last accessed 16 Nov 2010), National Institute of Standards and Technology, Gaithersburg, MD, 2005b.

F. Biggs, L. B. Mendelsohn, and J. B. Mann. Hartree-Fock Compton profiles for the elements. *Atomic data and nuclear data tables*, 16:201–309, 1975.

T. E. Booth, F. B. Brown, J. S. Bull, R. A. Forster, T. S. Goorley, H. G. Hughes, R. L. Martz, R. E. Prael, A. Sood, J. E. Sweezy, and A. J. Zukaitis. MCNP5-1.50 release notes. Technical report, Los Alamos National Laboratory, 2008.

J. Borg and D.W.O. Rogers. PIRS-629r: Monte Carlo calculations of photon spectra in air from Ir-192 sources. Technical report, National Research Council, March 1999.

F. Brown, B. Kiedrowski, and J. Bull. MCNP5-1.60 release notes. Technical report, Los Alamos National Laboratory, 2010.

J. Brownridge, S. Samnick, P. Stiles, P. Tipton, J. Veselka, and N. Yeh. Determination of the photon spectrum of a clinical accelerator. *Med. Phys.*, 11:794–796, 1984.

L. L. Campos and L. V. E. Caldas. Induced effects in ionization chamber cables by photon and electron irradiation. *Med. Phys.*, 18:522–526, 1991.

CANBERRA Industries. Canberra product catalog.

G. A. Carlsson, K. F. Berggren, C. A. Carlsson, G. Matscheko, and R. Ribberfors. The Compton spectrometer. *International Journal of Quantum Chemistry*, 35:721–734, 1989.

E. L. Chaney, T. J. Cullip, and T. A. Gabriel. A Monte Carlo study of accelerator head scatter. *Med. Phys*, 21:1383–1390, 1994.

O. Chibani, B. Moftah, and C.-M. Ma. On Monte Carlo modeling of megavoltage photon beams: A revisited study on the sensitivity of beam parameters. *Med. Phys.*, 38:188–201, 2011.

S. Y. F. Chu, L. P. Ekström, and R. B. Firestone. The Lund/LBNL Nuclear Data Search, Version 2.0, February 1999. [Online] Available: http://nucleardata.nuclear.lu.se/nucleardata/toi/ (last accessed 16 Nov 2010), 1999.

A. H. Compton. A quantum theory of the scattering of x-rays by light elements. *Phys. Rev.*, 21:483–502, 1923.

M. J. Cooper. Compton scattering and electron momentum determination. *Rep. Prog. Phys.*, 48:415–481, 1985.

L. Costrell. Scattered radiation from large Co-60 calibrating sources. *Health Phys.*, 8: 261–272, 1962.

S. D. Davis. *Air-kerma strength determination of a miniature x-ray source for brachytherapy applications.* Ph.D. dissertation, University of Wisconsin–Madison, 2009.

J. J. DeMarco, T. D. Solberg, and J. B. Smathers. A CT-based Monte Carlo simulation tool for dosimetry planning and analysis. *Med. Phys*, 25:1–11, 1998.

J. Deng, T. Guerrero, C. M. Ma, and R. Nath. Modelling 6 MV photon beams of a stereotactic radiosurgery system for Monte Carlo treatment planning. *Phys. Med. Biol.*, 49:1689–1704, 2004.

S. Dhanesar. *Conformal radiation therapy with cobalt-60 tomotherapy.* Ph.D. dissertation, Queen's University, 2008.

J. W. M. Du Mond. Compton modified line structure and its relation to the electron theory of solid bodies. *Physical Review*, 33:643–658, 1929.

M. Ehrlich, S. M. Seltzer, M. J. Bielefeld, and J. I. Trombka. Spectrometry of a ^{60}Co gamma-ray beam used for instrument calibration. *Metrologia*, 12:169–179, 1976.

B. A. Faddegon. Pile-up corrections in pulsed-beam spectroscopy. *Nucl. Instrum. Method B*, 51:431–441, 1990.

B. A. Faddegon, M. Asai, J. Perl, C. K. Ross, J. Sempau, J. Tinslay, and F. Salvat. Benchmarking of Monte Carlo simulation of bremsstrahlung from thick targets at radiotherapy energies. *Med. Phys.*, 10:4308–4317, 2008.

B. A. Faddegon, C. K. Ross, and D. W. O. Rogers. Forward-directed bremsstrahlung of 10- to 30-MeV electrons incident of thick targets of Al and Pb. *Med. Phys.*, 17:773–785, 1990.

G. Fehrenbacher, R. Meckbach, and P. Jacob. Unfolding the response of a Ge detector used for in-situ gamma-ray spectrometry. *Nucl. Instrum. Methods Phys. Res. A*, 383:454–462, 1996.

C. Fox, H. E. Romeijn, B. Lynch, C. Men, D. M. Aleman, and J. F. Dempsey. Comparative analysis of ^{60}Co intensity-modulated radiation therapy. *Phys. Med. Biol.*, 53:3175–3188, 2008.

R. P. Gardner, A. M. Yacout, J. Zhang, and K. Verghese. An investigation of the possible interaction mechanisms for Si(Li) and Ge detector response functions by Monte Carlo simulation. *Nucl. Instrum. Methods Phys. Res. A*, 242:399–405, 1986.

G. R. Gilmore. *Practical Gamma-ray Spectrometry.* John Wiley & Sons, Inc., West Sussex, England, 2nd edition, 2008.

K. Han, D. Ballon, C. Chui, and R. Mohan. Monte Carlo simulation of a cobalt-60 beam. *Med. Phys.*, 14(3):414–419, 1987.

J. Hrbacek, S. Lang, and S. Klock. Commissioning of photon beams of a flattening filter-free line accelerator and the accuracy of beam modeling using an anisotropic analytical algorithm. *Int. J. Radiat. Oncol. Biol. Phys.*, 80:1128–1237, 2011.

ICRU. Dosimetry of high-energy photon beams based on standards of absorbed dose to water. Report 64, International Commission on Radiation Units and Measurements, 2001.

G. E. M. Jauncey. Quantum theory of the intensity of the modified band in the Compton effect. *Phys. Rev.*, 25:723–736, 1925.

R. Jeraj, P. J. Keall, and P. M. Ostwald. Comparisons between MCNP, EGS4 and experiment for clinical electron beams. *Phys. Med. Biol.*, 44:705–717, 1999.

R. Jeraj, T. R. Mackie, J. Balog, and G. Olivera. Radiation characteristics of helical tomotherapy. *Med. Phys*, 31:396–404, 2004.

K. A. Jessen. Measurements of primary spectra from a kilocurie ^{60}Co unit and a 6 MeV linear accelerator. *Acta Radiologica Therapy Physics Biology*, 12:561–568, 1973.

Y. Jin, R. P. Gardner, and K. Verghese. A semi-empirical model for the gamma-ray response function of germanium detectors based on fundamental interaction mechanisms. *Nucl. Instrum. Methods Phys. Res. A*, 242:416–426, 1986.

H. E. Johns. The physicist in cancer treatment and detection. *Int. J. Radiat. Oncol. Biol. Phys.*, 7:801–808, 1980.

C. J. Karzmark, C. S. Nunan, and E. Tanabe. *Medical electron accelerators*. McGraw-Hill, Inc., 1993.

C. J. Karzmark and N. C. Pering. Electron linear accelerators for radiation therapy: history, principles and contemporary developments. *Phys. Med. Biol.*, 18:321–354, 1973.

F. Khan. *The Physics of Radiation Therapy*. Lippincott Williams and Wilkins, Philadelphia, PA, USA, 3rd edition, 2003.

O. Klein and Y. Nishina. Uber die streuung von strahlung durch freie elektronen nach der neuen relativistischen quantendyamik von dirac. *Z. F. Phys.*, 52:853–869, 1929.

G. F. Knoll. *Radiation Detection and Measurement.* John Wiley & Sons, Inc., New York, 3rd edition, 2000.

M. Krmar, D. Nikolić, P. Krstonošić, S. Cora, P. Francescon, P. Chiovati, and A. Rudić. A simple method for bremsstrahlung spectra reconstruction from transmission measurements. *Med. Phys.*, 29:932–938, 2002.

M. Krmar, J. Slivka, I. Bikit, M. Vesković, and Lj. Čonkić. Evaluation of bremsstrahlung spectra generated by a 4 MeV linear accelerator. *Med. Phys.*, 23:651–654, 1996.

S. F. Kry, U. Titt, F. Pönisch, D. Followill, O. N. Vassiliev, R. A. White, R. Mohan, and M. Salehpour. A Monte Carlo model for calculating out-of-field dose from a Varian 6 MV beam. *Med. Phys*, 33:4405–4413, 2006.

R. P. Lambert, J. W. Jury, and N. K. Sherman. Measurement of bremsstrahlung spectra from 25 MeV electrons on Ta as a function of radiator thickness and emission angle. *Nucl. Instrum. Methods*, 214:349–360, 1983.

D. J. Landry and D. W. Anderson. Measurement of accelerator bremsstrahlung spectra with a high-efficiency Ge detector. *Med. Phys.*, 18(3):527–532, 1991.

J. S. Laughlin. Development of the technology of radiation therapy. *RadioGraphics*, 9: 1245–1266, 1989.

J. S. Laughlin, R. Mohan, and G. J. Kutcher. Choice of optimum megavoltage for accelerators for photon beam treatment. *Int. J. Radiat. Oncol. Biol. Phys.*, 12:1551–1557, 1986.

L. B. Levy, R. G. Waggener, W. D. McDavid, and W. H. Payne. Experimental and calculated bremsstrahlung spectra from a 25 MeV linear accelerator and 19 MeV betatron. *Med. Phys.*, 1:62–67, 1974.

L. B. Levy, R. G. Waggener, and A. E. Wright. Measurement of primary bremsstrahlung spectrum from an 8 MeV linear accelerator. *Med. Phys.*, 3:173–175, 1976.

R. D. Lewis, S. J. S. Ryde, D. A. Hancock, and C. J. Evans. An MCNP-based model of a linear accelerator. *Phys. Med. Biol.*, 44:1219–1230, 1999.

B. Libby, J. Siebers, and R. Mohan. Validation of Monte Carlo generated phase-space descriptions of medical linear accelerators. *Med. Phys.*, 26(8):1476–1483, 1999.

M. L. F. Lim. *Principles and practice of clinical physics and dosimetry.* Advanced Medical Publishing, Inc., 2006.

F. Longo, L. Pandola, and M. G. Pia. New Geant4 developments for Doppler broadening simulation in Compton scattering; development of charge transfer simulation models in Geant4. *2008 IEEE Nuclear Science Symposium Conference Record*, pages 2865–2868, 2008.

D. M. Lovelock, C. S. Chui, and R. Mohan. A Monte Carlo model of photon beams used in radiation therapy. *Med. Phys.*, 22:1387–1394, 1995.

T. R. Mackie, P. Reckwerdt, T. McNutt, M. Gehring, and C. Sanders. Photon beam dose computations. In *Teletherapy: Present and Future: Proceedings of the 1996 Summer School*, pages 103–136. American Association of Physicists in Medicine, Advanced Medical Publishing, 1996.

T. R. Mackie, J. W. Scrimger, and J. J. Battista. A convolution method for calculating dose from 15 MV x-rays. *Med. Phys.*, 12:188–196, 1985.

C. Martens, C. De Wagter, and W. De Neve. The value of the PinPoint chamber for characterization of small field segments used in intensity-modulated radiotherapy. *Phys. Med. Biol.*, 45:2519–2530, 2000.

G. Matscheko and G. A. Carlsson. Measurements of absolute energy spectra from a clinical CT machine under working conditions using a Compton spectrometer. *Phys. Med. Biol*, 34:209–222, 1989.

T. J. McCaw, J. A. Micka, and L. A. DeWerd. Characterizing the marker-dye correction for Gafchromic EBT2 film: a comparison of three analysis methods. *Med. Phys.*, 38: 5771–5777, 2011.

R. Minniti, H. Chen-Mayer, S. M. Seltzer, M. S. Huq, L. Bryson, T. Slowey, J. A. Micka, L. A. DeWerd, N. Wells, W. F. Hanson, and G. S. Ibbott. The US radiation dosimetry standards for ^{60}Co therapy level beams, and the transfer to the AAPM accredited dosimetry calibration laboratories. *Med. Phys.*, 33:1074–1077, 2006.

J. Moga. *Characterization of low-energy photon-emitting brachytherapy sources and kilovoltage x-ray beams using spectrometry.* Ph.D. dissertation, University of Wisconsin–Madison, 2011.

J. Moga and L. DeWerd. Characterization of kilovoltage x-ray spectra using measurements with a high-purity germanium detector and Monte Carlo simulations. *Med. Phys.*, 37: 3427, 2010.

R. Mohan, C. Chui, and L. Lidofsky. Energy and angular distributions for photons from medical linear accelerators. *Med. Phys.*, 12:592–597, 1985.

G. M. Mora, A. Maio, and D. W. O. Rogers. Monte Carlo simulation of a typical ^{60}Co therapy source. *Med. Phys.*, 26(11):2494–2502, 1999.

M. Morháč, J. Kliman, V. Matoušek, M. Veselský, and I. Turzo. Efficient one- and two-dimensional Gold deconvolution and its application to gamma-ray spectra decomposition. *Nucl. Instrum. Methods Phys. Res. A*, 401:385–408, 1997.

M. Morháč, V. Matoušek, and J. Kliman. Efficient algorithm of multidimensional deconvolution and its application to nuclear data processing. *Digital Signal Processing*, 13: 144–171, 2003.

T. Nakamura and H. Hirayama. Spectra of bremsstrahlung produced in very thick lead targets by 15-, 20-, and 25-MeV electrons. *Nuclear Science and Engineering*, 59:237–245, 1976.

Y. Namito, S. Ban, and H. Hirayama. Implementation of the Doppler broadening of a Compton-scattered photon into the EGS4 code. *Nucl. Instrum. Methods Phys. Res. A*, 349:489–494, 1994.

NCRP Report 151. Structural shielding design and evaluation for megavoltage x- and gamma-ray radiotherapy facilities. Technical Report 151, National Council on Radiation Protection and Measurements, Bethesda, MD, 2005.

A. A. O'Dell, C. W. Sandifer, R. B. Knowlen, and W. D. George. Measurements of absolute thick-target bremsstrahlung spectra. *Nucl. Instrum. Methods*, 61:340–346, 1968.

N. Papanikolaou and S. Stathakis. Dose-calculation algorithms in the context of inhomogeneity corrections for high energy photon beams. *Med. Phys*, 36:4765–4775, 2009.

E. B. Podgorsak. *Radiation Oncology Physics: A Handbook for Teachers and Students.* International Atomic Energy Agency, Vienna, Austria, 2005.

R. Ribberfors and K. F. Berggren. Incoherent-x-ray scattering functions and cross sections $(d\sigma/d\omega')_{incoh}$ by means of a pocket calculator. *Phys. Rev. A*, 26:3325–3333, 1982.

D. W. O. Rogers. *Clinical Dosimetry Measurements in Radiotherapy.* Medical Physics Publishing, 2009.

D. W. O. Rogers, B. A. Faddegon, G. X. Ding, C. Ma, J. We, and T. R. Mackie. BEAM: A Monte Carlo code to simulate radiotherapy treatments. *Med. Phys.*, 22:503–524, 1995.

C. W. Scarantino, C. J. Rini, M. Aquino, T. B. Carrea, R. D. Ornitz, M. S. Anscher, and R. D. Black. Initial clinical results of an *in vivo* dosimeter during external beam radiation therapy. *Int. J. Radiat. Oncol. Biol. Phys.*, 62(2):606–613, 2005.

L. J. Schreiner, A. Kerr, G. Salomons, C. Dyck, and G. Hajdok. The potential for image guided radiation therapy with cobalt-60 tomotherapy. In *Medical Image Computing and Computer-Assisted Intervention*, 2003.

J. W. Scrimger and D. V. Cormack. Spectrum of the radiation from a cobalt 60 teletherapy unit. *Br. J. Radiol.*, 36:514–521, 1963.

W. W. Seelentag and W. Panzer. Stripping of x-ray bremsstrahlung spectra up to 300 kVp on a desk type computer. *Phys. Med. Biol.*, 24(4):767–780, 1979.

D. Sheikh-Bagheri and D. W. O. Rogers. Monte Carlo calculation of nine megavoltage photon beam spectra using the BEAM code. *Med. Phys.*, 29(3):391–402, 2002.

N. K. Sherman, K. H. Lokan, R. M. Hutcheon, L. W. Funk, W. R. Brown, and P. Brown. Bremsstrahlung radiators and beam filters for 25 MeV cancer therapy. *Med. Phys.*, 1: 185–192, 1974.

J. V. Siebers, P. J. Keall, B. Libby, and R. Mohan. Comparison of EGS4 and MCNP4b Monte Carlo codes for generation of photon phase space distributions for a Varian 2100C. *Phys. Med. Biol.*, 44:3009–3026, 1999.

L. D. Skarsgard, H. E. Johns, and L. E. S. Green. Iterative response correction for a scintillation spectrometer. *Radiat. Res.*, 14:261–280, 1961.

J. B. Smilowitz. *Integration of dose measurements and model-based treatment planning algorithms*. Ph.D. dissertation, University of Wisconsin–Madison, 2002.

J. B. Smilowitz, R. Jeraj, G. H. Olivera, L. A. DeWerd, and T. R. Mackie. Monte Carlo model of an Accredited Dosimetry Calibration Laboratory Cobalt-60 unit. In *Proceedings of Recent developments in accurate radiation dosimetry: International Workshop*, page in press. Medical Physics Publishing, 2001.

C. Soares. Personal communication, November 2010.

A. Sood. Doppler energy broadening for incoherent scattering in MCNP5, part I. Memorandum LA-UR-04-0487, Los Alamos National Laboratory, Los Alamos, NM, 2004.

A. Sood and R. P. Gardner. A new Monte Carlo assisted approach to detector response functions. *Nucl. Instrum. Methods Phys. Res. B*, 312:100–104, 2004.

A. Sood and M. C. White. Doppler energy broadening for incoherent scattering in MCNP5, part II. Memorandum LA-UR-04-0488, Los Alamos National Laboratory, Los Alamos, NM, 2004.

G. Starkschall, R. E. Steadham Jr., R. A. Popple, S. Ahmad, and I. I. Rosen. Beam-commissioning methodology for a three-dimensional convolution/superposition photon dose algorithm. *Journal of Applied Clinical Medical Physics*, 1:8–27, 2000.

Å. C. Tedgren, S. de Luelmo, and J. E. Grindborg. Characterization of a ^{60}Co unit at a secondary standard dosimetry laboratory: Monte Carlo simulations compared to measurements and results from the literature. *Med. Phys*, 37:2777–2786, 2010.

P.-H. van der Giessen. Maintenance costs for cobalt machines and linear accelerators: new machines versus old. *Radiother. Oncol.*, 62:349–352, 2002.

J. Van Dyk and J. J. Battista. Co-60: An old modality, a renewed challenge. *Current Oncology*, 3:8–17, 1996.

F. Verhaegen and J. Seuntjens. Monte Carlo modelling of external radiotherapy photon beams. *Phys. Med. Biol.*, 48:R107–R164, 2003.

M. C. White. Photoatomic data library MCPLIB04: A new photoatomic library based on data from ENDF/B-VI Release 8. Memorandum LA-UR-03-1019, Los Alamos National Laboratory, Los Alamos, NM, 2003.

M. C. White. Further notes on mcplib03/04 and new mcplib63/84 Compton broadening data for all versions of MCNP5. Technical report, Los Alamos National Laboratory, 2012.

X-5 Monte Carlo Team. *MCNP — A General Monte Carlo N-Particle Transport Code, Version 5, Report LA-UR-03-1987.* Los Alamos National Laboratory, Los Alamos, NM, 2005.

A. M. Yacout, R. P. Gardner, and K. Verghese. A semi-empirical model for the x-ray Si(Li) detector response function. *Nucl. Instrum. Methods Phys. Res. A*, 243:121–130, 1986.

S.-J. Ye, R. Ove, and S. A. Naqvi. Doppler broadening effect on low-energy photon dose calculations using MCNP5 and PENELOPE. *Health Phys.*, 91:361–366, 2006.

C. Yu, C. Amies, and M. Svatos. Planning and delivery of intensity-modulated radiation therapy. *Med. Phys*, 35:5233–5241, 2008.